POROSITY CLASSIFICATION AND RESERVOIR FLOW UNITS RANKING IN THE KHARTAM MEMBER, KHUFF FORMATION (PERMO-TRIASSIC): OUTCROP APPROACH, CENTRAL SAUDI ARABIA

BY

Asaad Mohammed Mohammed Ahmed Abdulraziq

A Thesis Presented to the
DEANSHIP OF GRADUATE STUDIES

KING FAHD UNIVERSITY OF PETROLEUM & MINERALS

DHAHRAN, SAUDI ARABIA

In Partial Fulfillment of the
Requirements for the Degree of

MASTER OF SCIENCE

In

GEOLOGY

APRIL 2014

KING FAHD UNIVERSITY OF PETROLEUM & MINERALS
DHAHRAN- 31261, SAUDI ARABIA
DEANSHIP OF GRADUATE STUDIES

This thesis, written by **ASAAD MOHAMMED ABDULRAZIQ** under the direction his thesis advisor and approved by his thesis committee, has been presented and accepted by the Dean of Graduate Studies, in partial fulfillment of the requirements for the degree of **MASTER OF SCIENCE IN GEOLOGY.**

Dr. Osman Abdullatif
(Advisor)

Dr. Abdulaziz Al-Shaibani
Department Chairman

Dr. Gabor Korvin
(Member)

Dr. Salam A. Zummo
Dean of Graduate Studies

Dr. Lamidi Babalola
(Member)

15/5/14
Date

ACKNOWLEDGMENTS

I would to thank the Earth Sciences Department and King Fahd University of Petroleum & Minerals for offering me this opportunity to complete my graduate studies. I also would like to thank the Center for Water & Environment/Research Institute at King Fahd University of Petroleum & Minerals for having me as a research assistant and financially support my scholarship.

My immense thankfulness to my supervisor, Dr. Osman Abdullatif for his support, and invaluable guidance throughout my journey at King Fahd University of Petroleum & Minerals. Special thanks also go out to my committee members, Prof. Gabor Korvin and Dr. Lamidi Babalola, for their insights and constructive comments. Also I want to express my gratitude to Dr. Hassan Eltom for being a great guider through all the stages of my research.

I would like to thank the King Abdulaziz City for Science and Technology (KACST) for providing support to this research through NSTIP project No. 10-Oil1379-04 as a part of National Science, Technology and Innovation Plan (NSTIP).

My deepest appreciation goes to my mother and father for their support, patience, and prayers. I would like to extend my thanks to the rest of my family members who have provided moral strength and encouraged me to complete this study.

TABLE OF CONTENTS

LIST OF TABLES

LIST OF FIGURES

LIST OF ABBREVIATIONS

PIA	:	Petrographic Image Analysis
SEM	:	Scanning Electron Microscopy
HFSs	:	High Frequency Sequences
HST	:	Highstand System Tract
LST	:	Lowstand System Tract
TST	:	Transgressive System Tract

ABSTRACT (ENGLISH)

Full Name : Asaad Mohammed Mohammed Ahmed Abdulraziq

Thesis Title : Porosity Classification and Reservoir Flow Units Ranking in The Khartam Member, Khuff Formation (Permo-Triassic): Outcrop Approach, Central Saudi Arabia

Major Field : Geology

Date of Degree : April 2014

The study investigates the porosity and flow units' characteristics of the Permo-Triassic Upper Khartam Member of the Khuff Formation. Outcrop exposure in At Tarafiyah area, Qasim region, central Saudi Arabia. The objectives of this study are: to identify the geometrical characteristics for each pore type and subdivide the individual pore type based on their geometries, establish the porosity-permeability relationship and to determine the heterogeneity in the porosity and permeability and integrate the porosity-permeability data to identify and rank the flow units at the outcrop scale. Thin section petrography was used to identify the different types of porosity and the diagenetic alterations that may affect the porosity. The pore sizes, pore geometrical shapes, and frequency distribution frequencies were determined using Petrographic Image Analysis technique. Microporosity in the investigated samples was identified with the aid of Scanning electron microscopy microscope (SEM). Core plugs' poroiometer and permeameter were used to measure the total porosity and the permeability. The outcrop succession is mainly composited of well-sorted oolitic grainstone, cross-bedded oolitic skeletal grainstone and graded mudstone to packstone facies. This study revealed two distinguished geometries of the moldic porosity (oomoldic and skelmoldic) and two different geometrical-sizes of the vuggy porosity (vuggy-1 and vuggy-2). Petrographic image analysis was used to identify the pore sizes, aspect ratio and roundness factor for each pore type. Oomoldic and vuggy-1 porosities are ranked to be the best porosity types, in term of size and their contribution in the overall porosity. The combination of oomoldic and vuggy-1 form the optimum reservoir quality. Coefficients of variance indicated major heterogeneity in the porosity and permeability, which can be attributed to the variation within the individual pore type, presence of micropores system and the mixture of the pore types within the individual facies. Generally, poor correlation coefficient was obtained between porosity and permeability when the lithofacies are combined. This correlation improved significantly when porosity and permeability were plotted based on the individual facies group. This heterogeneity in the porosity and permeability most was probably controlled by depositional facies and by the diagenetic alterations (leaching/cementation). Gathering the porosity-permeability data of the studied outcrop revealed that cross-bedded oolitic skeletal grainstone facies has the highest flow units' quality where moldic and vuggy porosities are dominant. In the vertical sections', the flow units boundaries perfectly coincide with the facies boundaries. However, few intervals do not follow the facies boundaries. This most probably indicate that the flow units are primarily controlled by the facies, and s diagenetic alterations.

ABSTRACT (ARABIC)

ملخص الرسالة

الاسم الكامل: أسعد محمد محمد أحمد عبدالرازق

عنوان الرسالة: تصنيف المسامية وترتيب جودة الوحدات السامحة بالتدفق في عضو الخرطم، تكوين الخف (البرمي – الترياسي): دراسة على المنكشف السطحي ، في وسط المملكة العربية السعودية

التخصص: الجيولوجيا

تاريخ الدرجة العلمية: أبريل 2014

هذه الدراسة تتحرى الخصائص المميزة للمسامية وللوحدات التي تسمح بالتدفق في المنكشف السطحي لعضو الخركم العلوي من تكوين الخف (البرمي - الترياسي). تقع منطقة الدراسة في منطقة الطرفية في إقليم القصيم، وسط المملكة العربية السعودية. أهداف هذه الدراسة تتلخص في: التعرف على الخصائص الهندسية لكل نوع من أنواع المسامية وذلك للتمكن من إحداث التقسيم المناسب على كل نوع عند ملاحظة أي فروق هندسية. إقامة علاقة بين المسامية والنفاذية وأيضا تحديد عدم التجانس في كل من المسامية والنفاذية. تم دمج بيانات المسامية والنفاذية وذلك لتحديد وترتيب الوحدات التي تسمح بالتدفق على مستوى المنكشف السطحي. تم إستخدام تحليل الصور البتروجرافية وذلك للحصول على أحجام المسام ، والأشكال الهندسية ، وتوزيع التكرارات. تم دراسة الشريحة الصخرية الرقيقة تحت المجهر وذلك لتحديد أنواع المسامية المختلفة وأثر عمليات النشأة المتأخرة على المسامية. تم إعتماد المجهر الإلكتروني (SEM) في تحديد المسامية الدقيقة. إستخدم جهاز قياس المسامية وجهاز قياس النفاذية على العينات الصخرية المقطوعة إسطوانيا للحصول على المسامية الكلية والنفاذية. يتكون التتابع الصخري في المنكشف السطحي أساسا من سحنات صخر حبيبات الأوليت جيد الفرز، وصخر حبيبات الأوليت وقطع المستحاثات ذو التطبق المتقاطع، الصخر المتدرج من حجر الطين إلى الباكستون. كشفت هذه الدراسة شكلين هندسيين مميزين من مسامية القالب (هما قالب الأوليت وقالب القطع المستحاثية) وشكلين/حجمين مختلفين من مسامية التقب (هما الثقب-1 والثقب-2). تم إستخدام تحليل الصور البتروجرافية لتحديد حجم المسام ، ونسبة الأبعاد ، وعامل الإستدارة لكل نوع من أنواع المسامات. تم تحديد كل من مسامية قالب الأوليت والثقب-1 ليكونا أفضل أنواع المسامية من حيث حجمهما ومساهمتهما في المسامية الكلية. الخليط من مسامية قالب الأوليت والثقب-1 يعطي أمثل جودة للخزانات

النفطية. أشارت معاملات التباين إلى عدم تجانس كبير في كل من المسامية والنفاذية ، والتي يمكن أن تعزى إلى الإختلافات في أحجام وأشكال المسام في نوع المسام الواحد ، ووجود نظام المسامية الدقيقة ، والخليط من أنواع المسامات المختلفة في السحنة الواحدة. بشكل عام ، كان معامل الارتباط بين المسامية والنفاذية ضعيف ، ولكن تحسن هذا المعامل بشكل ملحوظ عندما تم عمل العلاقة بين المسامية والنفاذية على أساس السحنات. عدم التجانس في كل من المسامية والنفاذية على الارجح محكوم بالسحنات الرسوبية وبعمليات النشأة المتأخرة (السمنتة/الإذابة). جمع بيانات المسامية مع النفاذية للمنكشف السطحي الذي تمت دراسته كشف أن سحنة صخر حبيبات الأوليت وقطع المستحاثات ذو التطبق المتقاطع لها أعلى جودة للتدفق لإحتوائها على مسامية ونفاذية عاليتين كونها تحتوي على نسب عالية من مسامية القالب والثقب. علاوة على ذلك ، من دراسة المقاطع الرأسية فإن حدود وحدات التدفق تتطابق بشكل كبير حدود السحنات. وبالرغم من ذلك ، فإن هنالك وحدات قليلة لا تتطابق مع حدود السحنات. هذا على الأرحج يدل يشير إلى أن وحدات التدفق معرفة في المقام الأول بالسحنات الرسوبية ، وتتأثر ثانيا بعمليات النشأة المتأخرة.

CHAPTER ONE

INTRODUCTION

Carbonate rocks which constitute important hydrocarbon reservoirs, are very heterogeneous and complex in terms of their reservoir quality. The complexity in carbonate rocks is due to their modes of formation (biological, chemical, and detrital processes), complex stratigraphy, susceptibility to extensive diagenetic changes, and complex mineralogical component. The complexity from the porosity point of view is because carbonate rocks contain a mixture of different types of porosity such as interparticle, intercrystalline, intraskeletal, vugular, and moldic porosities which makes the prediction of reservoir characteristics very hard.

This study focuses on porosity geometry (shape and roundness) and porosity size based on thin section petrography. Photomicrographs taken from the petrographic thin sections were analyzed to obtain the geometrical shapes for each type of porosity. The porosity in the thin section was classified according to the size and the geometrical shape. The significance of this classification is to indicate the pore geometry and pore type and relate them to each other. Geometrical subdivisions were also attempted when there are geometrical shapes' differences in individual porosity type.

By moving from thin section (mm) to higher scale, porosity and permeability measurements were conducted in the core plugs. In order to predict the permeability in given porosity, porosity-permeability relationship was established for this purpose. In order to make this prediction more efficient and to enhance the correlation, porosity-permeability relationship was constructed for each depositional texture separately.

Outcrop approach was introduced in this study to overcome the low resolution of the well data and to detect the heterogeneity within the reservoir units in term of facies, porosity and permeability in inter-well space scale (Girard et al., 2008). Outcrop can provide a high resolution in terms of flow units dimension (length and thickness), and identifying the lateral and vertical facies changes within the flow units. In addition, outcrop is used to justify the lateral and vertical variations in porosity and permeability, by identifying the factors that control reservoir quality (e.g. facies and/or diagenesis).

1.1. Study area

This study was carried out on the Permian-Triassic Khuff Formation outcrop located in At Tarafiyah area in the northern part of Buraydah town in Al-Qasim region in the central part of Saudi Arabia. Khuff Formation consists of N-S elongated outcrops that extend to approximately 1,200 km in the central Saudi Arabia (Steineke and Bramkamp, 1952; Steineke et al., 1958; Powers, 1968). The outcrop belt was divided into different quadrangles which include Buraydah quadrangle; where the study area is located (e.g., Vaslet et al., 2005) (Figure 1.1d).

Khuff Formation in the outcrop has been subdivided into five members which include from oldest to youngest, the Unayzah (Ash Shiqqah), Huqayl, Duhaysan, Midhnab and Khartam members (Delfour et al., 1982) (Figures 1.2 and 1.3). This study is focusing on the Khartam Member which is the uppermost member of Khuff Formation (Vaslet et al., 2005).

In At Tarafiyah area, Khartam outcrop is well exposed with 1.5 km width and 25 km length (Figures 1.1b and 1.1c). The outcrop mainly consists of interbedded carbonate grainstones and mudstones with some wackestones and packstones beds.

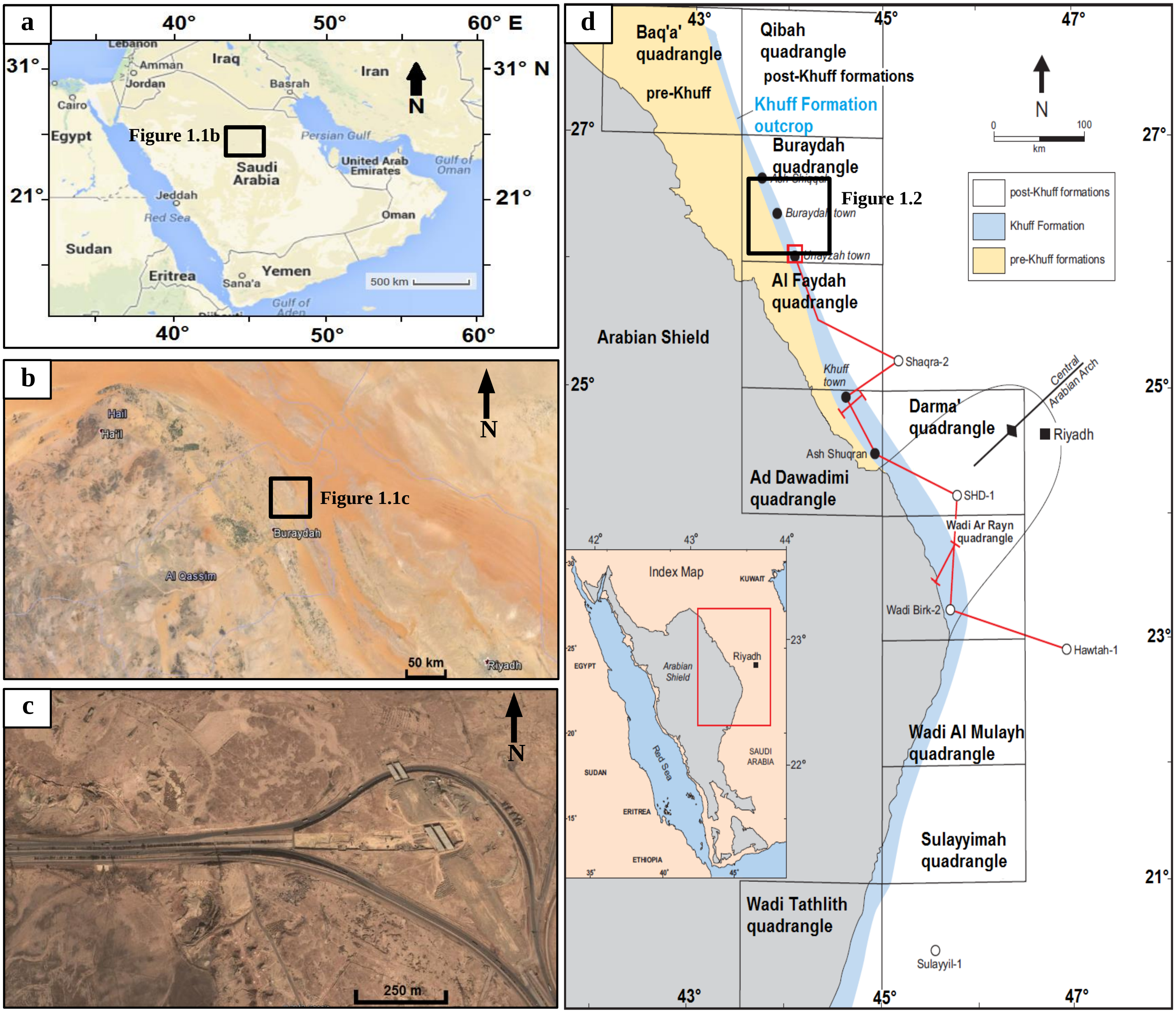

Figure 1.1: (a) Map showing the location of the study area highlighted with black box in the central Saudi Arabia; (b) close look of the region of the study area; (c) map showing the road cut of the studied outcrop (Google Maps, 2013); and (d) geological map showing the outcrops of Khuff Formation in different quadrangles, central Saudi Arabia (Vaslet et al., 2005).

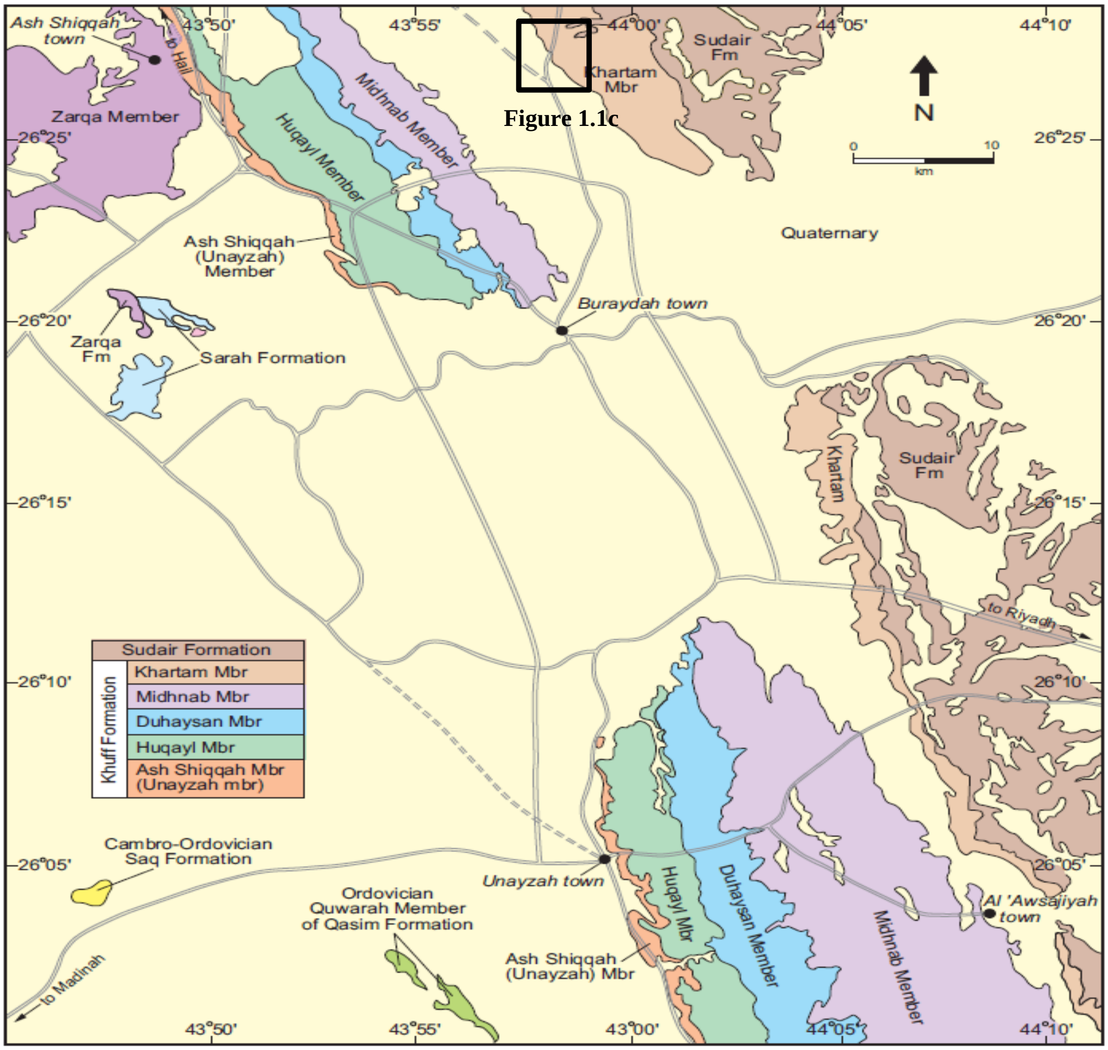

Figure 1.2: Geological map showing the members of the Khuff Formation at the outcrop as defined by Delfour et al. (1982) in the Buraydah quadrangle (See Figure 1.1d for the location of this map) (Vaslet et al., 2005).

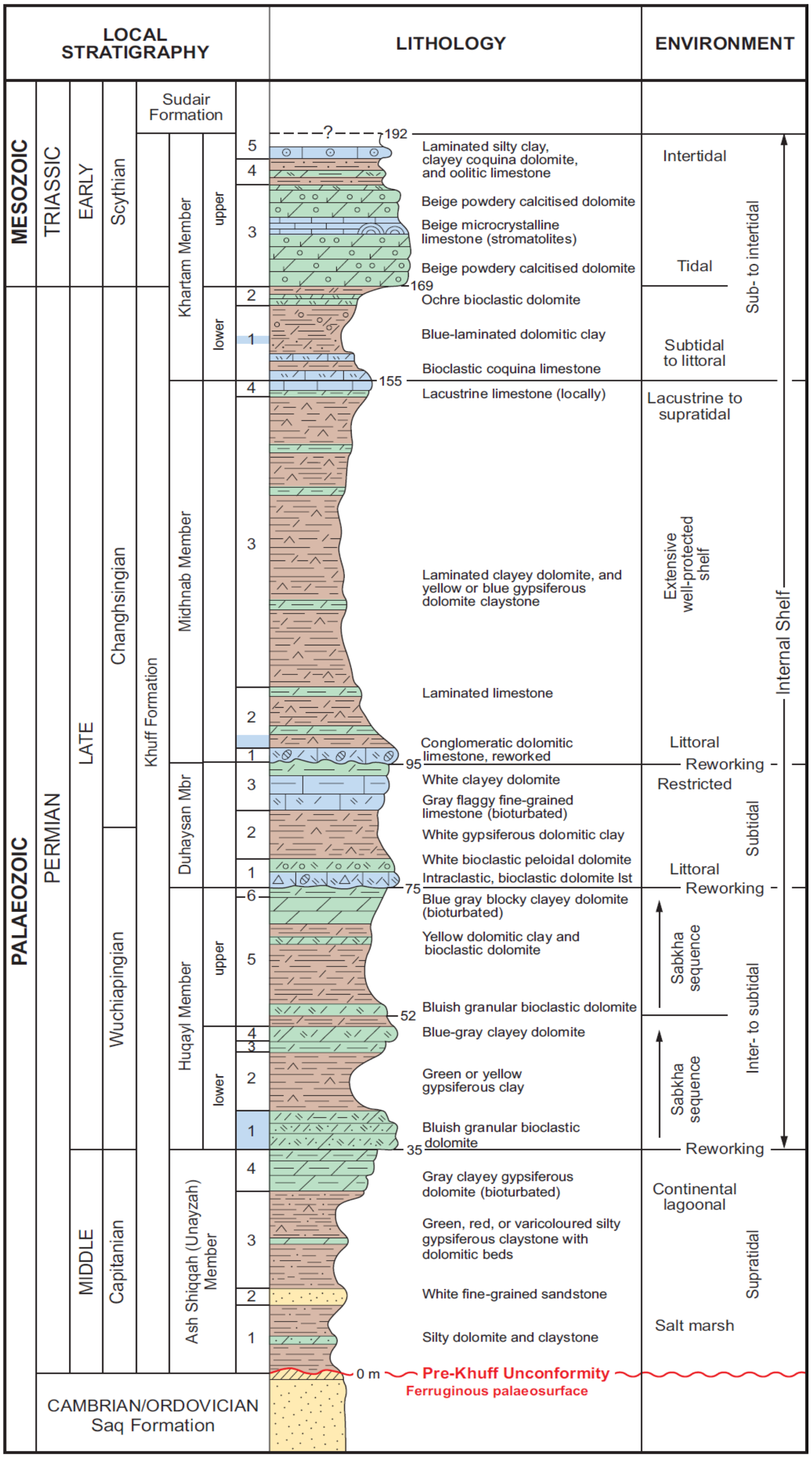

Figure 1.3: Outcrop lithostratigraphic section of Khuff Formation in reference section, central Saudi Arabia (Vaslet et al., 2005).

1.2. Objective

This study aims to characterize the porosity, examine the relationships between petrophysical parameters (core porosity and permeability), and reservoir flow unit characteristics of the Permian-Triassic Upper Khartam Member of the Khuff Formation.

The specific objectives of this research include:

- Carrying out a detailed geometrical classification of porosity by which the pore types can be linked with their equivalent geometries. This classification can be utilized to understand the genetic pore types, texture, and their depositional facies.
- Examining the porosity and permeability relationships with consideration on their depositional texture to determine their degrees of heterogeneity.
- Conducting a detailed outcrop study to identify the reservoir units (flow units) and to determine their lateral continuity as well as the vertical relationship with the impermeable layers.

1.3. Problem Statement

Recently, the challenges of obtaining maximum hydrocarbon recoveries from carbonate reservoirs have become a serious issue. The high complexity of carbonate reservoirs and limited data within the inter-well space, make it difficult to characterize the flow units and to identify their lateral and vertical variations. In order to overcome this problem, outcrop approach is introduced to enable better evaluation, and to identify the variations within the inter-well space in the outcrop scale (100-1000 meters).

In addition, different scales of evaluation starting from outcrop scale (meter to hundreds of meters), rock samples (centimeter scale), core plug (centimeter scale), thin section (millimeter scale) and micro-scale using Scanning Electron Microscopy (SEM) images. To understand the reservoir heterogeneity better, small scale (thin section and SEM images) was used to evaluate and characterize the pore space especially the pore size, geometry, and connectivity. The bigger scale was used to describe the flow unit dimensions, and to identify the lateral and vertical facies changes.

Therefore, this study intends to use the outcrop of Upper Khartam Member of the Khuff Formation to study the porosity in general and carry out detailed characterization of the pore size, and pore geometry in order to rank the porosity types, and eventually to identify the best reservoir flow units.

CHAPTER TWO

LITERATURE REVIEW

2.1. Khuff Formation

2.1.1. Geology of the Khuff Formation

The Permian-Triassic Khuff Formation forms a series of outcrops extending NS in central Saudi Arabia with approximate length of 1,200 km (Steineke and Bramkamp, 1952; Steineke et al., 1958) (Figure 1.1d). Khuff Formation was first recognized by Steineke and Bramkamp (1952), and the type section was defined formally by Steineke et al. (1958) in the Ad Dawadimi quadrangle near town of Khuff in central Saudi Arabia (Figure 1.1d). However, Khuff Formation was recognized and mapped in the eighties by Saudi Geological Survey (SGS) and French Geological Survey (Bureau de Recherché Géologiques et Miniéres (BRGM)) (Vaslet et al., 2005).

The outcrop of Khuff Formation in the reference section overlies the Proterozoic Basement in Wadi Ar Rayn quadrangle (Powers et al., 1966) (Figure 1.1d). Delfour et al. (1982) proposed a revised type section of the Khuff Formation in Ad Dawadimi quadrangle, and then subdivided the Khuff outcrop into five members namely, from oldest to youngest as: Unayzah (Ash Shiqqah Member), Huqayl, Duhaysan, Midhnab, and Khartam members. These authors mapped the section in the type section in (1982) (see Figures 1.1d and 1.2).

The Khuff outcrops extend from north to south and dip to the east in central Saudi Arabia. To the south the Khuff outcrops unconformably overly the Precambrian Basement at Darma, Ad-Dawadimi, Wadi Ar Rayn, Wadi Al Mulayh, Sulayyimah, and Wadi Tathlith quadrangles (Vaslet et al., 2005) (Figure 1.1d). In the northern part of Saudi Arabia, Khuff outcrops overly the pre-Khuff formations forming angular unconformity due to Carboniferous orogeny (Figure 1.1d) (Powers, 1968; Wender et al., 1998; Le Nindre et al., 2002; Al-Husseini, 2004).

The oldest Member of the Khuff Formation is Ash Shiqqah Member (Unayzah Member) as defined by Delfour et al. (1982) in northern part of Ad Dawadimi quadrangle and later revised by Le Nindre et al. (1990b) (Figure 1.1d). Ash Shiqqah Member unconformably overlies Saq Formation (Cambrian- Ordovician) in north of Ad Dawadimi quadrangle (Figures 1.1d and 1.2). Senalp and Al-Duaiji (1995) introduced Ash Shiqqah as Formation and defined the type section in Buraydah quadrangle in area of Ash-Shiqqah, and they subdivided Ash Shiqqah Formation into two different units (lower and upper) which are separated by incised channels.

Huqayl Member of the Khuff Formation overlies Ash Shiqqah Member. The type section of Huqayl Member is located in Safra Huqayl in the Ad Dawadimi quadrangle (Figure 1.1d) (Delfour et al., 1982, Le Nindre et al., 1990b). Duhaysan Member which overlies the Huqayl Member has its type section located at Jabal Duhaysan (Delfour et al., 1982; Le Nindre et al., 1990b).

The type section of Midhnab Member which was reintroduced by Delfour et al. (1982) and revised by Le Nindre et al. (1990b) is located at Wadi Maghib in Ad Dawadimi quadrangle, close to Khuff town (Figure 1.1d).

Khartam Member, the uppermost Member of the Khuff Formation, was defined by Delfour et al. (1982) at its type section in Ad Dawadimi quadrangle in the NE of Khuff town (Figure 1.1d).

In the type section of Khuff Formation, the boundary between Khuff Formation and overlying Sudair Formation is not visible in the Ad Dawadimi quadrangle near town of Khuff in central Saudi Arabia (Delfour et al., 1982).

Ziegler (2001) described the lithostratigraphic succession, paleogeography, and related hydrocarbon habitats of Khuff Formation. According to this author, the lithostratigraphy of Khuff Formation is mainly controlled by interaction of eustasy and sediment supply in local and regional tectonics framework within the Arabian Plate margins. Khuff Formation mainly consists of carbonate and evaporates cycles, which are laterally continuous.

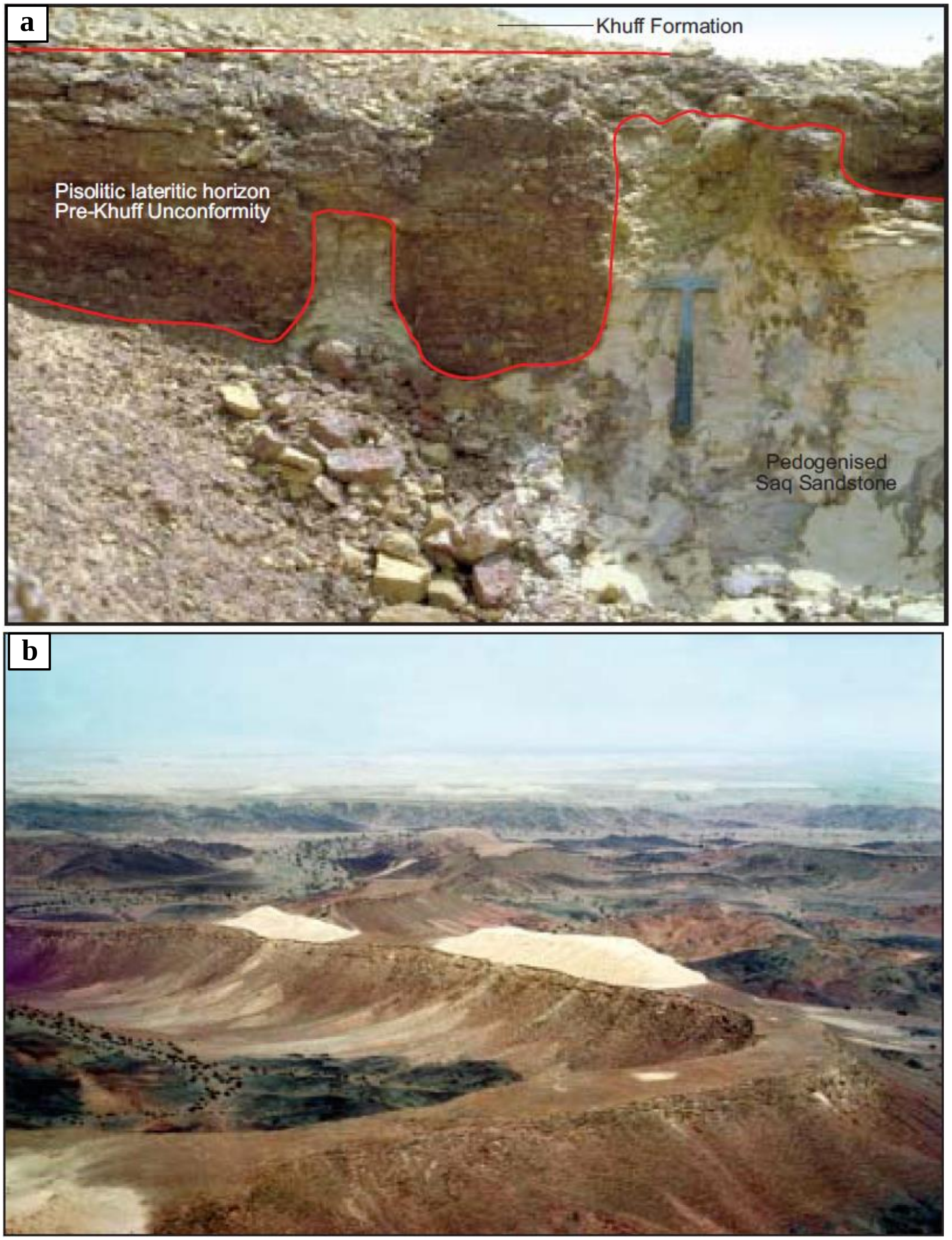

Figure 2.1: Pre-Khuff Unconformity (PKU). (a) A palaeosol horizon separate Saq Formation in the bottom from Khuff Formation in the top, Wadi Sajir area, Ad Dawadimi quadrangle; (b) Khuff Formation unconformably overlying the Proterozoic Basement, both Ash Shiqqah (gray colour) and Lower Huqayl (light colour) members are stand up of the Shield (blackish colour), Khnaigu'iyah area, Darma' quadrangle. (Both photos were taken by D. Vaslet, 1979).

2.1.2. Paleogeography

Khuff Formation is considered as the first major carbonate deposit in the Arabian plate (Konert et al., 2001). The carbonate deposits need shallow and clear water with moderate salinity and warm climate to deposit.

Beydoun (1993) suggests that during most of the Paleozoic Era, the Arabian, Iranian, and Anatolian (Turkey) plates together, formed the eastern part of Gondwana continental margin. During Permo-Carboniferous a time when the Gondwana supercontinent moved northward, the Arabian plate was located between 30º and 55ºS latitudes. The Arabian plate reached the location between 35º and 10ºS during late Permian, and continued to move northward and reached the 5ºN latitude in the early Triassic time to become equatorial with favorable climate for carbonate-evaporite accumulation (Figure 2.3) (Konert et al., 2001).

The separation of Arabian Plate from the Iranian-Anatolian Plate led to the formation of the Paleo-Tethys Sea in the early part of late Devonian to early part of Late Permian. At that time, the Paleo-Tethys Sea covered the areas that formed the present day Syria, Iraq, southern Turkey, and Iran (Figure 2.2) (Sharief, 1983; Ziegler et al., 1997).

In Carboniferous time, significant rifting took place along the eastern Gondwana margin and resulted to the opening the Neo-Tethys Sea. This rifting started from India (Garzanti and Sciunnach, 1997) to Oman (Al-Belushi et al., 1996). The Neo-Tethys Sea was developed to Neo-Tethys Ocean in the Middle Permian (Bechennec et al., 1990; Stampfli et al., 1991; Glennie, 2000) (Figure 2.4). With the opening of the Neo-Tethys Ocean, major transgression of the Neo-Tethyan water covered most of the Arabian plate (Al-

Aswad, 1997; Konert et al., 2001). This major transgression along with favorable climate allows the deposition and accumulation of shallow marine carbonates and evaporites of the Khuff Formation (Al-Jallal, 1989; Konert et al., 2001). This transgression continued to the Early Triassic time (Figure 2.4) (Al-Aswad, 1997).

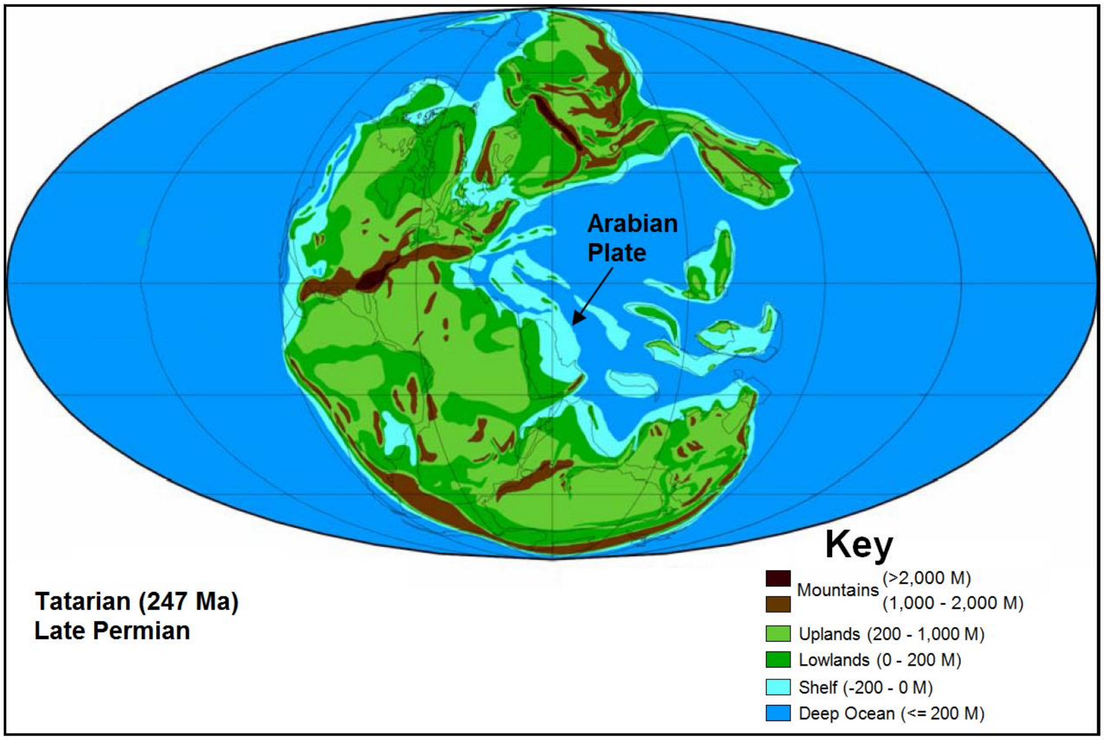

Figure 2.2: The topography of Gondwana in the Late Permian; the Arabian Plate was partially covered with Neo-Tethyan water (Ziegler et al., 1997).

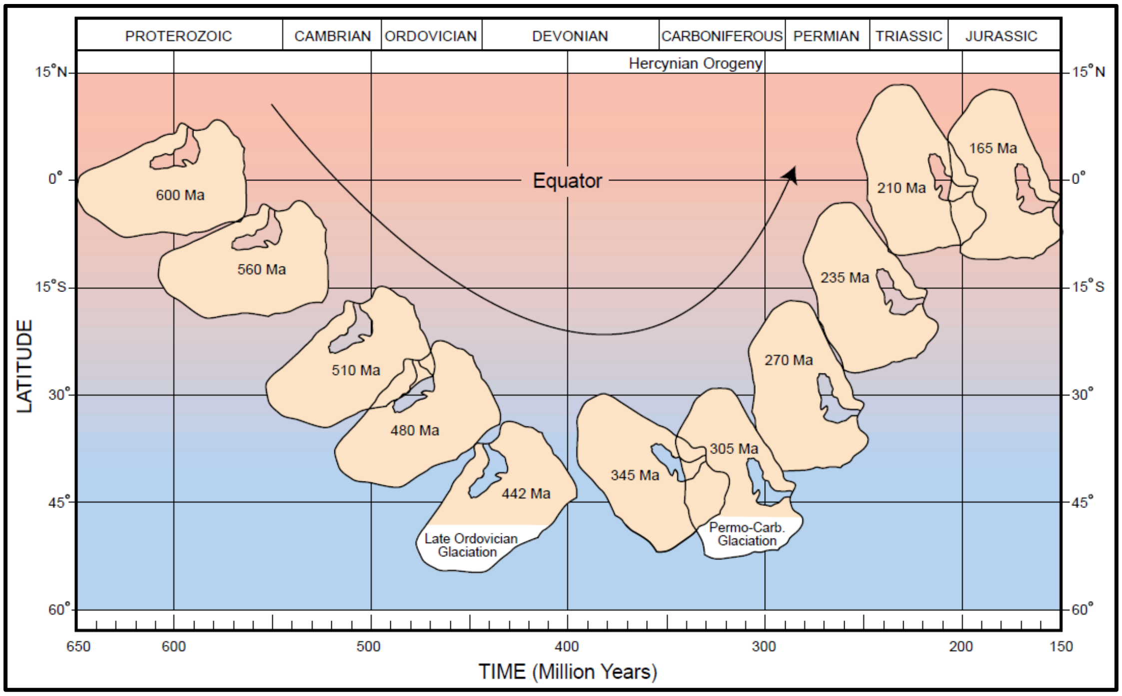

Figure 2.3: Paleolatitude positions of the Arabian Plate during Paleozoic and early Mesozoic (Konert et al., 2001).

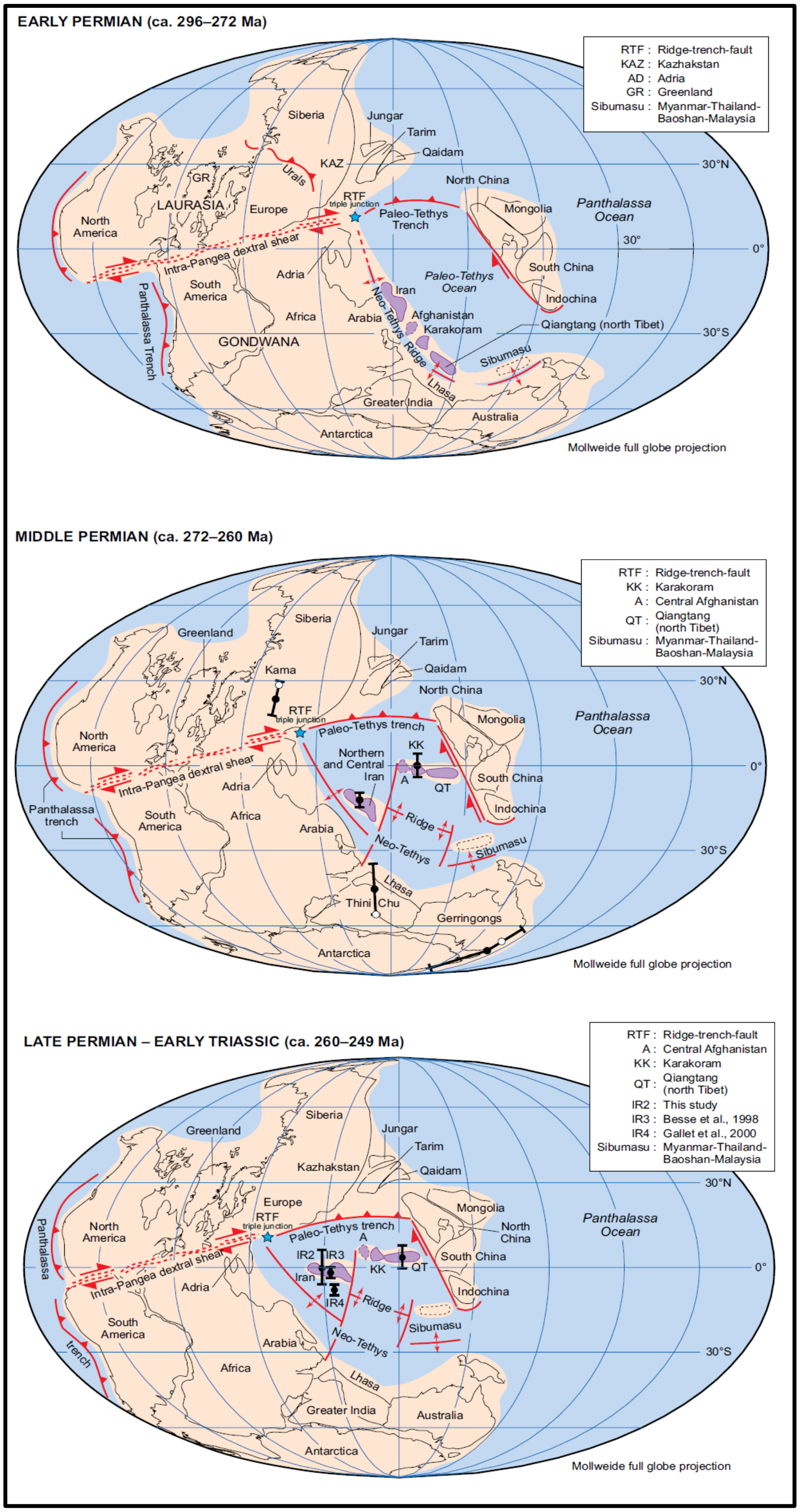

Figure 2.4: Paleogeographic maps showing the closing of Paleo-Tethys Ocean, and the development of the Neo-Tethys Ocean (Cogné, 2003).

2.1.3. Permian-Triassic Petroleum System

The Permian-Triassic petroleum system in the Gulf region contains huge amount of non-associated gas recovery which hold about 15-20 % of the non-associated gas reserves of the world. Khuff Formation outcropping in central Saudi Arabia (Vaslet et al., 2005), and to the east direction, extends into subsurface, where it forms an important reservoir of non-associated gas in Saudi Arabia, Iran, United Arab Emirates, Qatar, Oman, and Bahrain as well (Al Husseini, 2004; Alsharhan and Narin, 2003).

Understanding the geology of Khuff Formation is essential in terms of gas exploration and development in the Gulf region. Khuff carbonate is complex in terms of reservoir quality (porosity & permeability). The complexity is due to sediments formation, biological activities, mineralogy, susceptibility to extensive diagenetic changes, and stratigraphy. Therefore, the distribution of porosity and permeability is crucial in the prediction of the reservoir quality. Integration of different scales of observation starting from inter-well scale up to micro-scale at stratigraphic hierarchy will be helpful in the porosity and permeability prediction.

2.1.4. Depositional Environments

Khuff Formation represents a marine transgression during Permian-Triassic time (Figure 2.5). This transgression allowed the carbonate rocks of the formation to be deposited on the shallow continental shelf. Khuff Formation represents a deposition in flat carbonate ramp with huge extension within an arid climate like the present day climate in Arabian Gulf (Al-Jallal, 1995).

Khuff Formation in the subsurface has been subdivided into five units named from youngest to oldest as Khuff A, B, C, D, and E respectively (Figure 2.6). The lower Khuff E contains clastic deposits. Khuff A, B, C, D, and E represent cyclic deposition of sub-tidal carbonates during transgression, and intertidal and Sabkha deposits during regressive event, that perfectly formed shallowing-upward sequences of carbonate (Alsharhan and Nairn, 2003, Al-Jallal, 1995).

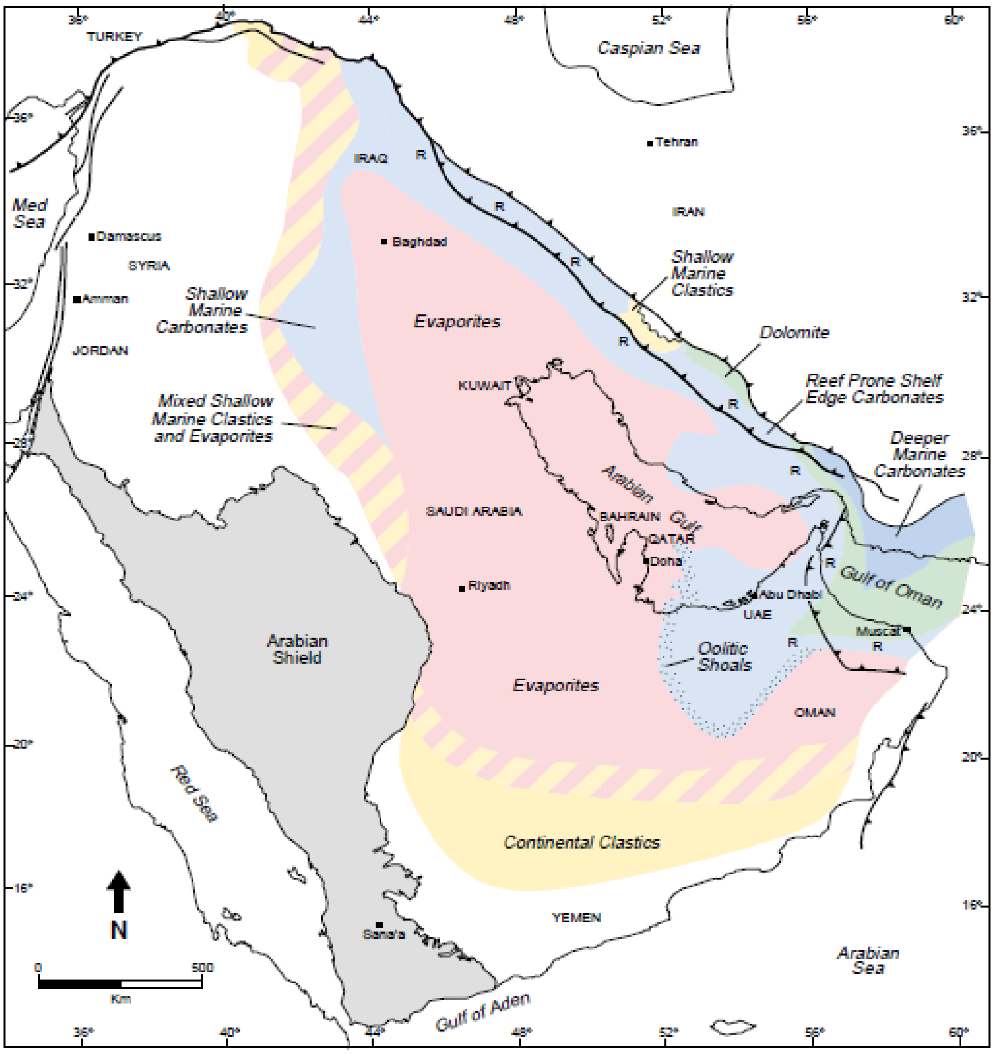

Figure 2.5: Paleogeographic map showing the depositional environments of the Khuff Formation during early Permian time (Konert et al., 2001 modified from Al-Jallal, 1995).

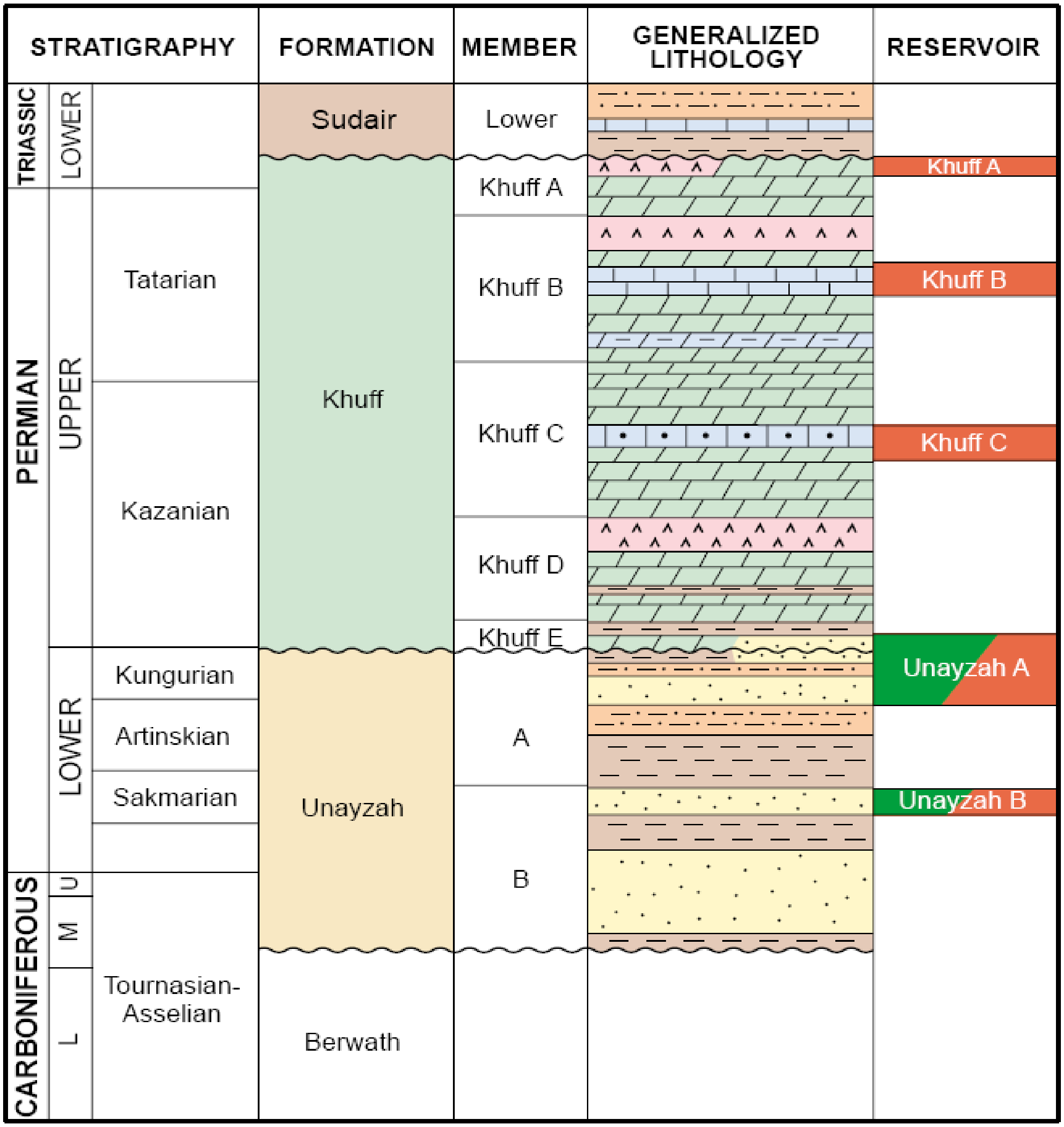

Figure 2.6: Carboniferous, Permian, and Lower Triassic parts of the late part of Paleozoic and early Mesozoic subsurface stratigraphic column of Saudi Arabia showing the Khuff A, B, C, D, and E (Dasgupta et al., 2002).

2.1.5. Regional Equivalents of the Khuff Formation:

Oman

Koehrer et al. (2012) did sedimentological and biostratigraphical works on the upper Saiq and lower Mahil formations that are considered the equivalent formations to the Middle and Upper members of the Khuff Formation (Koehrer et al., 2012). Their study was located at Oman Mountains in the Sultanate of Oman.

At the outcrop, the Permian–Triassic rock is subdivided into Saiq and Mahil formations (Glennie et al., 1973 and 1974) (Figure 2.7). Saiq Formation is mainly Permian. It considered as a time-equivalent to the Lower and Middle Khuff Formation. Whereas, Mahil Formation is mainly Triassic. Koehrer et al. (2012) identified eleven lithofacies with their depositional environment from the vertical sections that are located at Saiq Plateau, Wadi Hedek, Wadi Mistal, Wadi Bani Awf and Wadi Sahtan (see Table 2.1).

The boundary between the Saiq and the Mahil formations represent the Permian-Triassic boundary, which is defined by Rabu et al. (1986) and Coy (1997) as whitish-colored recessive step in the slope on the Saiq Plateau. Recently this boundary was defined by Koehrer et al. (2010) at Saiq Plateau.

United Arab Emirate

Maurer et al. (2009) studied the Bih Formation at outcrop in the Musandam Mountains in UAE. They prove the Bih Formation is the time equivalent to the Khuff reservoir. They used sedimentological and biostratigraphical approach to study the outcrop in Musandam island. From their study, nine lithofacies were identified with the interpretation (see Table

2.2). Their conclusion is the Bih Formation at outcrop is equivalent to the K3 to K1 reservoirs in the subsurface (North Dome/South Pars fields) (Figure 2.7).

Iran

Rahimpour-bonab et al. (2014) and Asadi-Eskandar et al. (2013) studied the Dalan and Kangan formations, which considered as time-equivalent to the Permian-Triassic Khuff reservoir (Alsharhan, 2006) (Figure 2.7). Their study was located at the South Pars Gas Field, in the Iran–Qatar border, Persian Gulf.

Rahimpour-bonab et al. (2014) did petrographic studies, petrophysical evaluations and geochemical analyses to delineate the intra reservoir barriers (IRBs). They identified eleven lithofacies with their depositional interpretation (see Table 2.3).

Asadi-Eskandar et al. (2013) constructed reservoir model for better permeability prediction. They distinguished 15 lithofacies from subsurface cores (see Table 2.4).

Table 2.1: The identified lithofacies of the time-equivalent of the Khuff Formation by Koehrer et al. (2013) in the Oman Mountains.

Koehrer et al. 2013 (Oman- Oman Mountains)	
Lithofacies	**Interpretation**
Burrowed to vertically rooted mud- to wackestone rooted mud- to wackestone	Low to moderate energy, shallow subtidal, protected inner ramp setting (backshoal); may experience exposure, reduced circulation and low sedimentation rates
Bioturbated mud- to wackestone	Low-energy outer ramp (offshoal) with strongly varying oxygenation, reduced circulation and low sedimentation rates
Microbial laminites	Low- to moderate energy, dominantly intertidal (more rarely subtidal) deposits
Graded wacke- to mudstone	Moderate- to high-energy storm sheets above SWB on the windward and leeward side of shoals
Graded pack- to wackestone	Moderate- to high-energy storm sheets above SWB on the windward and leeward side of shoals Intraclastic packstone
Intraclastic packstone (flakestone)	Moderate- to high-energy shallow subtidal storm deposits (channel fills, washover lobes); may be adjacent to muddy tidal flats
Intraclastic rudstone	Moderate- to high-energy shallow subtidal storm deposits (shoal margin)
Poorly-sorted peloid-rich pack- to grainstone	Moderate- to high-energy, shallow subtidal environment adjacent to sediment shoals (fore- and backshoal)
Poorly-sorted bioclast-rich pack- to grainstone	Moderate- to high-energy, deeper subtidal environment with normal marine circulation and variable sedimentation rates (fore- and backshoal)
Well-sorted oolitic /peloidal grainstone	Proximal to fully developed shoal or bar complexes within the high-energy midramp environment
Skeletal floatstone	Deeper water, outer platform deposits below SWB (offshoal)

Table 2.2: The identified lithofacies of the time-equivalent of the Khuff Formation by Maurer et al. (2009) in the Musandam Island in United Arab Emirates.

Maurer et la., 2009 (UAE-Musandam)	
Lithofacies	**Interpretation**
Bioturbated Dolomudstone to -Packstone	Moderate to low-energy environment of an open lagoon.
Laminated to Massive Dolomudstone and –Wackestone	Restricted, low-energy settings of the lagoon and nearshore mudflats (shallow subtidal to intertidal).
Pisolitic Dolopackstone	The combination of pisoids and reddish weathering of this facies suggests that it is related to subaerial exposure. It therefore represents the shallowest depositional environment among all studied facies.
Dolopackstone to -Grainstone with Staffelids	High-energy, most likely sand shoals. This facies is interpreted to have developed during a major flooding, when wave energy was high enough to remove most mud from the shelf.
Bioclastic Dolopackstone-Grainstone	Moderate to high-energy settings, most likely in leeward shoals of an open lagoon, as storm deposits and perhaps channelised tidal flat deposits.
Oolitic Dolograinstone	High-energy sand shoals facing and the outer shelf are the most likely depositional environment of this facies.
Thrombolitic Doloboundstone	The origin of this facies is microbial activity that was prolific at the Permian-Triassic boundary and in the lowermost Triassic on Peri-tethyan shelves (Baud et al., 2007; Kershaw et al., 2007).
Lithoclastic Dolograinstone-Packstone	A high-energy setting with frequent erosion and reworking of sediment most likely the sand shoals.
Mollusk Dolorudstone	Storm deposits.

Table 2.3: The identified lithofacies of the time-equivalent of the Khuff Formation by Rahimpour-Bonab et al. (2014) in the South Pars and Golshan gas fields in Iran.

Rahimpour-Bonab et la., 2014 (Iran-South Pars and Golshan gas fields)	
Lithofacies	**Interpretation**
Nodular Dolomudstone	Supratidal
Dolomudstone with Anhydrite Crystals	Supratidal- Intertidal
Dolomudstone (Dolomicrite)	Upper Intertidal
Fenestral Dolomudstone	Intertidal
Stromatolite & Thrombolite Boundstone	Intertidal -Subtidal
Pelloid- Bioclast Wackestone – Packstone	Lagoon
Ooid-Bioclast Packstone – Wackestone	Leeward Shoal
Ooid-Bioclast Grainstone – Packstone	Central Shoal
Coarse Bioclast-Intraclast Grainstone	Seaward Shoal
Bioclast Wackestone –Mudstone	Mid Ramp
Fine Bioclast Mudstone	Outer Ramp

Table 2.4: The identified lithofacies of the time-equivalent of the Khuff Formation by Rahimpour-Bonab et al. (2014) in the South Pars and Golshan gas fields in Iran.

Asadi-Eskandar et al., 2013 (Iran-Central Persian Gulf)
Lithofacies
Anhydrite (from massive to layer)
Mudstone often fenestrate/evaporate casts
Stromatolite boundstone
Wackestone to packstone (skeletal/peloid often with oncoids)
Oncoid, peloid packstone to grainstone
Fine-grained ooid, peloid grainstone
Medium-grained skeletal, ooid grainstone
Coarse-grained skeletal, intraclast grainstone
Beach barrier packstone to grainstone
Intra-formationa lconglomerate/collapse breccia
Bioturbated mudstone to wackestone
Dark argillaceous mudstone to claystone
Fossiliferous mudstone to skeletal wackestone
Shale to claystone
Thrombolite boundstone

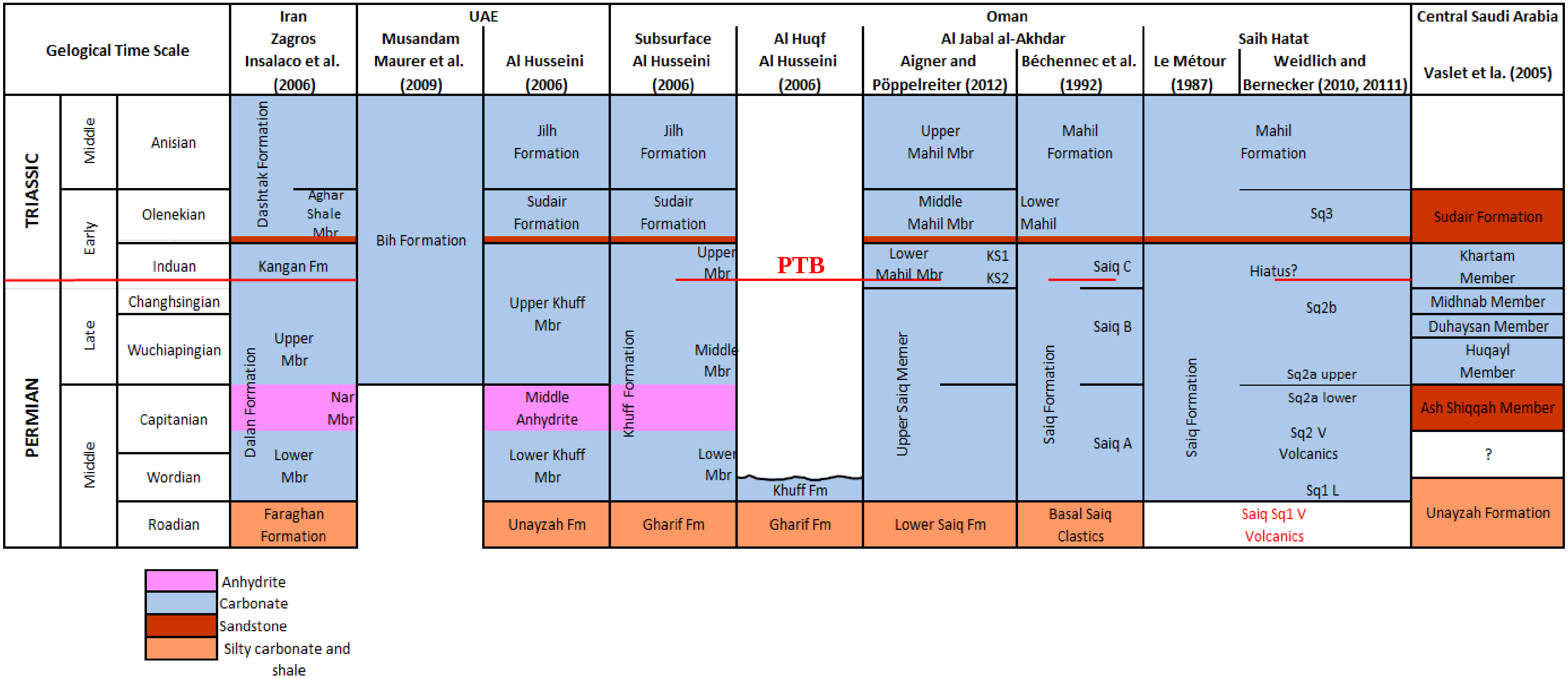

Figure 2.7: Regional correlation of the Permian-Triassic formations through the Gulf countries (modified from Baud and Richoz, 2013).

2.2. Petrographic Image Analysis (PIA)

Petrographic image analysis, a technique which has been used for siliciclastic studies since the early 90’s (Ehrlich et al., 1984; 1991a; 1991b), was recently applied to carbonate petrography (Anselmetti et al., 1998; Layman and Ahr, 2004). This technique has found various applications in grain texture, sorting, porosity, and mineralogical analyses. Petrographic image analysis is extensively used for identifying and classifying porosity.

Ehrlich et al. (1991b) used petrographic image analysis to extract a permeability model from porosity values from thin sections. Ehrlich et al. (1984; 1991a) also characterized the pore space and related the capillary pressure (using mercury injection) to the pore space and pore throat geometry by using images analysis technique in siliciclastic rocks.

Anselmetti et al. (1998) utilized digital image analysis to quantify carbonate porosity at different magnification levels to justify the permeability variations in carbonate rocks. Luo and Machel (1995) used normal optical petrographic microscope to identify mesoporosity and macroporosity, and environmental scanning electron microscope (ESEM) to identify microporosity.

Layman and Ahr (2004) used petrographic image analysis (PIA) to characterize porosity and identify the reservoir flow units in carbonate rocks. They measured the pore size, pore shape, frequency distribution for all types of porosity, and total porosity as well. Porosity data determined from petrographical methods, cores, and porosity logs were all compared with total porosity extracted from PIA to test the accuracy of their PIA. They also defined the reservoir pore facies by determining the pattern and trends (from porosity histograms) of the porosity.

2.3. Porosity Classification

Carbonate porosity types have been previously defined and classified (e.g., Archie, 1952; Choquette and Pray, 1970; Luo and Machel, 1995 and Ahr et al., 2005). These various classification schemes are briefly described as follows.

Archie (1952) developed a porosity classification for carbonate reservoirs. Archie's definition of the porosity was based on the texture and character of the visible porosity while his classification was based on the textural description of the rock and the visible porosity. He defined three textural types and four ranges of visible porosity. The textures are defined as type I, II, and III which represent muddy, chalky, and grainy rocks, respectively. The visible porosity range from Class A which shows no visible porosity to Class D with pores larger than 2 mm in diameter (Ahr, 2008).

Archie's classification ignored the relationship between rock types and pore origin, although some of the pores are opened or closed due to the diagenesis way long after deposition. In order to correlate and identify the spatial distribution of the reservoir interval (flow units), relationship between the petrophysical characteristics and rock type should be understood. This relationship was not considered in the Archie's classification (Ahr, 2008).

Choquette and Pray (1970) introduced a new practical classification. They grouped all identified porosity types into three classes; which are fabric selective, not fabric selective, and fabric selective or not (Figure 2.8a). Fabric selectivity means the carbonate porosity is controlled and does not cross the boundaries of the rock's grains, crystals, or any internal structures (Scholle and Ulmer-Scholle, 2003). However, the pores that cross the grains and crystals boundaries is classified under "not fabric selective, and fabric selective or not" (Figure 2.8b). This classification is highly practical and comprehensive. Also there is a list of genetic modifiers that were used to identify and describe the process, stage, and time of formation of porosity types as needed.

Luo and Machel (1995) described porosity as microporosity, mesoporosity, macroporosity, and megaporosity depending on the scale of observation. They succeeded in linking the crystal/particle sizes with pore size and pore-throat radii. Microporosity is the porosity with less than 4µ in size and this pore lies between the micrite crystals which is also less than 4µ in diameter. The connectivity of the pore throat radii is less than 0.5µ for oil reservoir and less than 0.1µ for gas reservoirs (Figure 2.9). Same idea applies to the mesoporosity, macroporosity, and megaporosity as shown in Figure 2.9. The significance of this classification is the incredible linking of the crystal/particle sizes, pore size, and pore throat radii that lies in different scales of magnification.

Ahr et al. (2005) introduced a better porosity classification by considering three processes including depositional, diagenetic, and fracture processes (Figure 2.10). Porosity types produced by depositional processes such as interparticle, fenestral, and shelter porosities are closely related to the original rock properties (depositional fabric and texture). Diagenetic processes like compaction, cementation, recrystallization, replacement, and dissolution may enhance or reduce the overall porosity or specific type of porosity. Fracture porosity is a kind of porosity that is formed as a result of the rock's failure due to differential stress on the rocks (Figure 2.10) (Ahr et al., 2005). By relating the pore origin to the pore geometry, this classification can be used to model the distribution of porosity and permeability in three dimensions, and based on that, flow units can be identified and ranked.

Ahr’s classification considered the Hybrids 1, 2, and 3 kinds of pores denoted as H1, H2, and H3 (Figure 2.10). Hybrid 1 (H1) represents the depositional pores that were affected by diagenesis. Hybrid 2 (H2) is that kind of diagenetic pores influenced by fractures. Hybrid 3 (H3) is a depositional pore influenced by fractures (Figure 2.10). Later, Humbolt (2008) modified Ahr’s classification and divided each Hybrid pore (H) into three parts A, B, and C. Therefore the new subdivisions are as follows: Hybrid 1 contains H1-A, H1-B, and H1-C; Hybrid 2 consists of H2-A, H2-B, and H2-C; and lastly Hybrid 3 is comprised of H3-A, H3-B, and H3-C. For example, Humbolt (2008) divided Hybrid 1 into A, B, and C depending on the degree of alteration or the amount of diagenesis, which include H1-A, H1-B, and H1-C. In Hybrid 1-A (H1-A), the pores which are still depositional pores, are strongly controlled by the depositional facies and original texture. Hybrid 1-B (H1-B) is a case where the porosities are equally controlled by the depositional and diagenetic features. In Hybrid 1-C (H1-C) the diagenetic features are dominant factor that control the porosity, and consequently the diagenetic features are control the distribution of the flow units.

Ahr’s classification can be further classified as enhanced or reduced, depending on the diagenetic changes through geological time by just adding the letter ‘r’ for porosity reduction or ‘e’ for porosity enhancement. For example here a H1-C pore that was enhanced, the new notation will be H1-Ce.

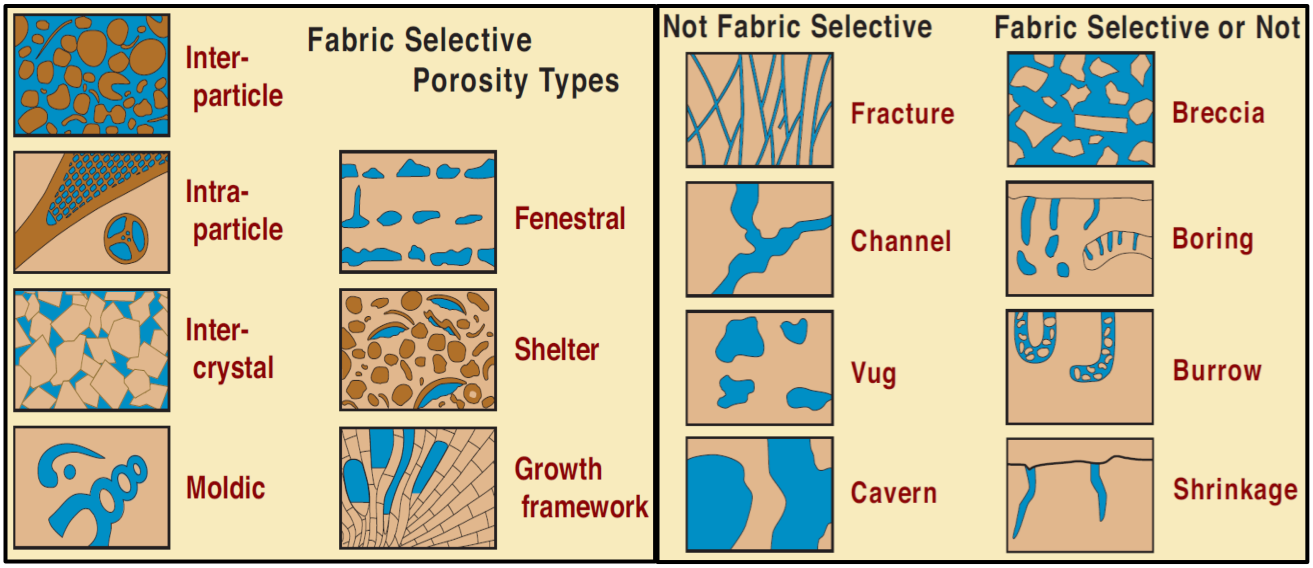

Figure 2.8: Carbonate porosity classification of Choquette and Pray (1970) (modified by (Scholle and Ulmer-Scholle, 2003) from (Choquette and Pray, 1970)).

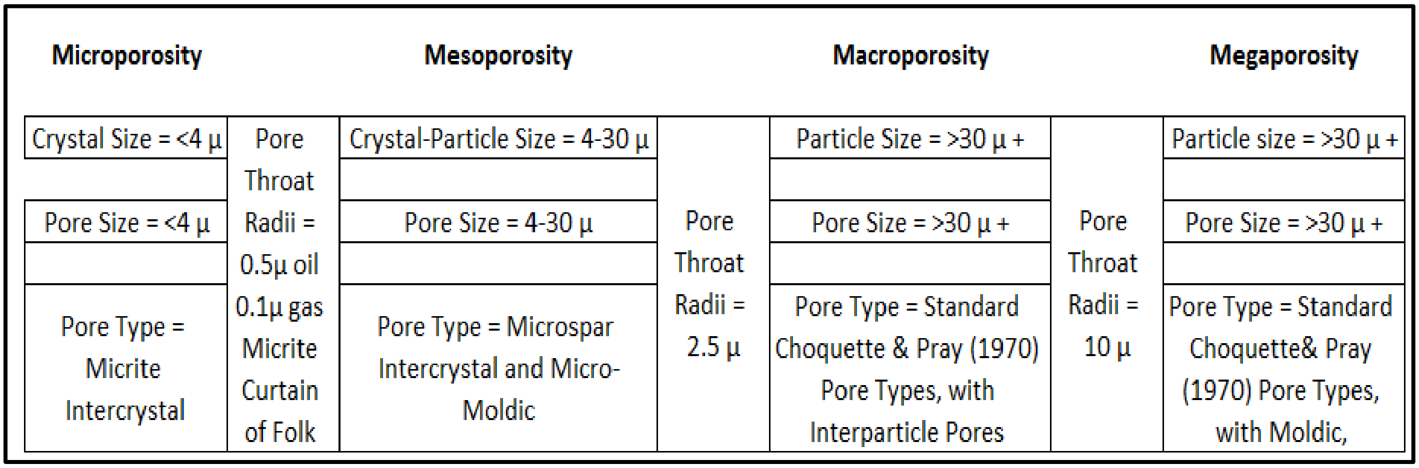

Microporosity		Mesoporosity		Macroporosity		Megaporosity
Crystal Size = <4 μ	Pore Throat Radii = 0.5μ oil 0.1μ gas Micrite Curtain of Folk	Crystal-Particle Size = 4-30 μ	Pore Throat Radii = 2.5 μ	Particle Size = >30 μ +	Pore Throat Radii = 10 μ	Particle size = >30 μ +
Pore Size = <4 μ		Pore Size = 4-30 μ		Pore Size = >30 μ +		Pore Size = >30 μ +
Pore Type = Micrite Intercrystal		Pore Type = Microspar Intercrystal and Micro-Moldic		Pore Type = Standard Choquette & Pray (1970) Pore Types, with Interparticle Pores		Pore Type = Standard Choquette& Pray (1970) Pore Types, with Moldic,

Figure 2.9: Microporosity, mesoporosity, macroporosity, and megaporosity as defined by Luo and Machel (1995).

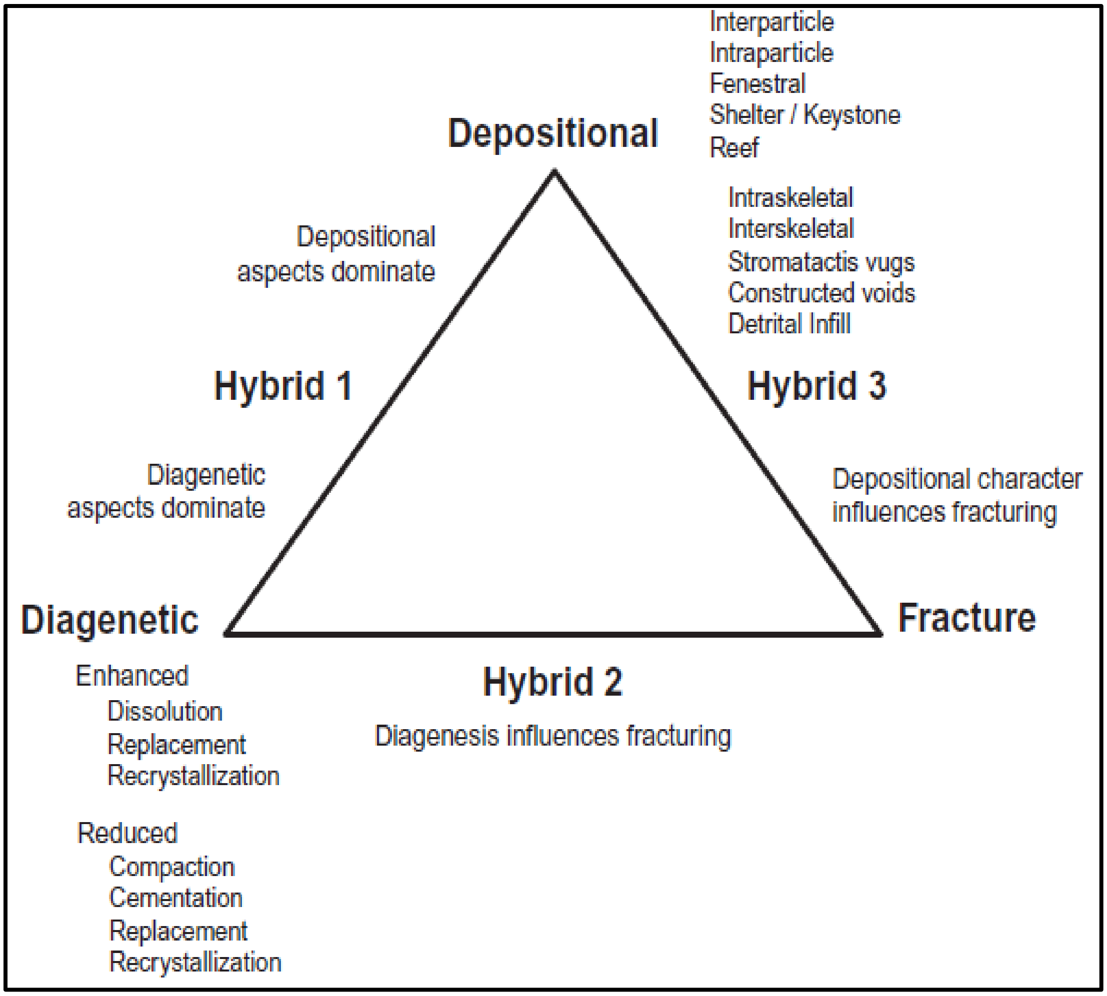

Figure 2.10: A genetic classification for carbonate porosity (Ahr et al., 2005).

CHAPTER THREE

METHODOLOGY

3.1. Introduction

The methods used in this study consist of extensive field works, measurements of both porosity and permeability from core plugs, thin section description. Using JMicroVision 1.2.7 Software, petrographic Image Analysis (PIA) was used to analyze selected thin section samples. Scanning Electron Microscopy (SEM) imaging was also carried out on representative samples for microporosity.

3.2. Field Work

The field investigation targeting Upper Khartam Member of Khuff Formation was carried out in the At Tarafiyah area, north of Buraydah town, Al-Qasim region, central Saudi Arabia. Detailed description for outcrop sections, and sampling were conducted during the field investigations. The field description was used to identify the reservoir units (grainy layers) by tracing the lateral extension (length) and vertical thickness. Visible variations in facies within the flow units at outcrop scale were also identified, and finally, all the field data were superimposed into panorama images. A series of photos were taken to build panorama picture covering the whole outcrop. The pictures were merged to form a complete photomosaic (panorama) of the outcrop (Figure 4.10) using Adobe Photoshop CS5 software.

3.3. Laboratory Work

3.3.1. Porosity and Permeability Measurements

Horizontal and vertical core plugs drilled from representative outcrop samples were used to carry out the petrographic description, porosity, and permeability measurements. All of these measurements were used to evaluate the potential reservoir units.

Plugs taken were 1 in. (2.5 cm) in diameter and approximately 3 in. (7.5 cm) in length. Porosity and permeability measurements were made for each core plug using water saturation method. Core porosity was calculated by measuring the weight of dry samples and subtracting the measurement value from the weight of the wet samples. Samples were placed in water of known density under vacuum to make sure that all the pores were filled with water. Permeability was also measured using the water saturation method by injecting the water with known properties through the core and measuring the amount of water that went through the core at different time intervals.

3.3.2. Thin-Section Petrography

Thin sections were prepared from representative outcrop samples using the standard thin section preparation technique. Detailed thin section petrography was carried out to identify the visible grains, porosity, cement, and matrix under optical petrographic microscope.

3.3.3. Petrographic Image Analysis (PIA)

Objective and Equipment:

Representative samples were analyzed using JMicroVision software. These samples selected from the reservoir units and non-reservoir units. In this part, the main concern was to identify the porosity and classify the pore size and geometry (aspect ratio and roundness) for different types of porosity, and also to quantify and qualify the different types of porosity based on pore sizes and geometry. Selection of the right magnification to identify small sizes of both pores and grains was carefully considered. Images were captured using microscopic camera and relayed to the computer and saved as (.tif) format for further analyses.

Calibration and Sampling Procedure:

In order to carry out petrographic image analysis (PIA), the right magnification for focusing, and light properties (source type, intensity, and polarity) were standardized to ensure the comparability of all thin section images.

In order to cover the entire thin section and to make imaging more consistent, each thin section was subdivided into approximately eight to ten images (depending on the chosen magnification). JMicroVision 1.2.7 software was used to curry out the visual porosity estimation for each image of the entire thin section, and then the average porosity was calculated for all images of the entire thin section.

Measurements

Based on blue epoxy coloration of the pores, the pores in the thin section images were manually digitized using JMicroVision 1.2.7 software. Manual detection of the pore was done by applying 2D measurements and selecting the polygon icon, pressing and moving the cursor around the pores. This procedure was repeated until all the pores in the image were identified. Finally, the software was used to identify the different parameters such as area, perimeter, length, and width. These parameters were subsequently used to quantitatively estimate the visual porosity. Pore size in (μm^2) is equivalent to the area in the software. Total porosity (visual estimation) of the images was obtained by subdividing the total pore areas over the area of the entire image. This is called Total Optical Porosity (TOP) (Ehrlich et al., 1984). Pore shape was determined based on the aspect ratio (length\width) and roundness factor ($\text{perimeter}^2 / 4 \pi a$; where a represents the pore area) (Layman, 2002). Using the aspect ratio, we can deduce whether the pore is elongated (aspect ratio > 1.5) or equidimensional (aspect ratio 1.0-1.5), the roundness factor can indicate whether the pore is rounded (roundness factor = 1.0-3.0) or angular (roundness factor > 3). The combination of both aspect ratio and roundness factor can provide excellent interpretation of the pore shape. If the pore has an aspect ratio between 1.0 and 1.5 and the roundness factor range form 1.0-3.0, it is considered as a circular shape. If the pore has an aspect ratio of 1-1.5 and roundness factor above 3.0, it is considered as a square shape. When the pore's aspect ratio is above 1.5 and its roundness factor ranges from 1.0-3.0, then the shape is elliptical, and also when the pore has an aspect ratio >1.5 and roundness factor > 3.0, a rectangular shape is the best interpretation (Layman, 2002).

3.3.4. Scanning Electron Microscopy (SEM)

Representative samples were selected for scanning electron microscopy (SEM) to identify microporosity, grain shape, cement, and matrix. SEM was performed in the fresh side of the selected samples. Gold was used as coating materials to avoid any reaction (Goldstein and Yakowitz, 1975). SEM is essential in this study to address the micro-scale heterogeneity within the lithofacies.

3.3.5. Powder X-ray Diffraction (XRD)

Powder X-ray diffraction was performed on representative samples to identify the mineral composition for each lithofacies. Selected samples were crushed and powdered. Each of the powdered samples was placed in sample holder with a 20 µm square capacity. The scan range was fixed from 10 to 90 degrees to cover wide range of identification. The scan parameters are illustrated in Table 3.1. The Standard Measurement software (Rigaku package) is synchronized with the personal computer (PC). The data of the standard measurement software were saved in data format. And subsequently processed using PDXL2 integrated X-ray powder diffraction software to match the peaks with the minerals in the database of the ICDD PDF software. The complete report for the analysis for each sample containing the XRD signature, measurement conditions, qualitative analysis results, the peak list and other parameters was exported to MS word file.

Table 3.1: Measurement conditions used in the powder X-ray diffraction's instrument.

X-Ray	30 kV , 15 mA	Scan speed / Duration time	2.0000 deg./min.
Goniometer		Step width	0.0200 deg.
Attachment	-	Scan axis	2theta/theta
Filter		Scan range	10.0000 - 90.0000 deg.
CBO selection slit	-	Incident slit	1.25 deg.
Diffracted beam mono.	Fixed Monochromator	Length limiting slit	-
Detector	MiniFlex2 counter	Receiving slit #1	1.25 deg.
Scan mode	CONTINUOUS	Receiving slit #2	0.3mm

CHAPTER FOUR

LITHOFACIES AND SEQUENCE STRATIGRAPHY

4.1. Introduction

Vaslet et al. (2005) recorded three lithofacies in the Upper Khartam Member which include: 1) stramatolite mats; 2) coquina; and 3) planar oblique oolitic grainstone. These three lithofacies were interpreted to have been deposited in very shallow marine environment of intertidal flat in infra- and mid-littoral (foreshore to backshore) depositional environments. In a recent study in the same locality (At Tarafiyah area), Eltom et al. (*in prep*) provided more refinement of the previous studies with more evidence of the depositional environment and lithofacies.

Eltom et al. (*in prep*) described ten lithofacies from the Upper Khartam Member and assigned them to different depositional environments. These facies are: poorly sorted intraclast grainstone (backshoal fringing shoal intercalation), bimodal cross-bedded oolitic fossiliferous grainstone (Backshoal fringing shoal intercalation), graded pack-mudstone (Foreshoal), spill-over channel (Foreshoal), well-sorted oolitic grainstone (Shoal and shoal bars), thinly bedded Marl Limestone alternating with grainstone (Backshoal fringing shoal intercalation), poorly-Sorted dolomitic skeletal oolitic grainstone and packstone (tidal flat), heterolithic (tidal flat), microbial laminites (Supra tidal flat), and burrowed poorly sorted skeletal oolitic (Beach). These lithofacies were grouped into five high frequency sequences.

Eltom et al. (*in prep*) subdivided the Upper Khartam Member into five high frequency sequences (HFSs). The outcrop studied for this thesis is located within the HFS-4. Four vertical sections and a lateral section investigated show the HFS-4 in details. The summary of the depositional environment of these five high frequency sequences according to Eltom et al. (*in prep*) is illustrated in Figure 4.4.

4.2. Facies Description:

4.2.1. Well-Sorted Oolitic Grainstone Facies

This facies is characterized by brownish to whitish color and rough surface in the outcrop, with lack of any significant fractures. This facies is erosive at the bottom and cross bedded at the top. The facies is composited of 50 to 200 cm thick, well-sorted oolitic molds (Eltom et al. (*in prep*)). Vertical repetition of well-sorted oolitic grainstone facies is common with some changes in thickness. Some intervals of this facies are continuous and other are truncated or pinched out laterally.

Thin section study shows this facies is mainly composite of oolitic grains with minor skeletal grains. The diameter of the ooids is range from 0.2 to 0.5 mm. The main porosity types are moldic and vuggy porosity dominated by oolitic molds (Figures 4.1a and 4.1c). Moldic and vuggy porosities are affected by partially/total cement filling. However, pores with no cements inside are dominant. Micro-fractures in thin section scale are relatively rare and the recorded micro-fractures are completely filled with calcite cement (Figures 4.1b and 4.1e) and some are open (Figure 4.1f). This facies is affected by dolomitization appear in fabric preserved dolomite (Figure 4.1f).

4.2.2. Cross-bedded Oolitic Skeletal Grainstone Facies

In outcrop, this facies shows clear reddish to brownish color with rough surface. There were not any significant fractures observed in the outcrop scale. The ooid and skeletal molds can be observed from the hand specimen or core plugs. The thickness varies from 20 to 40 cm. This facies shows typical cross bedding indicating high energy setting. Well-rounded oolitic grains, peloids, and bivalve, gastropods fragments are the typical grains types in the facies (Eltom et al. (*in prep*)).

Thin section study shows this facies is mainly composite of oolitic and skeletal grains mainly bivalve with some gastropod. The diameter of the ooids is range from 0.2 to 0.5 mm and more than 1 mm for skeletal grains (Figure 4.2). The main porosity types are moldic and vuggy porosity dominated by oolitic molds (Figure 4.2c). Moldic and vuggy porosities are affected by partially/total cement filling. Micro-fractures in thin section scale are not present. This facies is affected by dolomitization appear in fabric preserved dolomite (Figure 4.2f).

4.2.3. Graded Mudstone to Packstone Facies

Yellowish to whitish colors mudstone, wackestone and packstone beds. This facies show massive to laminated and cross bedded strata. In outcrop, the fractures in this facies are filled with gypsum. While the micro-fractures in the thin section completely filled with calcite cement (Figures 4.3a and 4.3c).

In thin section, this facies show pure mudstone with no visual porosity, scattered skeletal and non-skeletal grains of wackestone and packstone (Figure 4.3). The main porosity type in this facies is vuggy porosity. Intercrystalline porosity is mainly occurs in association with dolomite crystals. Micro-fractures are often present in the muddy beds but all the encountered micro-fractures are filled with calcite cement (Figures 4.3a and 4.3c). Unlike other facies, the dolomitization in this facies is enhancing the porosity especially in the packstone texture (Figures 4.3e and 4.3f).

4.3. High Frequency Sequences (HFSs) with their Depositional Environment:

The HFS-1 started with marine transgression mudstone in the lower part followed by foreshoal fine grained sediments and overlain at the top by thick shoal and shoal bars grainstone. HFS-2 has thick fine muddy carbonate sediments in the lower and middle parts representing foreshoal deposits. Coarse sediments found at the top of this HFS are characteristic shoal and shoal bars deposits. HFS-3 and HFS-4 show almost similar lithofacies. HFS-5 mainly shows deposits of tidal flat and backshoal sub-environments. Figure (4.4) summarizes the sub-environments of each of the high frequency sequences.

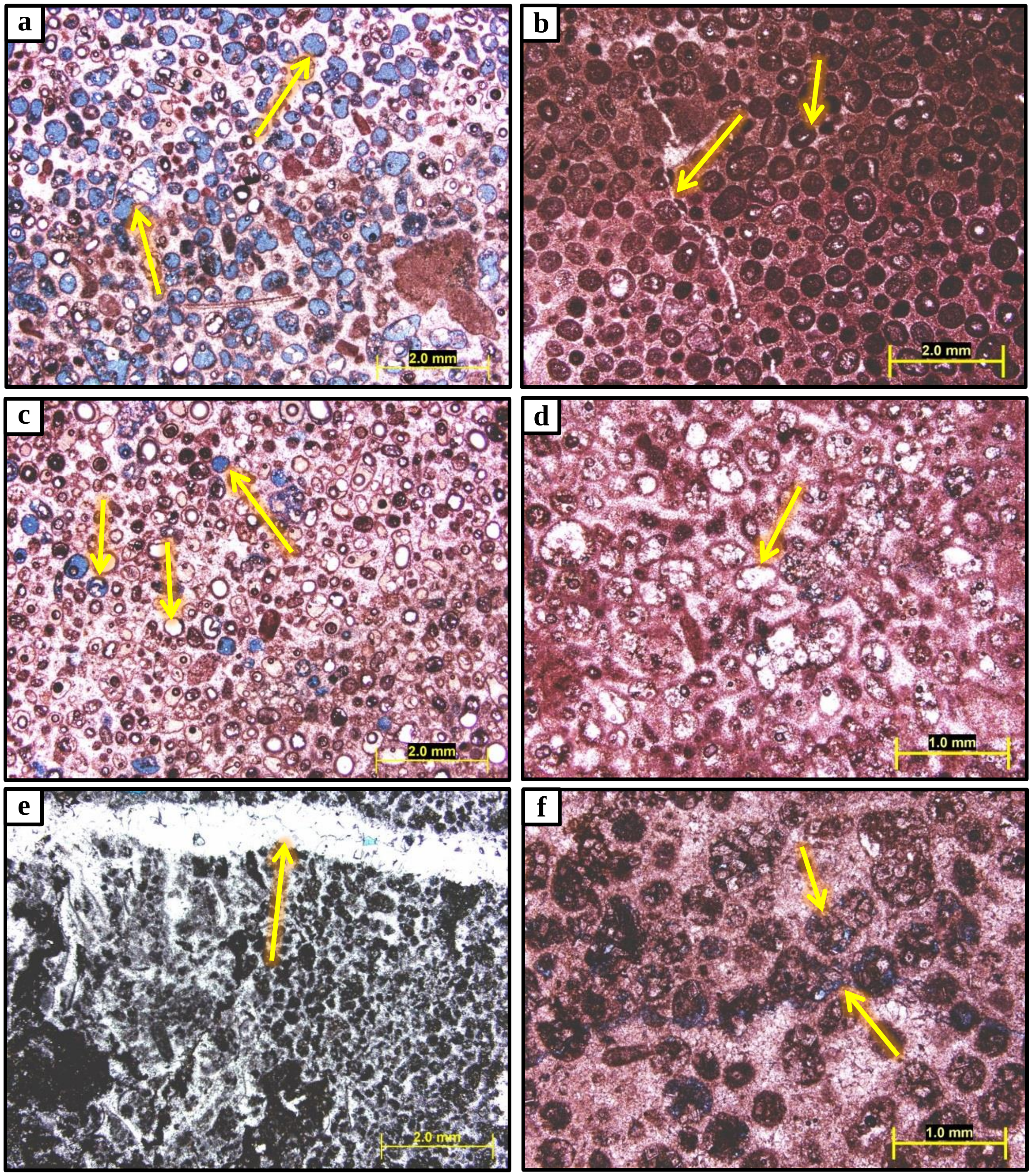

Figure 4.1: show well-sorted oolitic grainstone facies in the thin section showing well rounded ooids (b) and (c) to little bit elongated in (a) and (d). Moldic and vuggy porosities show no cements, partially and completely cemented pores in (a), (c) and (d). Micro-fractures are completely filled with calcite cement as in (b) and (e) but sometimes the micro-fractures are open in association with dolomitization like in (f). Dolomitization is shown in (f) which occur as dolomite cement attack the oolitic molds.

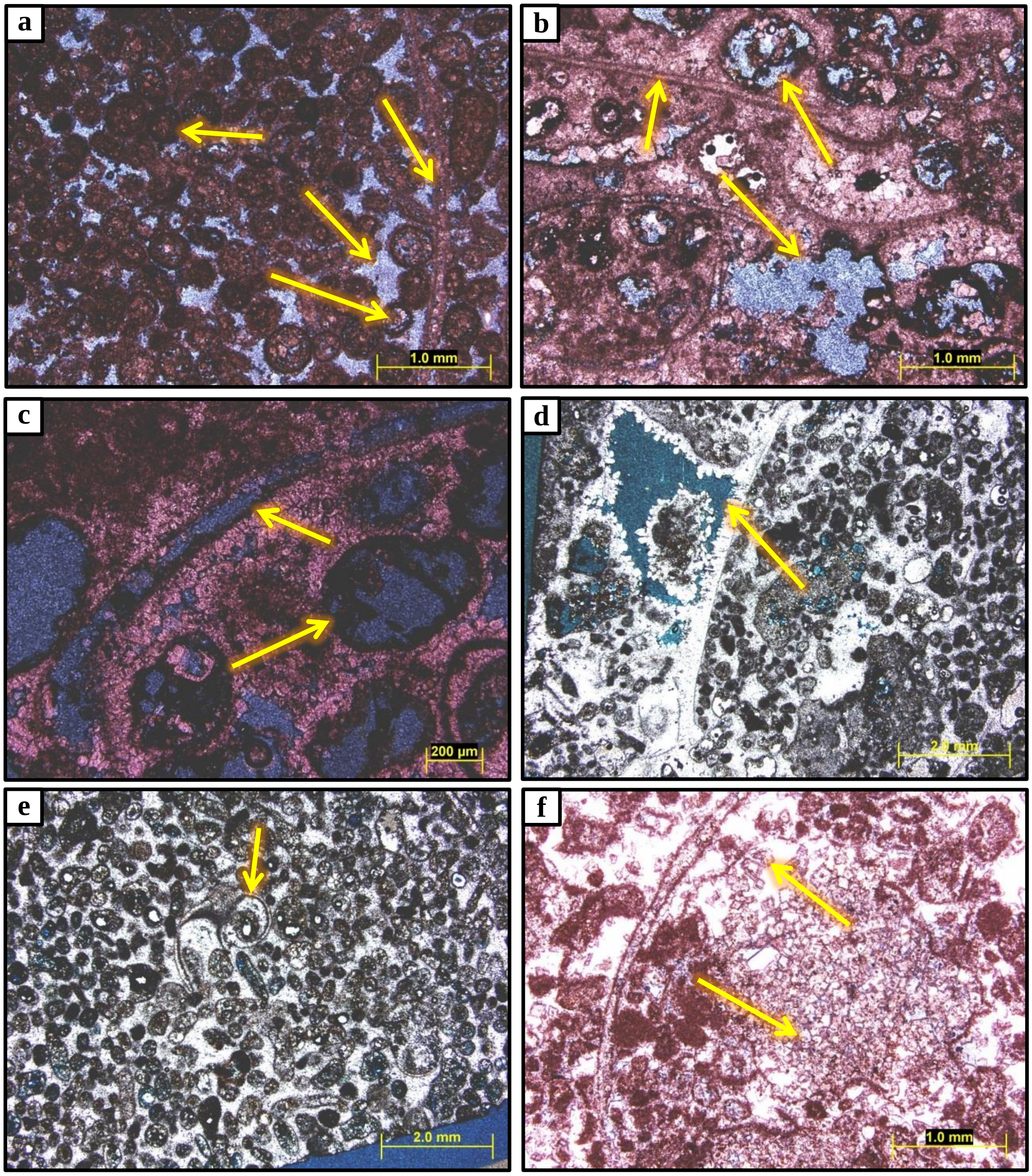

Figure 4.2: show cross-bedded oolitic fossiliferous grainstone facies in the thin section showing well rounded ooids as in (a), (c), (d) and (e) and some skeletal grains as in (a), (b), (c), (d), (e) and (f). Moldic porosity is present as dissolution of oolitic and skeletal grains as in (c). Vuggy porosity is also dominant in this facies as in (b) and (d). Intergranular and intragranular porosities (as in (a)) are rare to find in this facies. Dolomitization is shown in (f) which occur as dolomite cement attack the oolitic and skeletal grains.

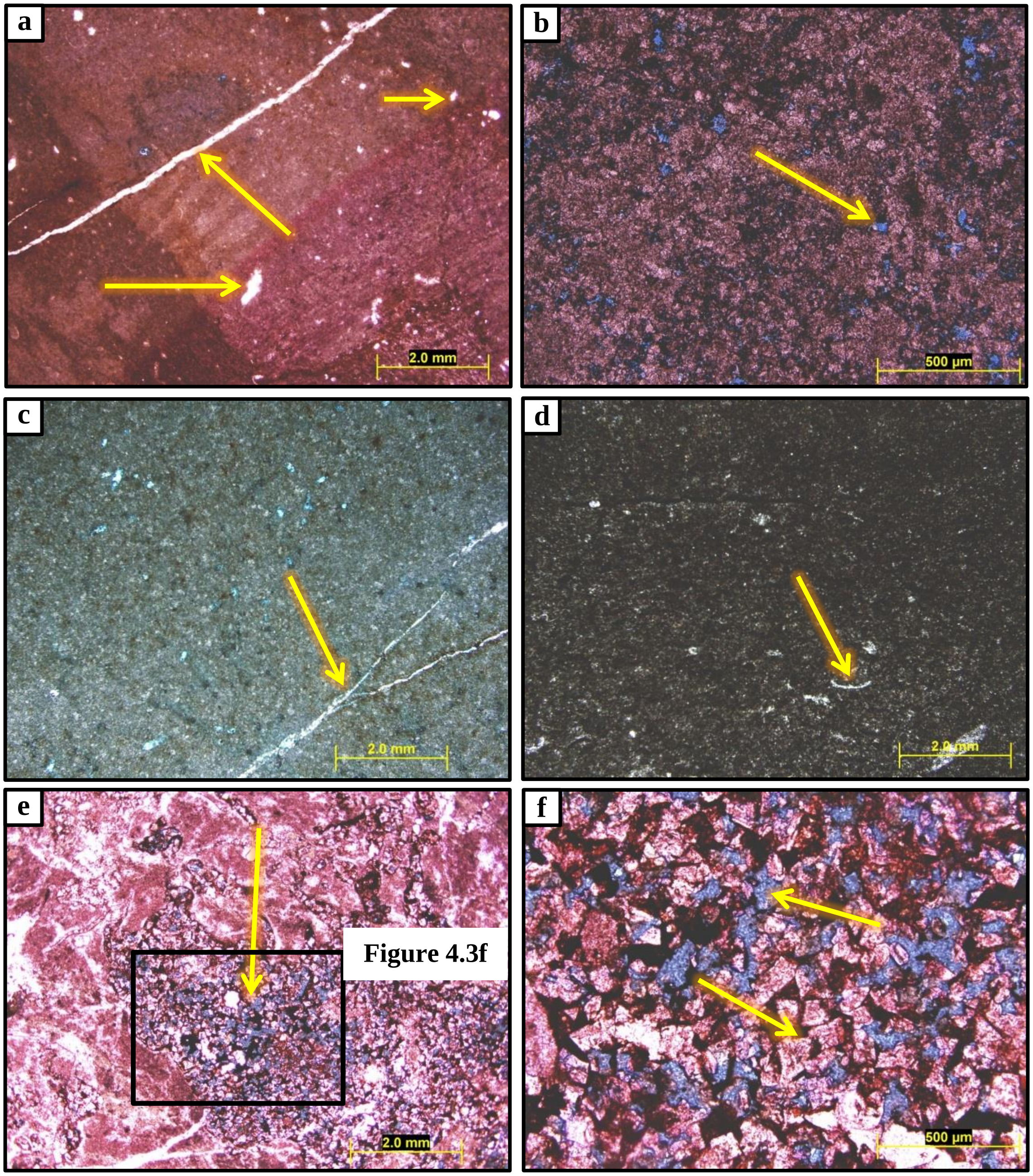

Figure 4.3: show graded mudstone to packstone facies in the thin section showing mainly mud with some skeletal and non-skeletal grains as in (a), (d) and (e). Vuggy porosity is the dominant pore type as in (b) and (c). Intercrystalline porosity is mainly associated with dolomite crystals as in (f). Micro-fractures are present in this facies but it completely filled with calcite cement as in (a) and (c). Dolomitization is shown in (e) and (f) which enhance the overall porosity.

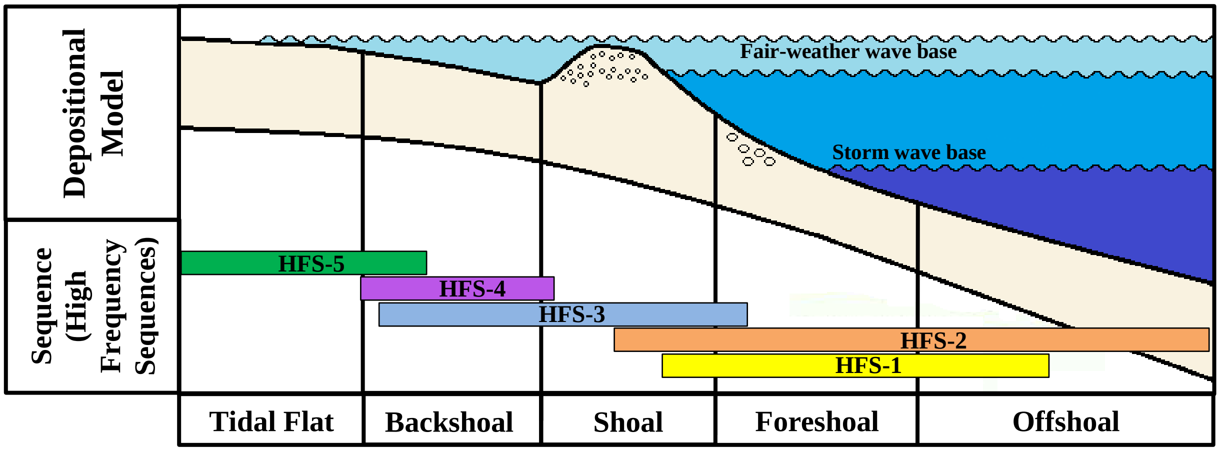

Figure 4.4: Distribution of the high frequency sequences (HFSs) of the Upper Khartam Member within their depositional environment in the carbonate ramp model (modified from Eltom et al. (*in prep*)).

4.4. Outcrop Description:

Four vertical sections were described and sampled bed by bed in the field (Figures 4.6, 4.7, 4.8 and 4.9). The locations of these vertical sections and the panorama images are illustrated in Figure 4.5. Complete description of the vertical sections is given below.

4.4.1. Vertical Section # 1:

This section is located at 26°25'38.31"**N** 44° 0'11.50"**E** (see Figure 4.6). This section is 9.5 meters thick of interbedded mudstone/grainstone carbonate layers. All the sequences present in this section are belonging to the HFS-4.

This section is comprised of eight shallowing-upward, coarsening upward and thinning upward 3rd order high frequency sequences. In the bottom, a thin white color massive mudstone and thick beds of grainstone that contain four stylolite surfaces, are grouped together to form the first sequence. This sequence disappeared at approximately 35 meter in the dip direction (NEE direction). This sequence is overlain by two beds of yellowish massive/laminated mudstone and oolitic grainstone with recognizable moldic porosity. The overlying sequence contains a thick bed of yellowish to reddish mudstone interbedded with thin beds of grainstone. Laterally, the grainstone beds are thicker than the mudstone beds. The thin sequence contains yellowish massive mudstone and oolitic grainstone, laterally becomes thinner until they pinch out at the dip direction. This sequence is overlain by soft yellowish massive to weakly laminated mudstone and 50 cm thick grainstone that maintains the same thickness laterally. Two repeated sequences of mudstone-grainstone are present at the top of this section.

4.4.2. Vertical Section # 2:

The location (26°25'40.30"**N** 44° 0'15.96"**E**) of this section is shown in Figure 4.7. This section which is approximately 6.5 meters thick is composed of six 3rd order high frequency sequences. All the sequences appearing in this section are considered as parts of the HFS-4.

A half meter thick mudstone-grainstone sequence occurs at the bottom of the section. The second sequence is comprised of massive to laminated mudstone and massive grainstone. This was followed by yellowish layers of massive to laminated mudstone and brownish oolitic grainstone (clearly distinguished by ooid molds). The 1-meter thick of mudstone-grainstone layers shows some heterogeneity and complexity. Two sequences of repeated mudstone-grainstone layers characterized great heterogeneity in thickness and in lithology laterally is found at the top of the section.

4.4.3. Vertical Section # 3:

The location (26°25'42.85"**N** 44° 0'19.69"**E**) of this section is shown in Figure 4.8. This section which is approximately 8.2 meters thick occurs at the upper part of HFS-4, 4th order sequence boundary and the lower part of HFS-5.

This section starts with four sequences within the HFS-4. These sequences are characterized by interbedded mudstone and grainstone layers that are laterally very heterogeneous in thickness and lithology. A distinctive fourth order sequence boundary that separated the HFS-4 from HFS-5 and characterized by soil horizon followed this sequence. Laminated mudstone and thin grainstone bed overly this fourth order sequence boundary. Laminated to massive yellowish to reddish mudstone layers and grainstone bed formed the second sequence in the HFS-5. Massive to weakly laminated mudstone is encountered at the bottom of the third sequence in the HFS-5. The overlying grainstone has recognizable moldic and vuggy porosity. Lastly, reddish mudstone and brownish grainstone beds are present in the last sequence of this section.

4.4.4. Vertical Section # 4:

The location (26°25'44.18"**N** 44° 0'22.32"**E**) of this section is shown in Figure 4.9. This section which is approximately 6.5 meters thick, contains a set of sequences that form the upper part of the HFS-4 and the lower part of HFS-5 with 4th order sequence boundary.

The section commences with very thick grainstone beds with stylolite surfaces. A fourth order sequence boundary overlies the grainstone beds. The HFS-5 portion of the sections commences with massive beds of yellowish mudstone and brownish grainstone. Weakly laminated mudstone and relatively thick grainstone layers which constitute the second sequence of the HFS-5 is also present within the section. Thin layers of laminated mudstone and grainstone form the third sequence of the HFS-5 in this location. Massive yellowish mudstone and grainstone with high amount of moldic and vuggy porosity are the characteristic of the fourth HFS-5. The vertical section ends with thick grainstone that contains mudstone patches.

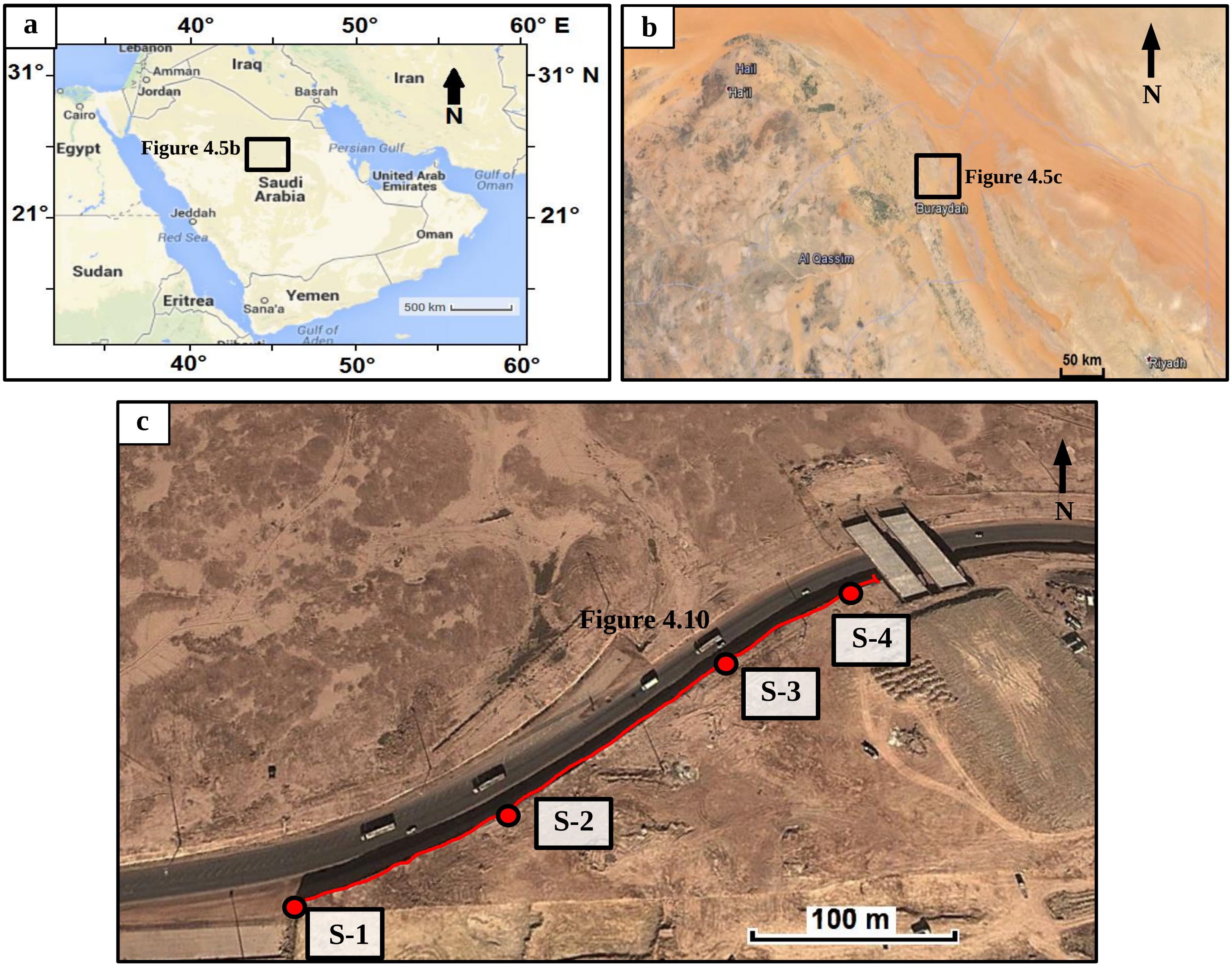

Figure 4.5: (a) Map showing the location of the study (area highlighted with black box) in the central Saudi Arabia; (b) close look of the region of the study area; (c) map showing the road cut of the studied outcrop with locations of the four vertical sections and the panorama image (Google Maps, 2013).

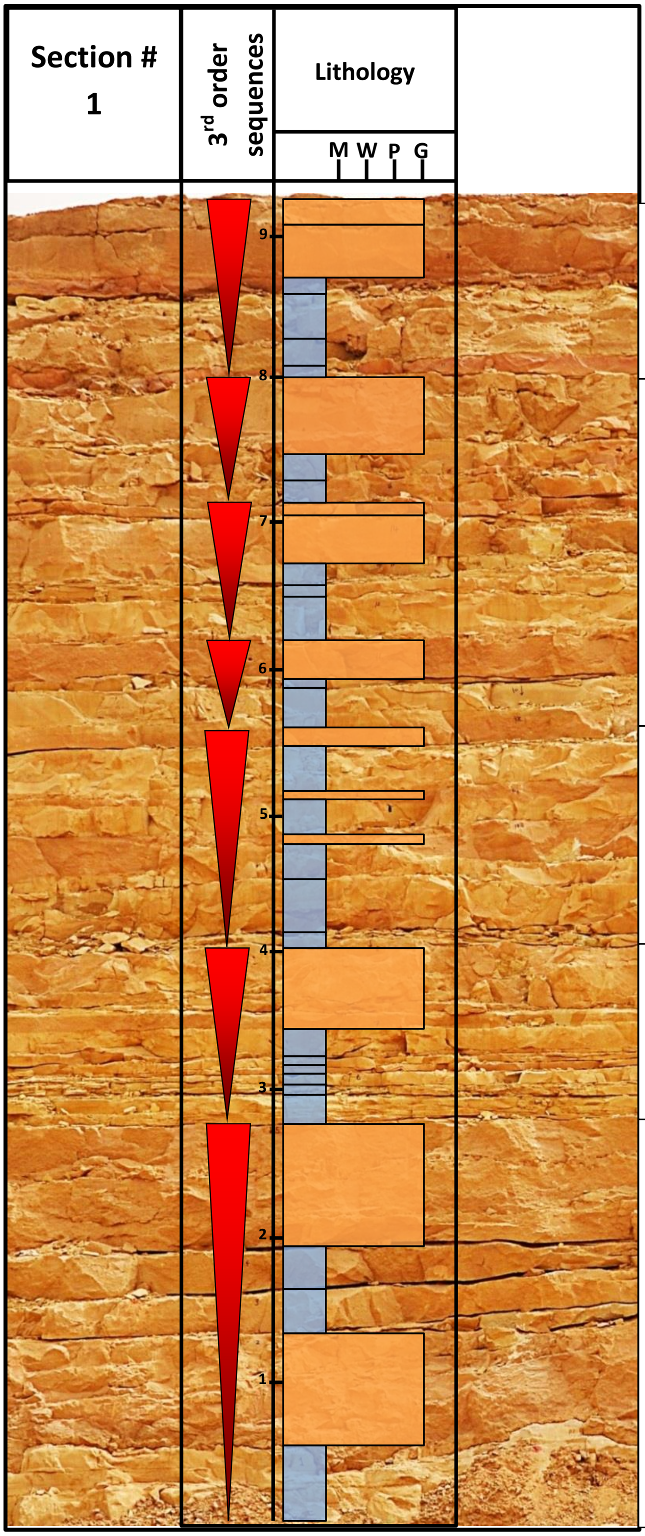

Massive reddish and yellowish beds of mudstone overlain by massive brownish grainstones beds.

Interbedded massive mudstone and grainstone beds.

Yellowish/reddish thick beds of mudstone interbedded with thin brownish grainstone.

Yellowish laminated mudstone and brownish massive oolitic grainstone bed.

Thickly beds of oolitic grainstone contain stylolite surfaces. The mudstone beds are thick and massive, but laterally become thin and laminated.

Figure 4.6: showing the first vertical section with the outcrop picture and the description.

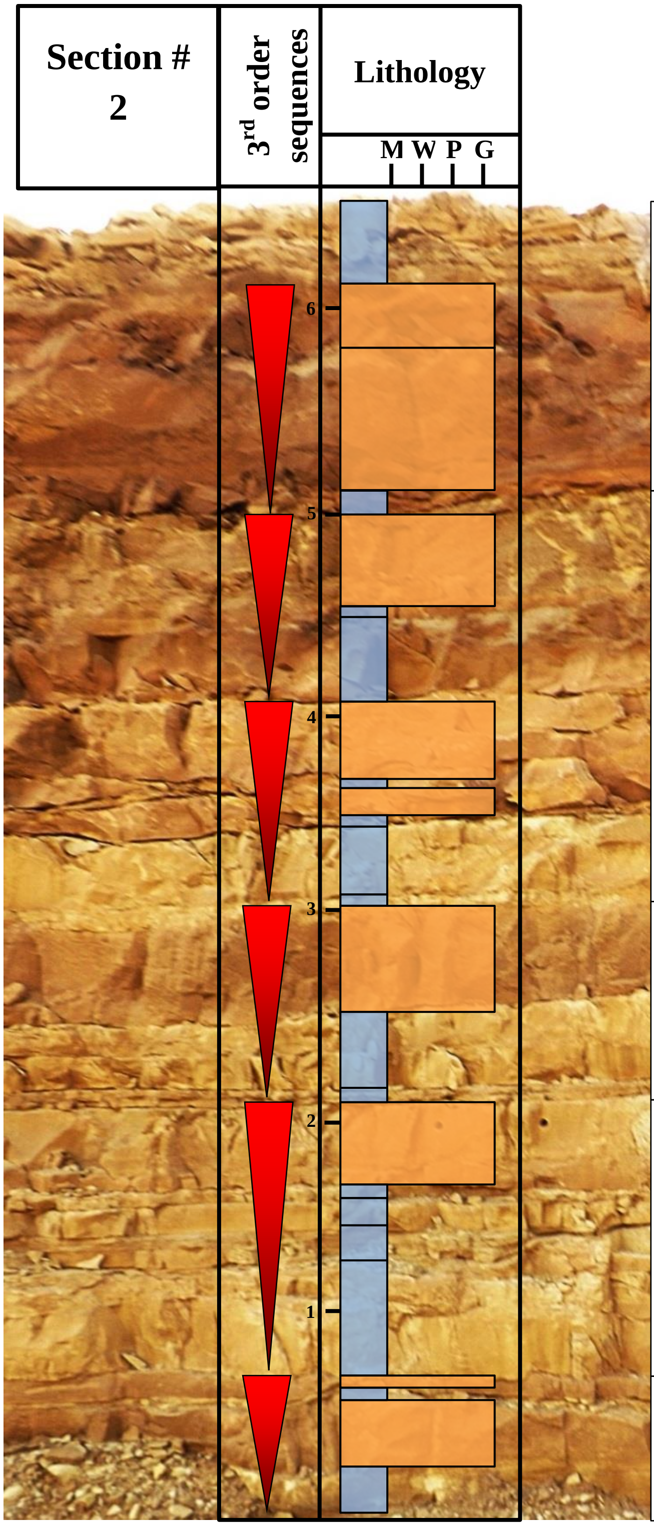

Thick beds of grainstone with complex in colors and degree of black inclusions. The mustone beds are laminated with yellowish color.

Interbedded massive mudstone and grainstone beds. The mudstone beds have reddish and yellowish colors, whereas grainstone beds are brownish color. This bed set are very complex and heterogeneous in term of bed boundaries, colors and composition.

Massive/laminated mudstone overlie by dark brownish oolitic grainstone bed.

Interbedded of massive mudstone and laminated mudstone, overlained with oolitic grainstone. Laterllay, mudstone beds become interbedded with thin grainstone beds.

Yellowish massive mudstone bed overlain by brownish grainstone interbedded with laminated mudstone.

Figure 4.7: showing the second vertical section with the outcrop picture and the description.

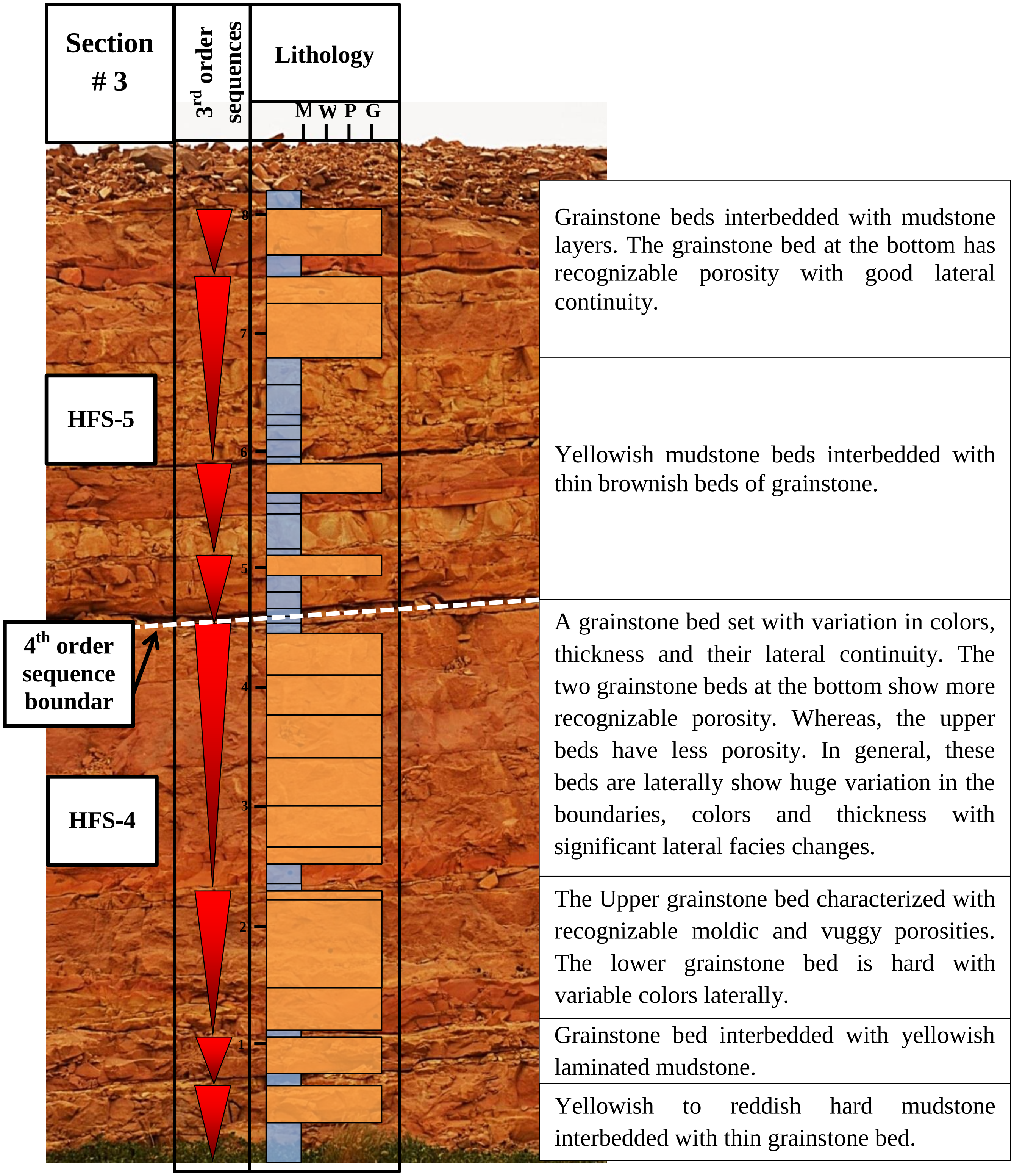

Grainstone beds interbedded with mudstone layers. The grainstone bed at the bottom has recognizable porosity with good lateral continuity.

Yellowish mudstone beds interbedded with thin brownish beds of grainstone.

A grainstone bed set with variation in colors, thickness and their lateral continuity. The two grainstone beds at the bottom show more recognizable porosity. Whereas, the upper beds have less porosity. In general, these beds are laterally show huge variation in the boundaries, colors and thickness with significant lateral facies changes.

The Upper grainstone bed characterized with recognizable moldic and vuggy porosities. The lower grainstone bed is hard with variable colors laterally.

Grainstone bed interbedded with yellowish laminated mudstone.

Yellowish to reddish hard mudstone interbedded with thin grainstone bed.

Figure 4.8: showing the third vertical section with the outcrop picture and the description.

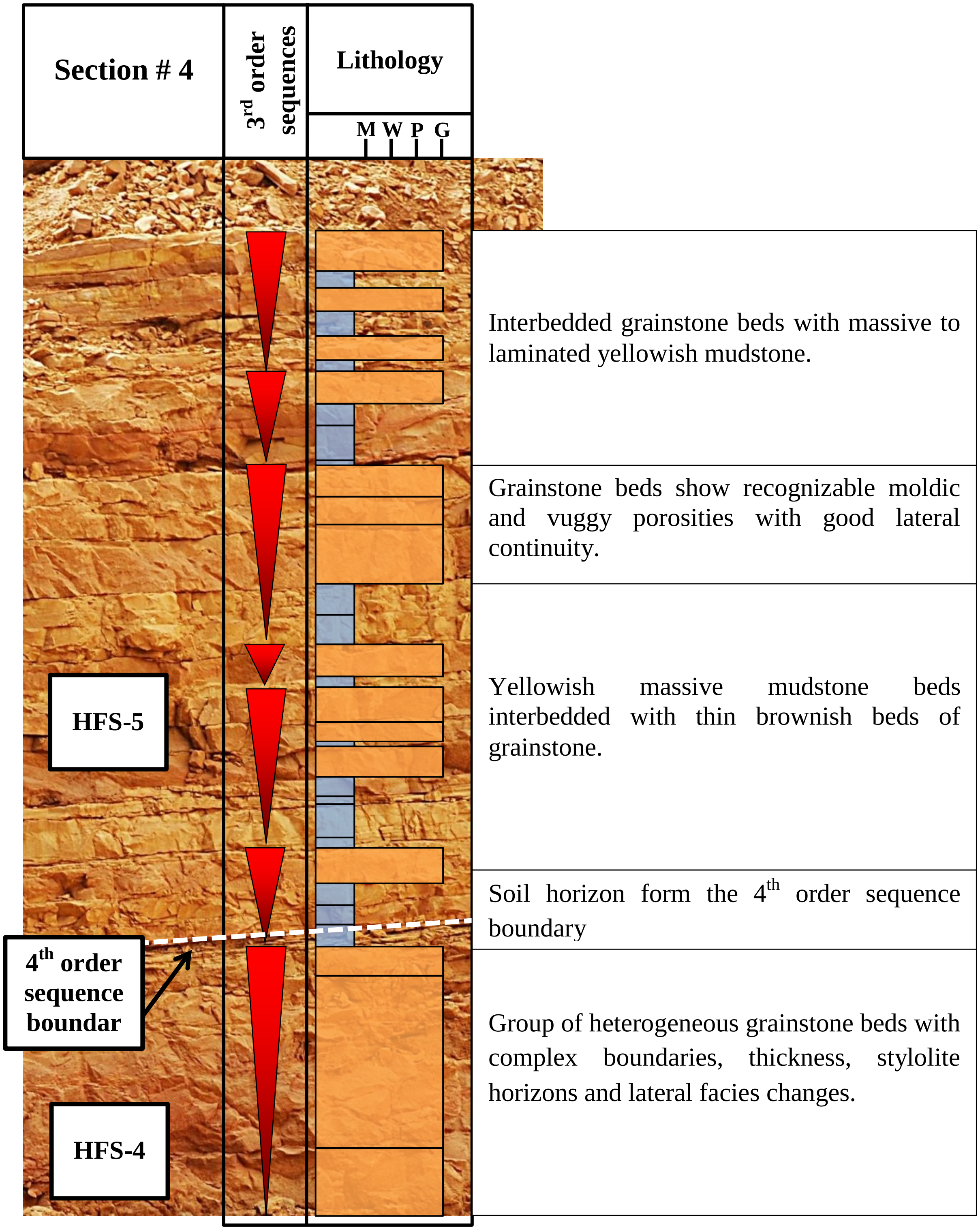

Interbedded grainstone beds with massive to laminated yellowish mudstone.

Grainstone beds show recognizable moldic and vuggy porosities with good lateral continuity.

Yellowish massive mudstone beds interbedded with thin brownish beds of grainstone.

Soil horizon form the 4th order sequence boundary

Group of heterogeneous grainstone beds with complex boundaries, thickness, stylolite horizons and lateral facies changes.

Figure 4.9: showing the fourth vertical section with the outcrop picture and the description.

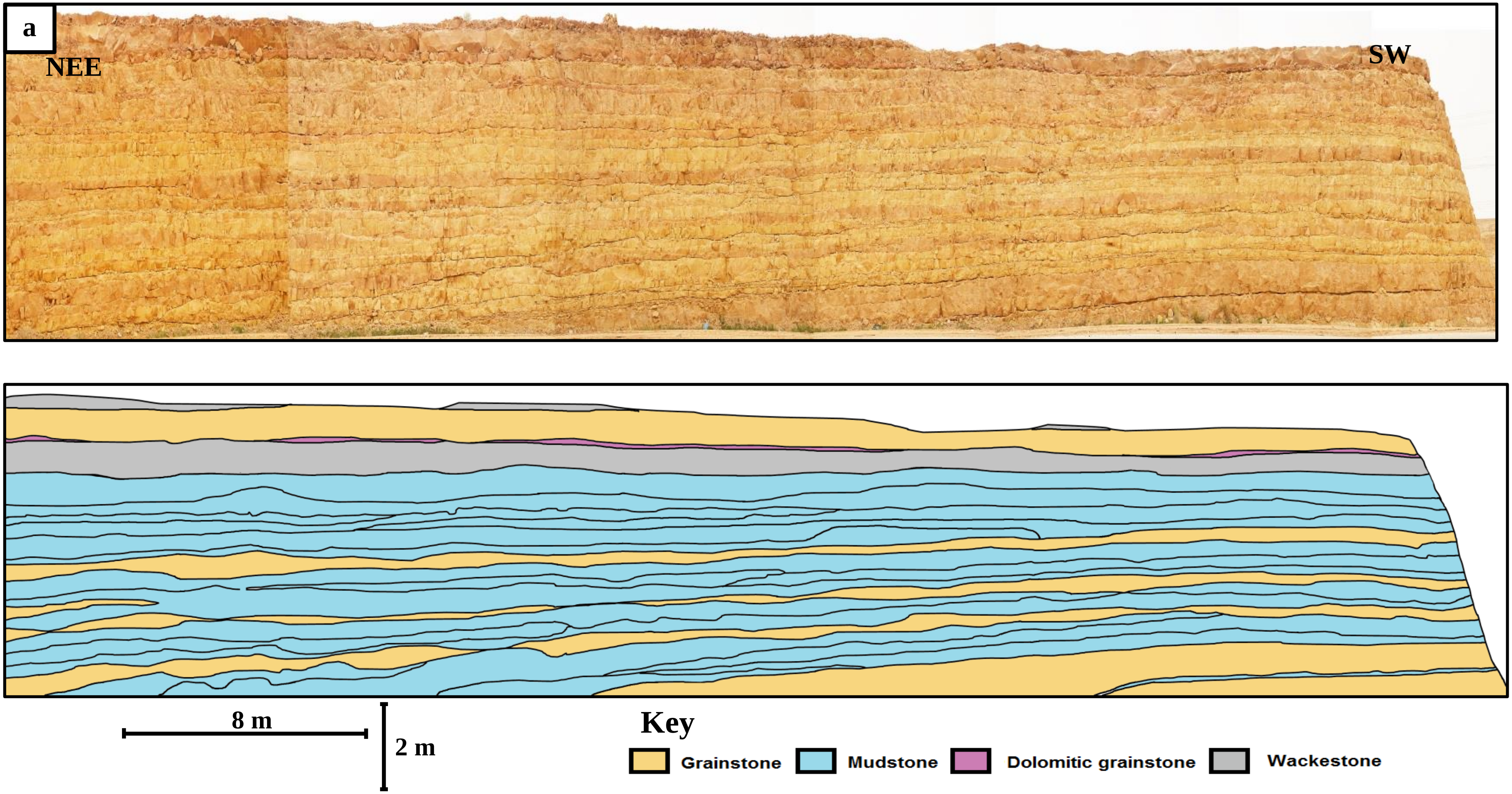

Figure 4.10: the panorama images for the 400 meters extended outcrop with their simplified lithological model. The NEE of each panorama is overlapped with the SWW in next panorama.

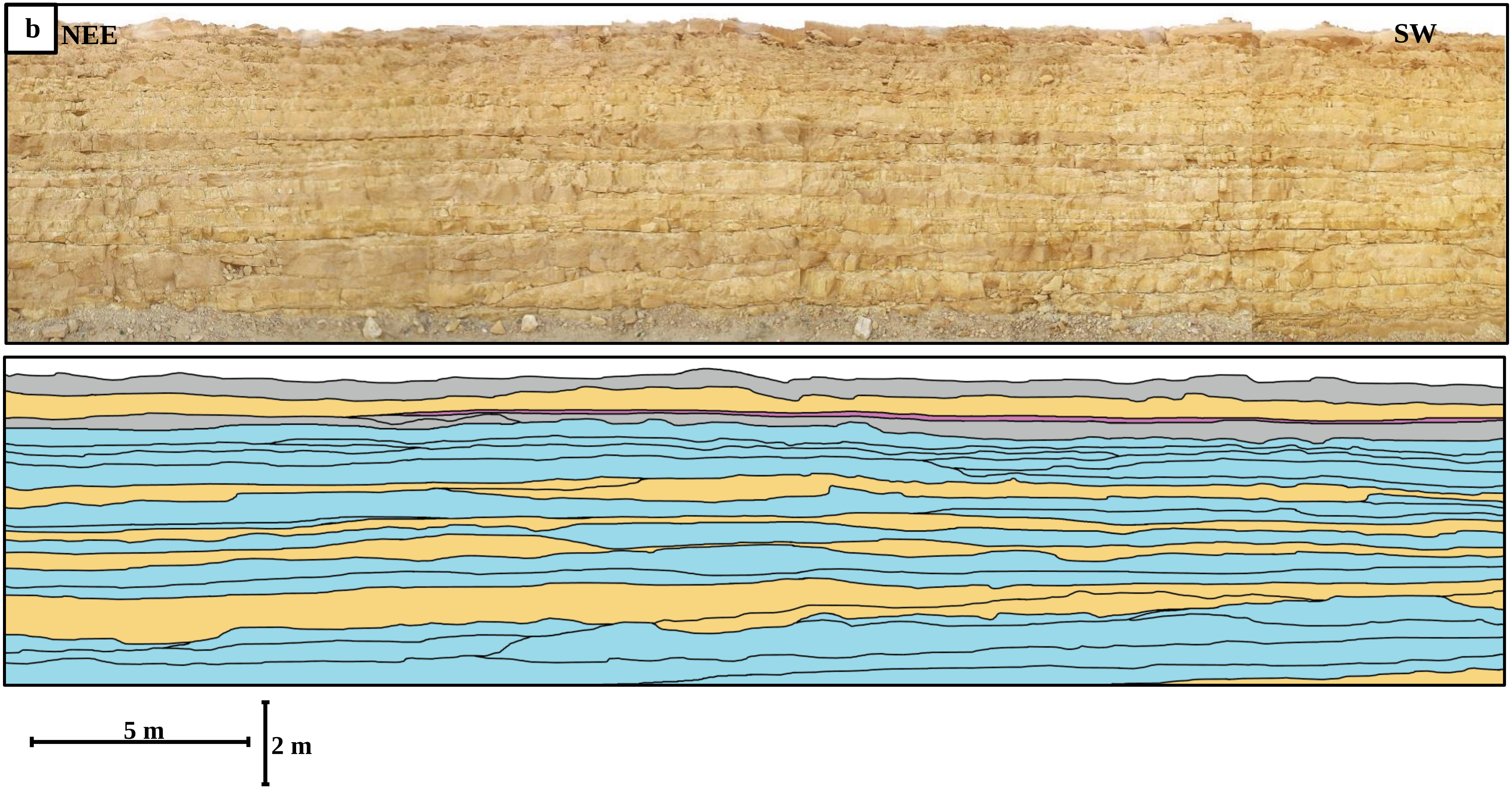

Figure 4.10: (Continued).

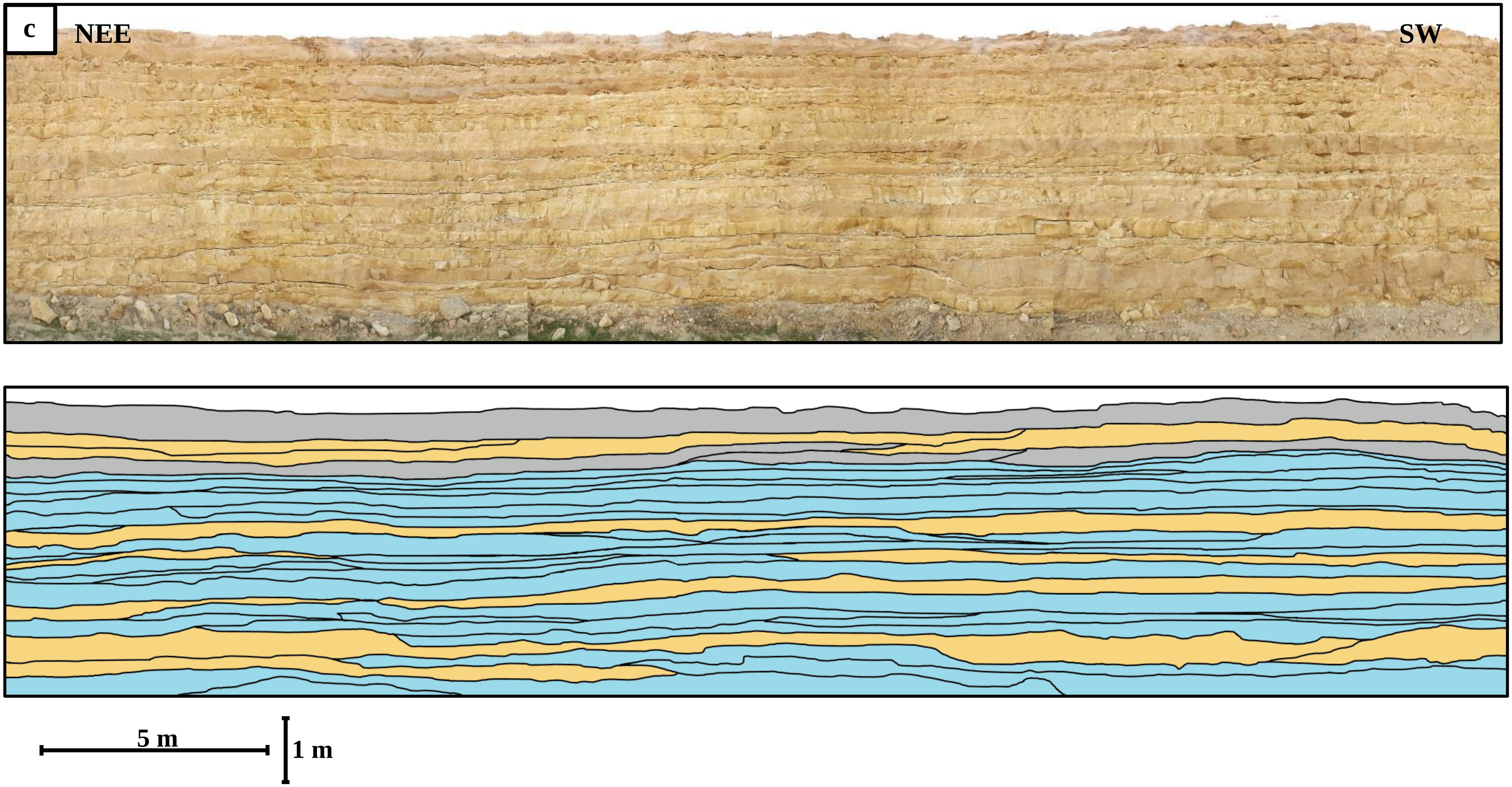

Figure 4.10: (Continued).

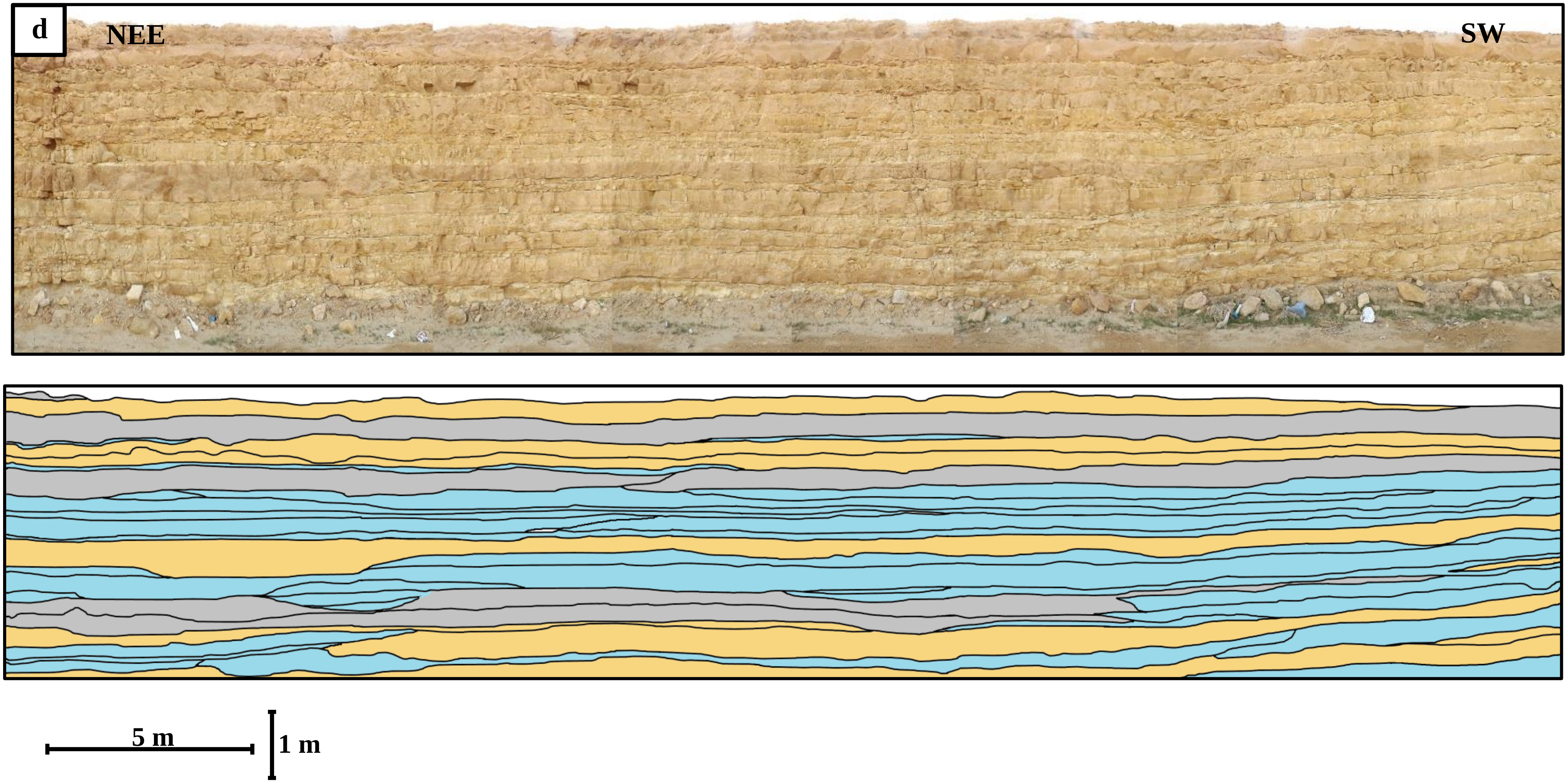

Figure 4.10: (Continued).

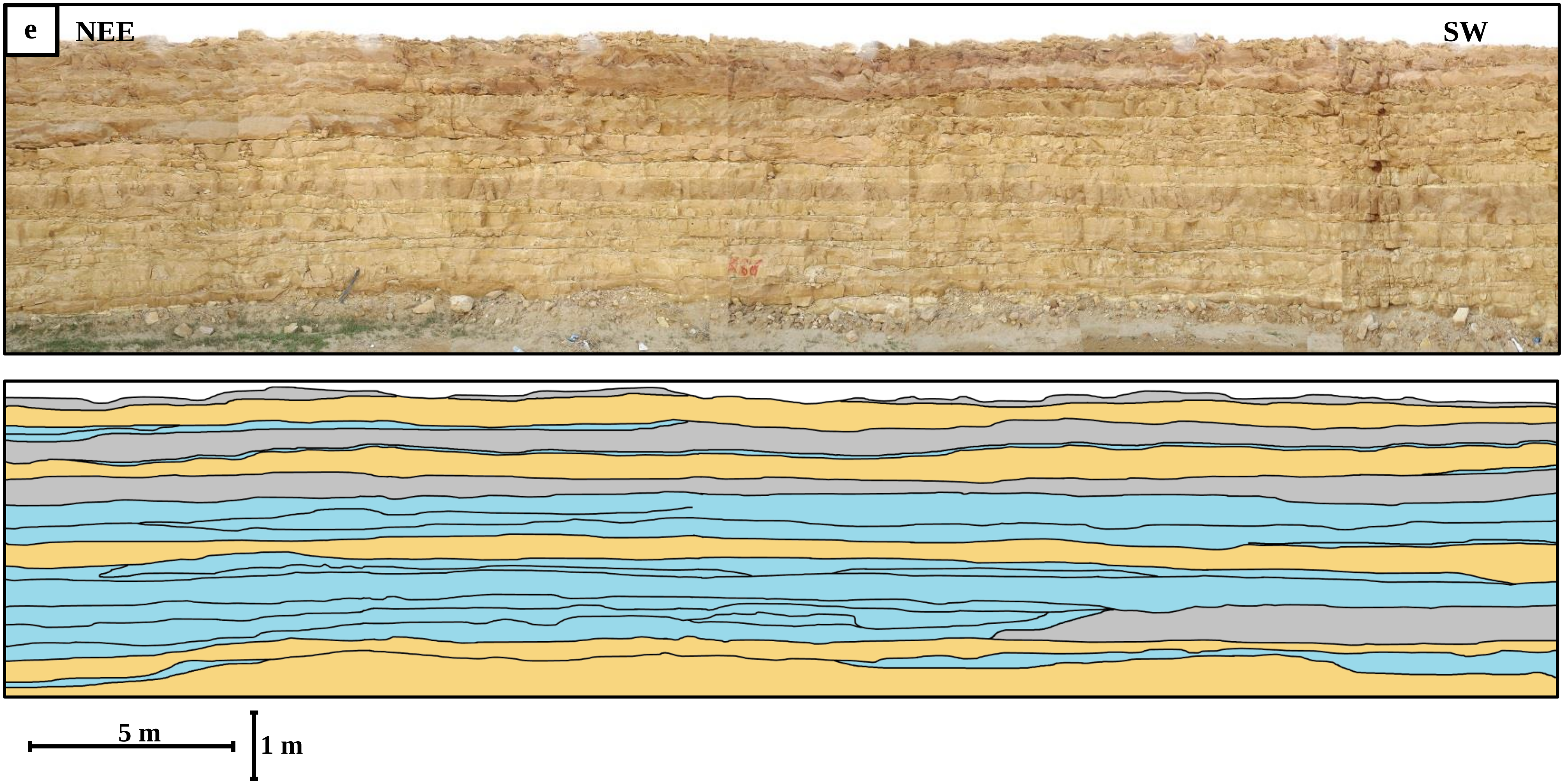

Figure 4.10: (Continued).

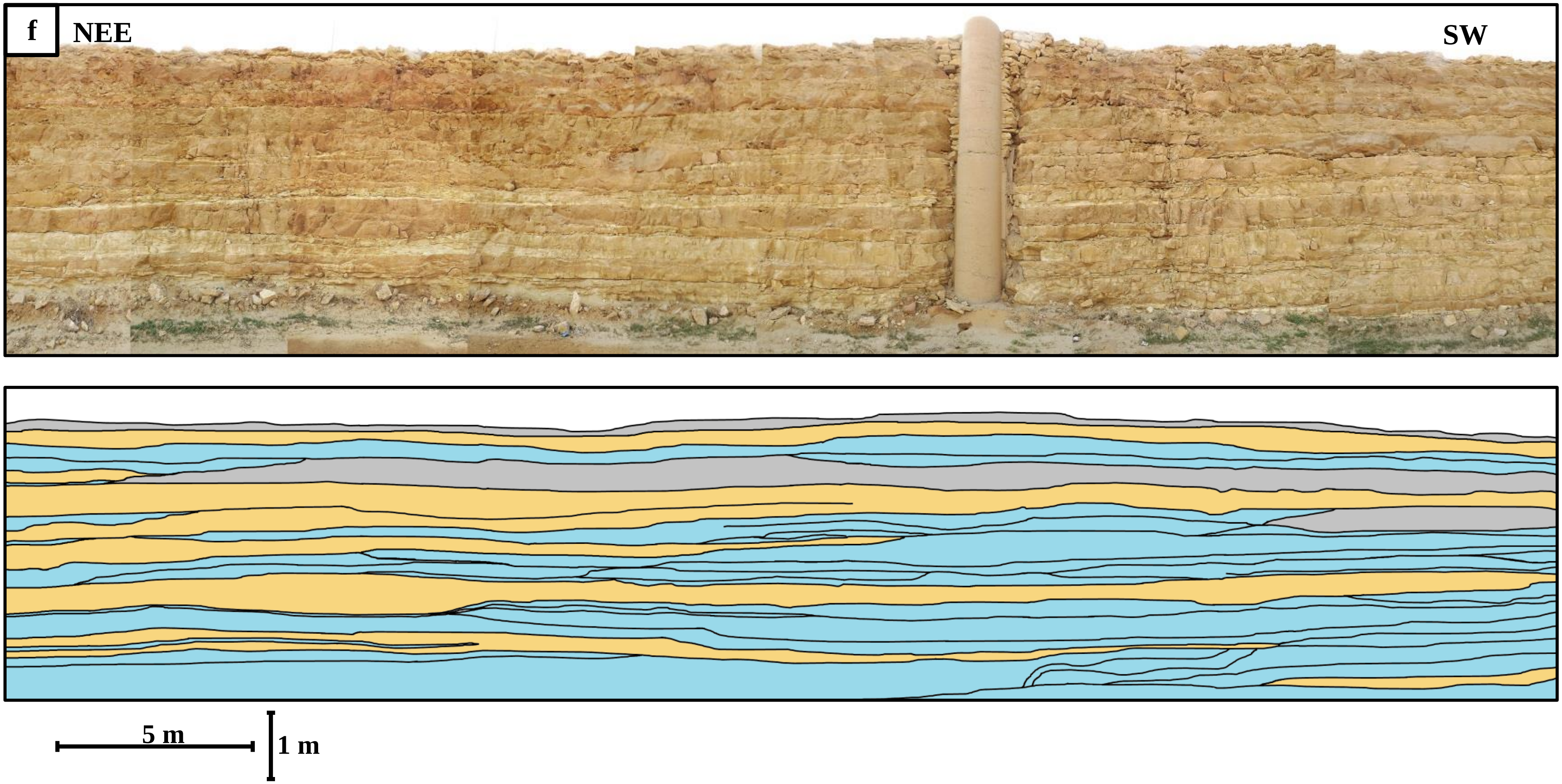

Figure 4.10: (Continued).

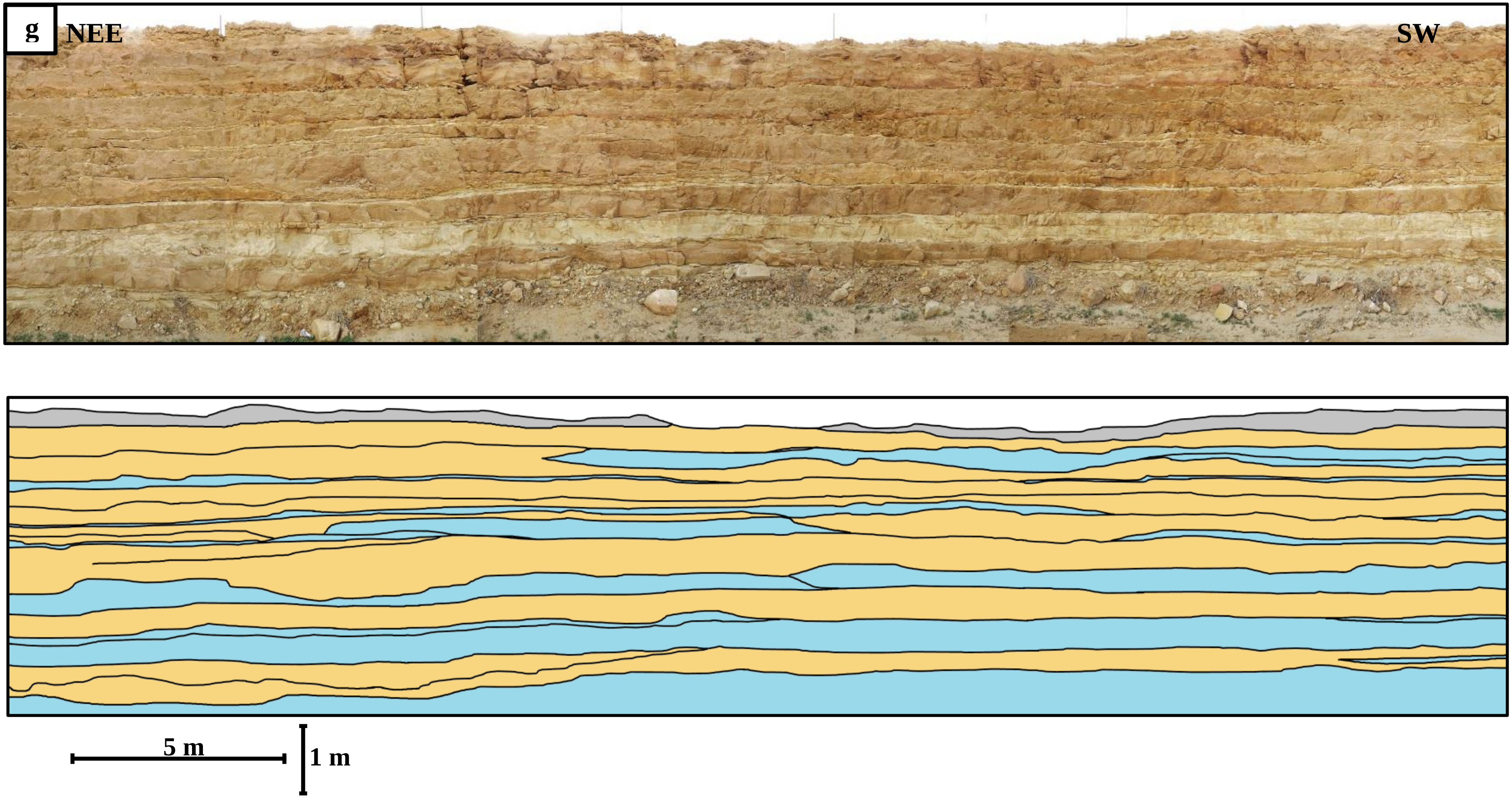

Figure 4.10: (Continued).

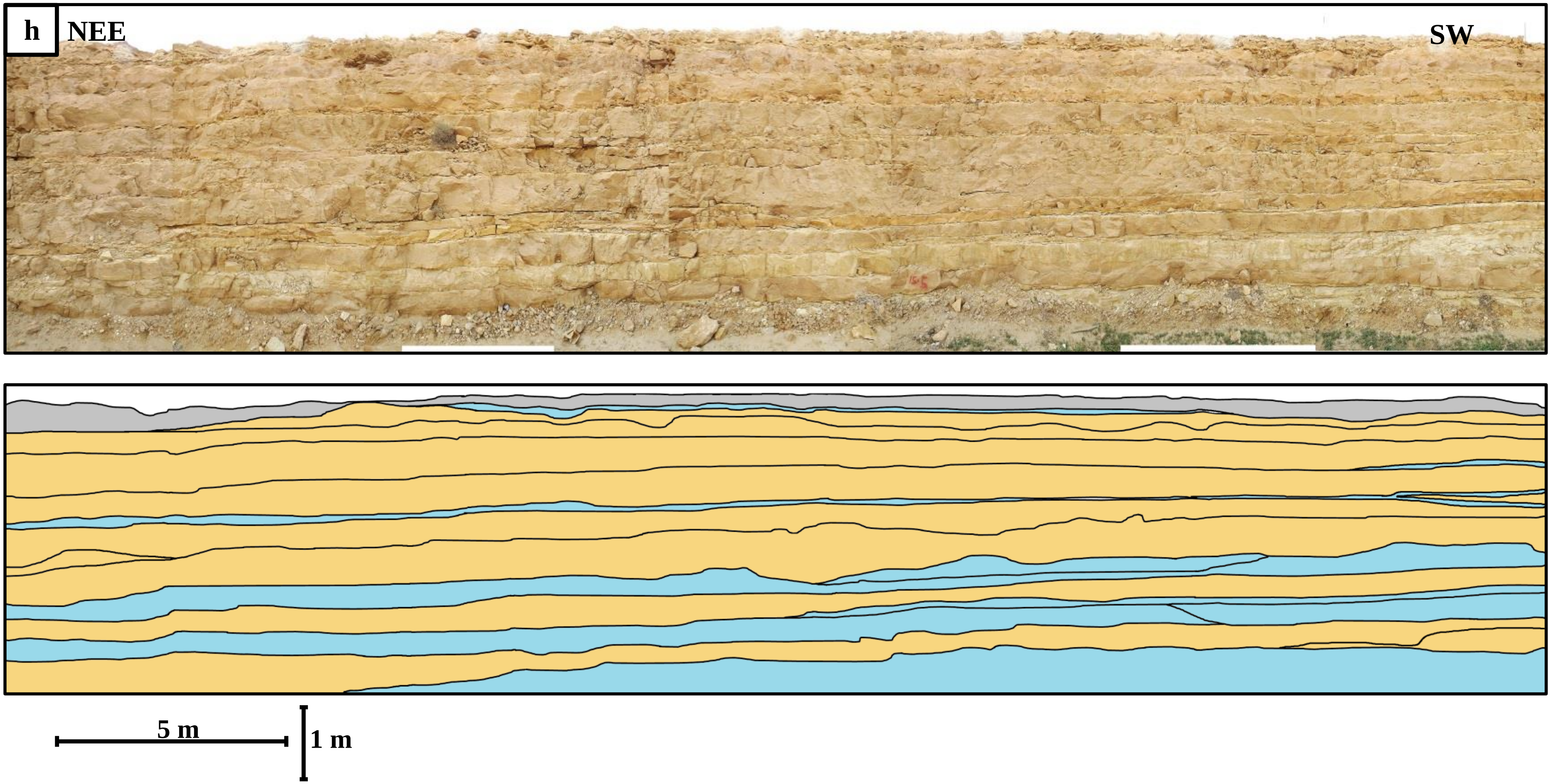

Figure 4.10: (Continued).

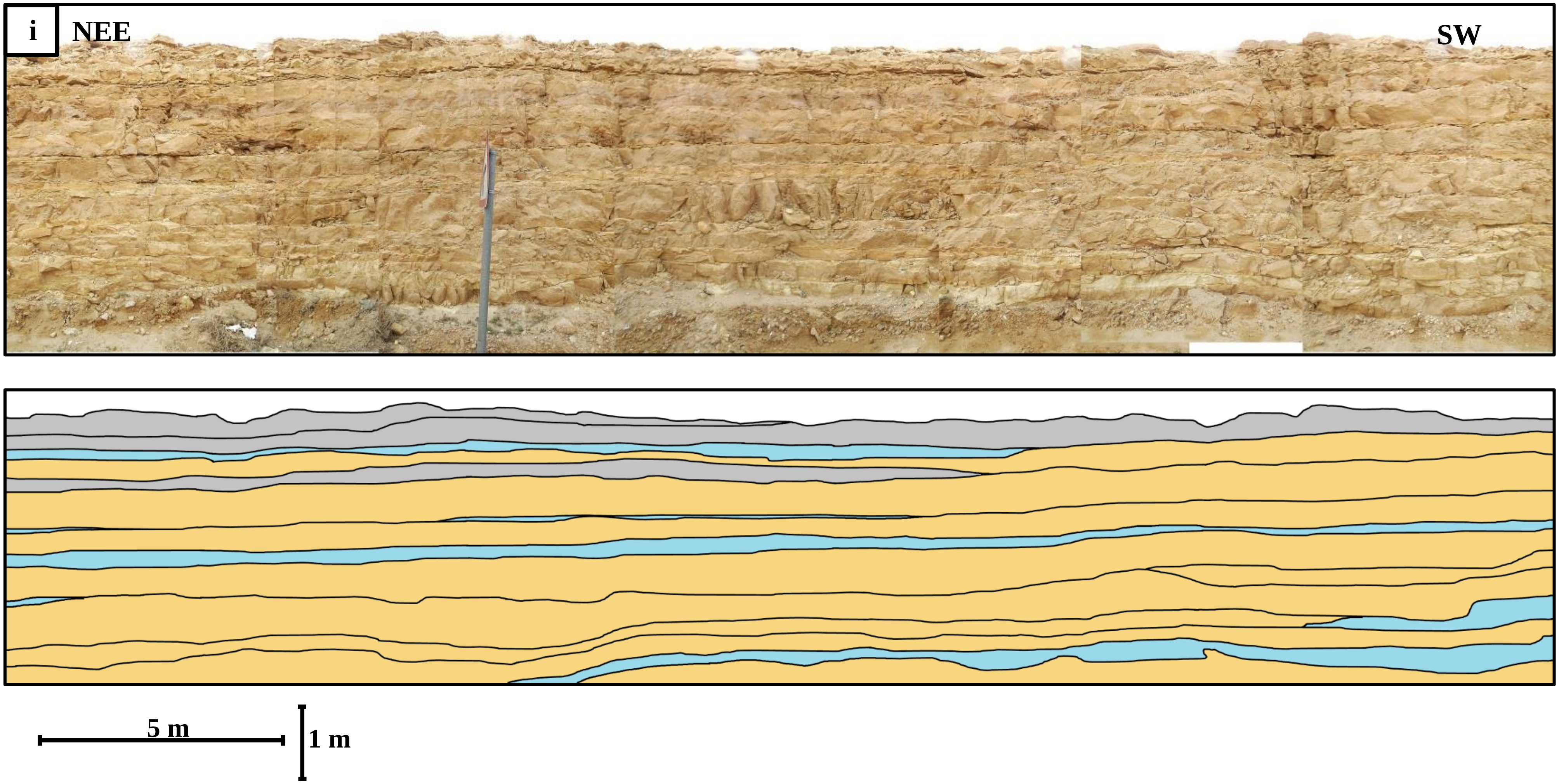

Figure 4.10: (Continued).

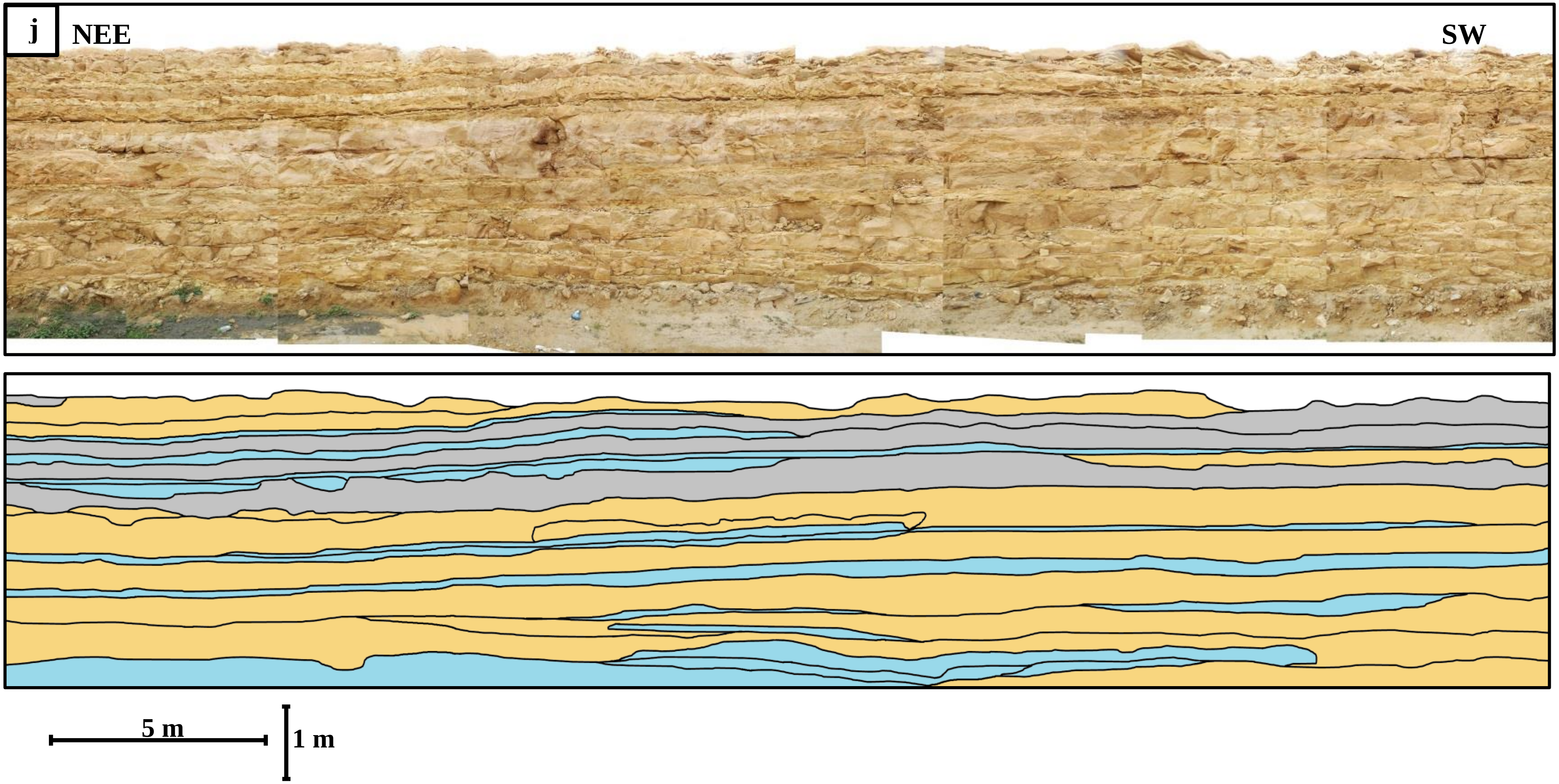

Figure 4.10: (Continued).

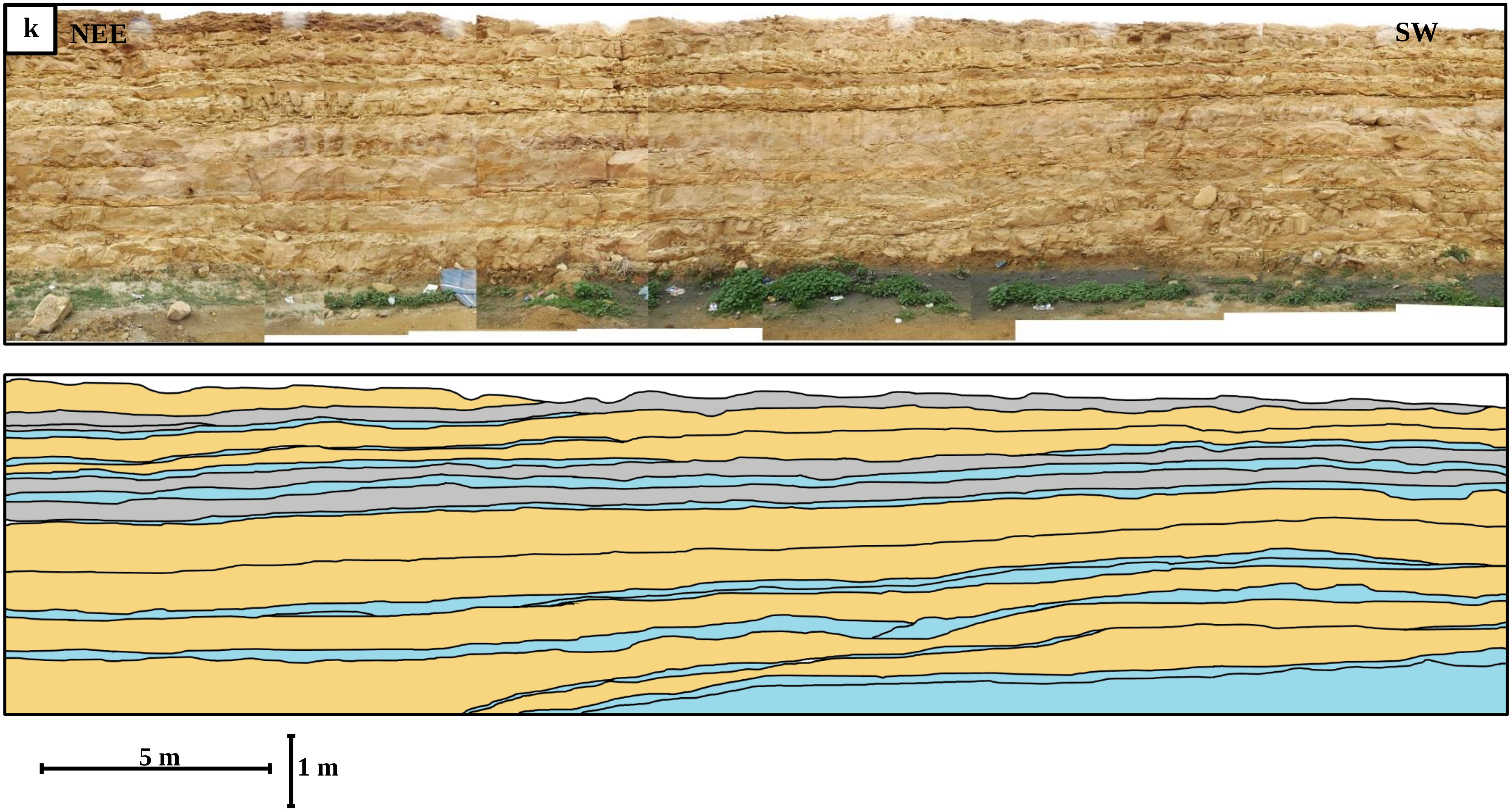

Figure 4.10: (Continued).

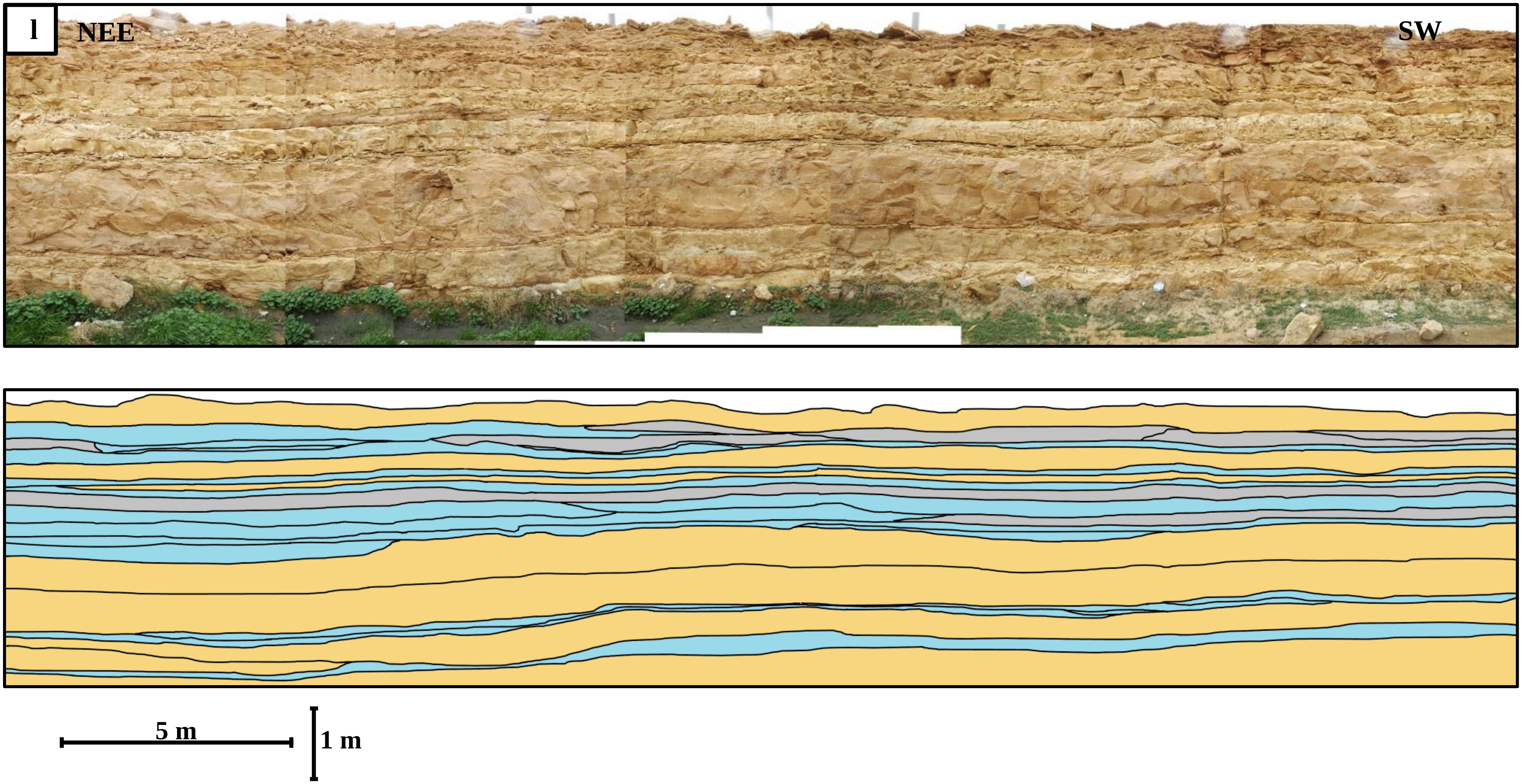

Figure 4.10: (Continued).

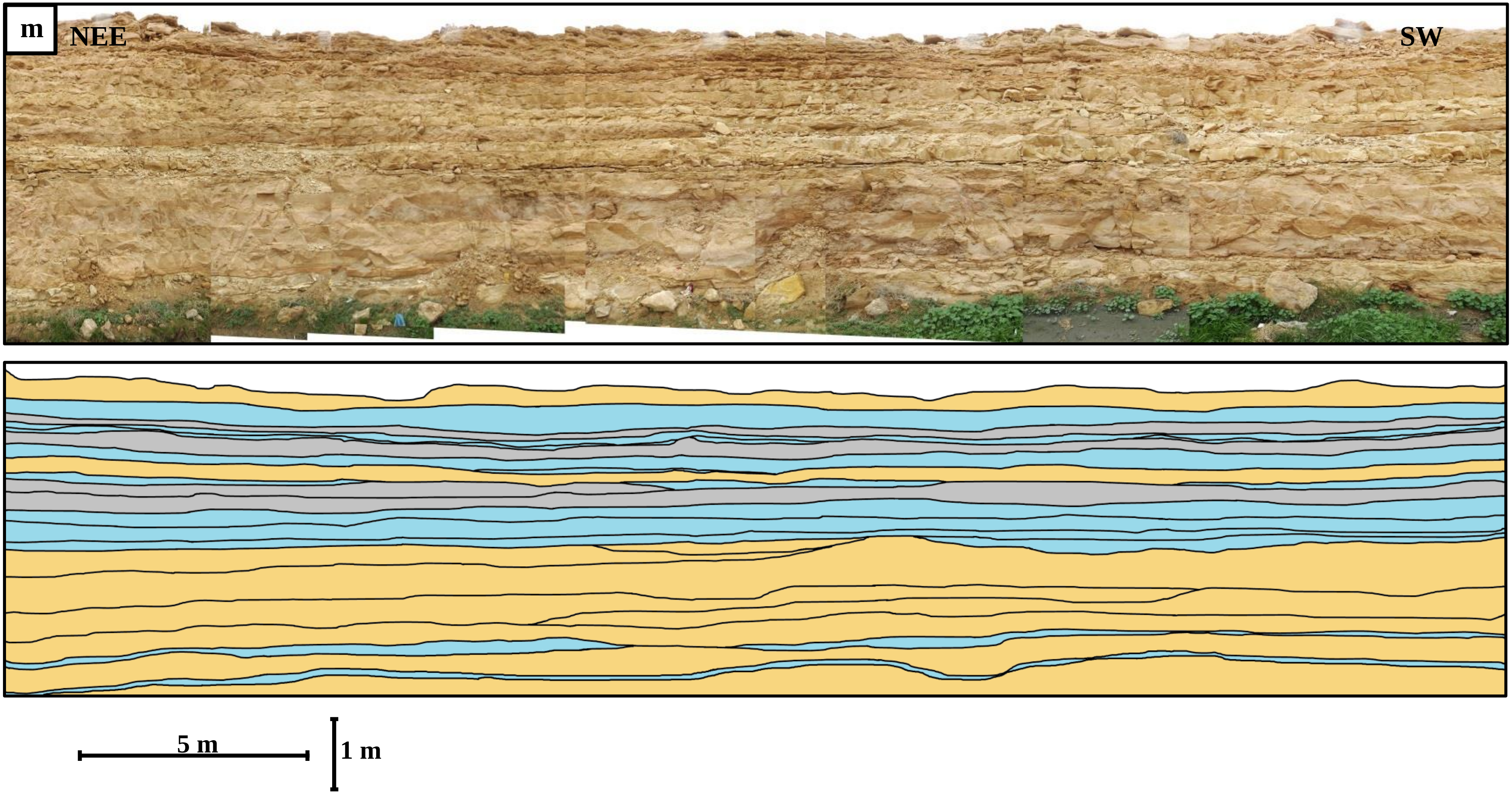

Figure 4.10: (Continued).

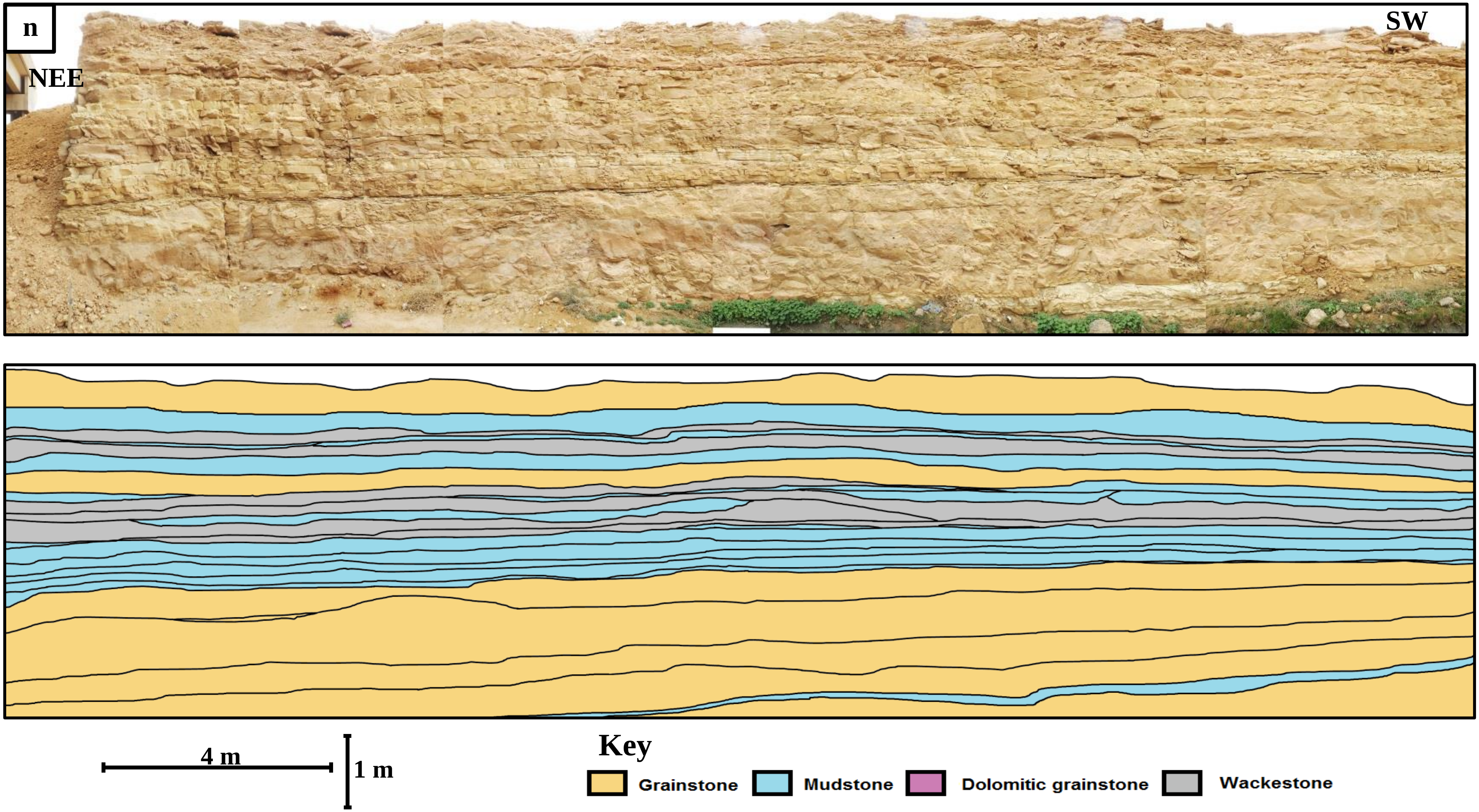

Figure 4.10: (Continued).

CHAPTER FIVE

POROSITY CHARACTERIZATION

5.1. Introduction

In order to maximize the oil and gas production, understanding the porosity types and their distribution is important in the reservoir characterization. Focusing on the thin section scale, the characters of different porosity types can play the roles in defining the reservoir quality. Pore size is one of the important parameters that can determine the quality of the pore type in reservoir intervals. A mixture of the best quality types of the pores within a reservoir unit can produce the optimum reservoir quality. Therefore, pore characters including: pore size and geometry can have a significant impact on understanding the reservoir quality. In this study, the pore types were linked with their geometrical shapes and sizes. If any variation is noticed in the pore geometry or in the size within the individual pore type, the pore type will be subdivided into two or more distinguished geometries. According to the variations in the pore geometries and sizes, eight pore types were identified in this study. Moldic porosity was divided into oomoldic and skelmoldic depending on the variation in the geometry. Vuggy porosity also subdivided into vuggy-1 and vuggy-2 based on the geometrical and size changes.

Quantitative analysis of the pore geometry required quantitative data of the aspect ratio and roundness factor for each pore type. Each pore type was identified separately to avoid mixing of different populations of porosity, and accordingly the parameters were separated. Microporosity was also calculated by subtracting the visually estimated porosity value from the total plug's porosity in each sample (Cantrell and Hagerty, 1999). Quantitative analysis of the aspect ratio and roundness factor for each pore type are essential to make the geometrical classification of porosity and to link the pore type with the pore geometry.

The analyzed thin section samples contain group populations of different pore sizes. In each sample there are many types of porosity forming a large population. On the basis of pore sizes, there are at least three different populations in each type of porosity. In the following samples, the populations were separated on the basis of the porosity types and further into different pore sizes. Separation of the porosity's populations is important because each population has different contributions to the visual estimated porosity. Porosity type A has different sizes, geometry and percent as compared to the porosity type B. For the same porosity type, large size pores are counted fewer times than smaller pores, with more contribution to the total porosity. Smaller pores are count more with less contribution in the total porosity.

5.2. Porosity Types Identified From Thin Sections

The Choquette and Pray (1970) porosity classification scheme was used to classify the porosity present the analyzed samples. On the basis of this classification scheme, six types of porosity were identified from the studied samples. The porosity types which include intergranular, intragranular, moldic, vuggy intercrystalline and intracrystalline types are briefly described as follow;

Intergranular porosity is defined as the pore space between skeletal or non-skeletal grains. In the Upper Khartam Member, this type of porosity constitutes the initial main pore type in oolitic and skeletal grainstone before it was destroyed by diagenetic cementation. This type of porosity provides minor effective porosity in the analyzed samples (Figure 5.6a). It occurs in a limited number of beds because of the extensive cementation that destroyed the primary porosities. Cementation also closed the pore throat and killed the effective porosity and the permeability as well.

Intragranular porosity is considered as secondary porosity formed as a result of partial dissolution of grains. It rarely occurs in the studied samples as in ooids and skeletal grains.

Moldic porosity is formed when the metastable grains are dissolved. The moldic pores take the shape, and size of the original grains. Molds are the dominant pore type in the analyzed samples. Some of the molds are complete molds, while other molds are filled partially or completely by calcite cement (Figures 5.1a and 5.1b). This type of pore shows unconnected molds in 2D thin section view. However, the connections appear in the SEM images show intensive microporosity between the cements and inside the molds itself (Figures 5.1f, 5.1g and 5.1h).

The vuggy porosity is characterized by large pores and it outlines do not follow any systematic boundaries. This porosity was likely formed as a result of combination of two or more pore types, or by extremely poor mold preservation. Diagenetic dissolution of grains, matrix or cements in the samples might have also allowed the formation of this porosity type. Vugs are the main porosity type in the wackestone/mudstone and grainstone facies in the studied outcrop sections of Upper Khartam Member (Figure 5.1).

Intercrystalline porosity is the porosity type that occurs dominantly between dolomite crystals. This porosity type was found mainly associated with analyzed dolomitized mudstone and grainstone samples. It may also be associated with micrite cement crystals at micro-scale (Figure 5.1f). This type of porosity accounts for approximately less than 1% of the total porosity in the studied samples (Figure 5.1). Intracrystalline porosity mainly occurs within the dolomite crystals. This type of porosity was likely formed either due to partial dissolution of dolomite crystals or as a result of de-dolomitization. This porosity was encountered in a number of the analyzed dolomitized samples. Fractures are very rare in the study area. However, a few minor fractures observed in some of the samples likely contribute to enhancing their porosity and permeability. Most of these fractures are partially/completely filled by calcite cement at thin section.

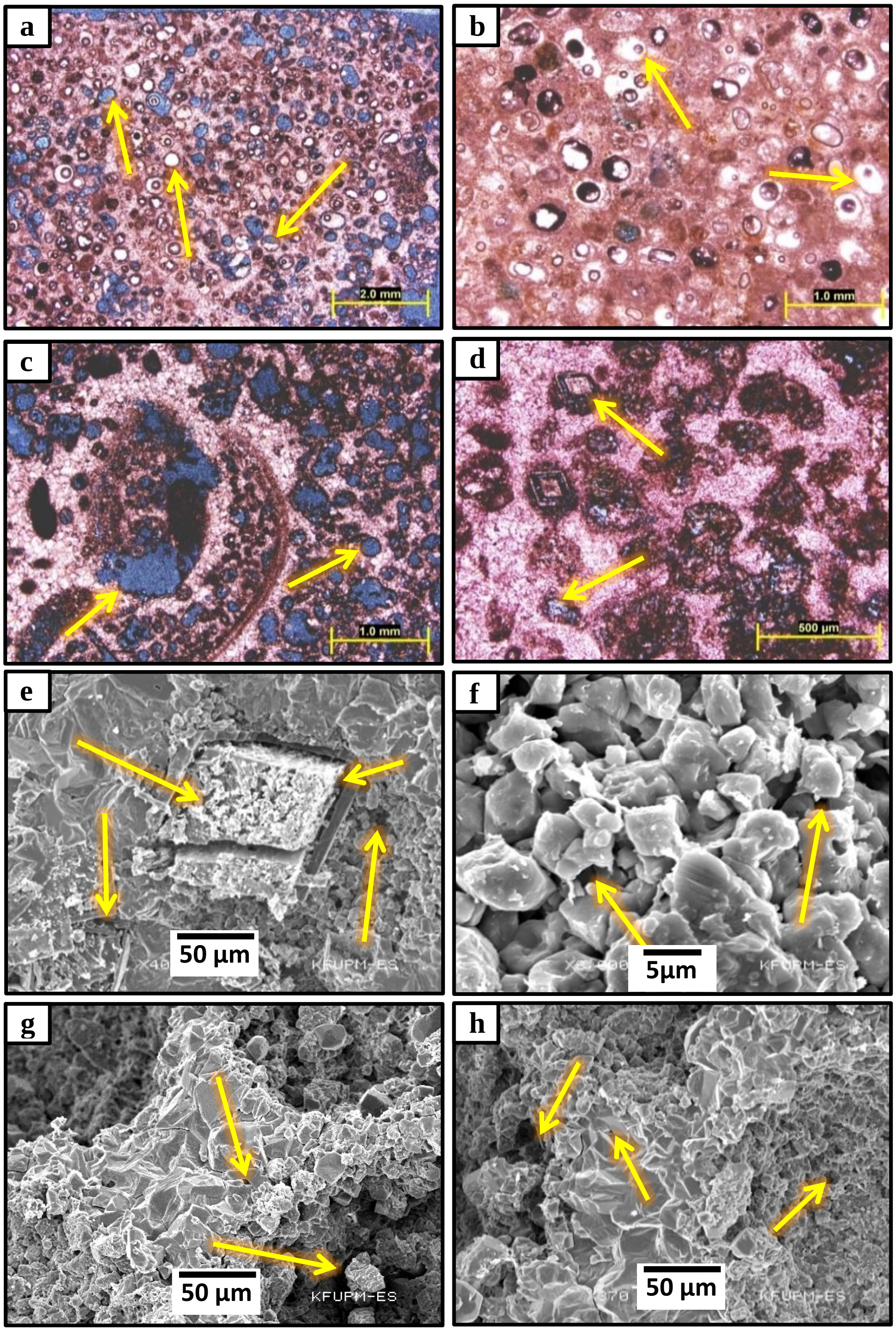

Figure 5.1: Different types of porosity in different scales of observation. (a) Moldic porosity show full molds but some molds are filled partially with cement, (b) complete filling of the moldic porosity with calcite cement, (c) vuggy porosity show variable shapes and sizes, (d) intercrystalline and intracrystalline porosities associated with dolomite crystals, (e) microporosity within the dolomite crystals, (f) microporosity between the sparry calcite crystals, (g) and (h) are showing the microporosity between the cement and inside the molds.

5.3. Porosity Characterization of the Upper Khartam Member

5.3.1. Facies Description

On the basis of sedimentological and thin section petrographic description, the studied samples were well-sorted oolitic grainstone facies, cross-bedded oolitic fossiliferous grainstone facies, graded mudstone to packstone facies, and dolostone facies.

5.3.1.1. Well-Sorted Oolitic Grainstone Facies

This facies is characterized by total dissolution of ooid grains, well rounded moldic porosity, and absence of the skeletal grains/molds. The pores from two representative samples belonging to this facies are described below. Both samples are characterized by dominantly moldic and minor amount of vuggy porosities. In general, the moldic and vuggy porosities show very close geometry and sizes. The total measured core porosity range from 25% to 35% and their permeability values ranges from 10 to 23 md.

The core plug measured porosity in the first sample is 25%. Using JMicroVision software to calculate the visual porosity, a 16% moldic porosity was obtained while vuggy porosity contributed about 4% to the pore volume. Therefore the microporosity in the sample accounts for ~5% of the total porosity (Figure 5.2c). The second sample is characterized by 35.5% measured core plug porosity. In thin section, moldic porosity contributes by 28%, while vuggy porosity contributes about 0.5%. Therefore ~7% represents the microporosity in the sample (Figure 5.3c).

Except for very few pores that are partially filled with calcite cement, the molds show full pore molds in both samples (Figures 5.2a and 5.3a). The few skeletal molds encountered in both samples had little or no contributions to porosity value. Some molds show strong sharp porosity color contrast indicating preservation by micrite envelopes while a few other show weak boundaries indicating poor preservation of molds that converted to vuggy porosity.

In both samples, moldic porosity appears as a well-rounded circular shape, with aspect ratio very close to 1.5 in average (equidimensional) and an average of 2 roundness factor indicating rounded shape. The dominant pore sizes of the oolitic molds in the first and second sample are 350 μm^2 and 16 mm^2 respectively (Figures 5.2d and 5.3d).

Both samples showed equidimensional pores in all pore size windows (Figures 5.2e, 5.2g, 5.2i, 5.3e, 5.3g and 5.3i). Roundness factor indicates rounded shape in size less than 1 mm^2 and 3.3 mm^2 respectively for the first sample and the second sample (Figures 5.2f, 5.2h, 5.3f and 5.3h). However, the pores begin to be a little angular in sizes larger than 1 mm^2 and 3.3 mm^2, respectively for the first sample and the second sample (Figures 5.2j and 5.3j). Combination of the aspect ratio and roundness factor shows circular pores with marginal large square pores.

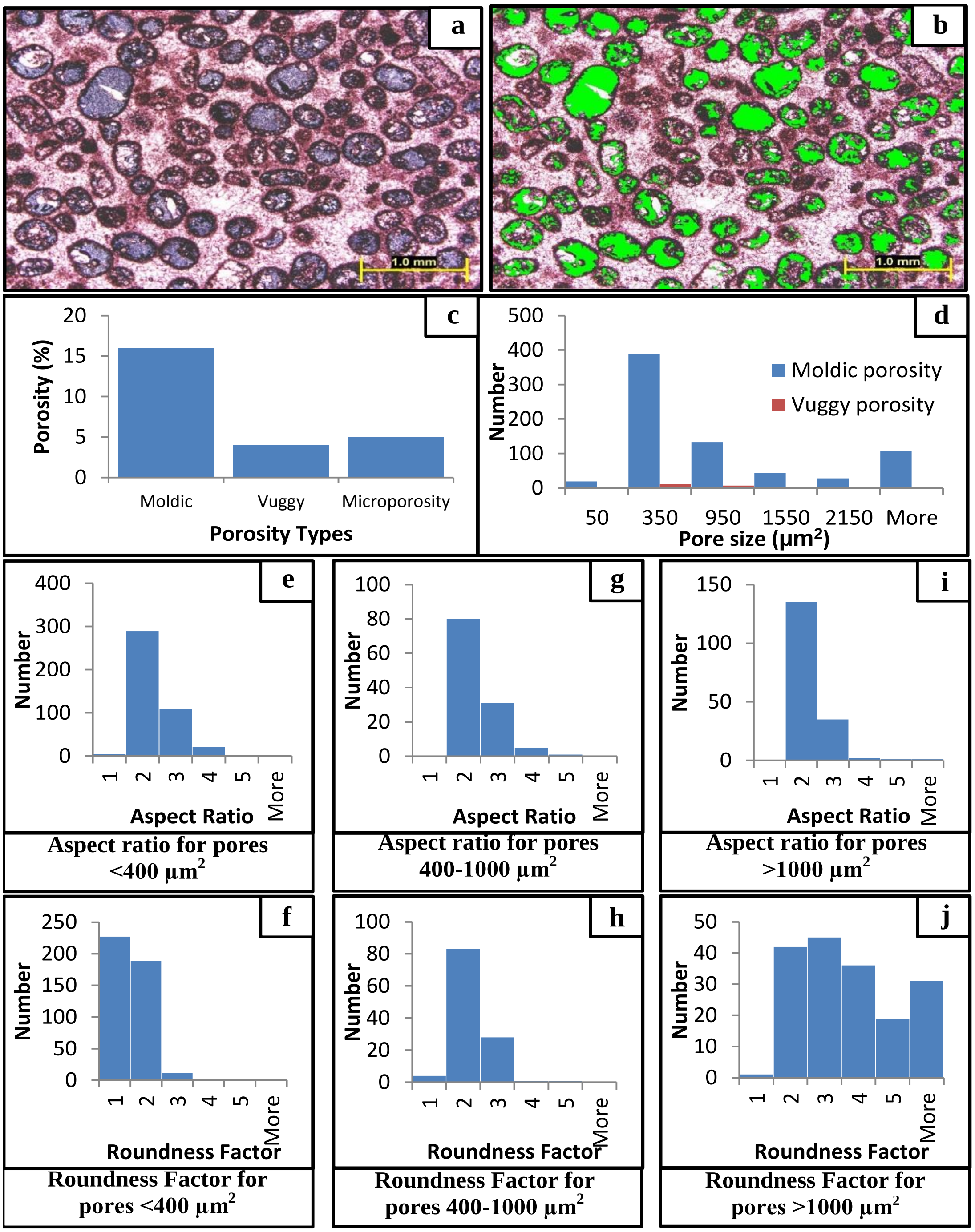

Aspect ratio for pores <400 µm^2

Aspect ratio for pores 400-1000 µm^2

Aspect ratio for pores >1000 µm^2

Roundness Factor for pores <400 µm^2

Roundness Factor for pores 400-1000 µm^2

Roundness Factor for pores >1000 µm^2

Figure 5.2: (a) representative microphotograph of the first thin section sample of the well-sorted oolitic grainstone facies; (b) picked porosities in green using JMicroVision software; (c) The percentages of visual estimation of different pore types and calculated microporosity; (d) The frequency distribution of moldic and vuggy porosity with different pore sizes; (e) & (f) The aspect ratio and roundness factor frequency distribution of pore sizes less than 400 μm^2 window respectively; (g) & (h)The aspect ratio and roundness factor frequency distribution of pore sizes between 400-1000 μm^2 window respectively; and (i) & (j) The aspect ratio and roundness factor frequency distribution of pore sizes larger than 1000 μm^2 window respectively.

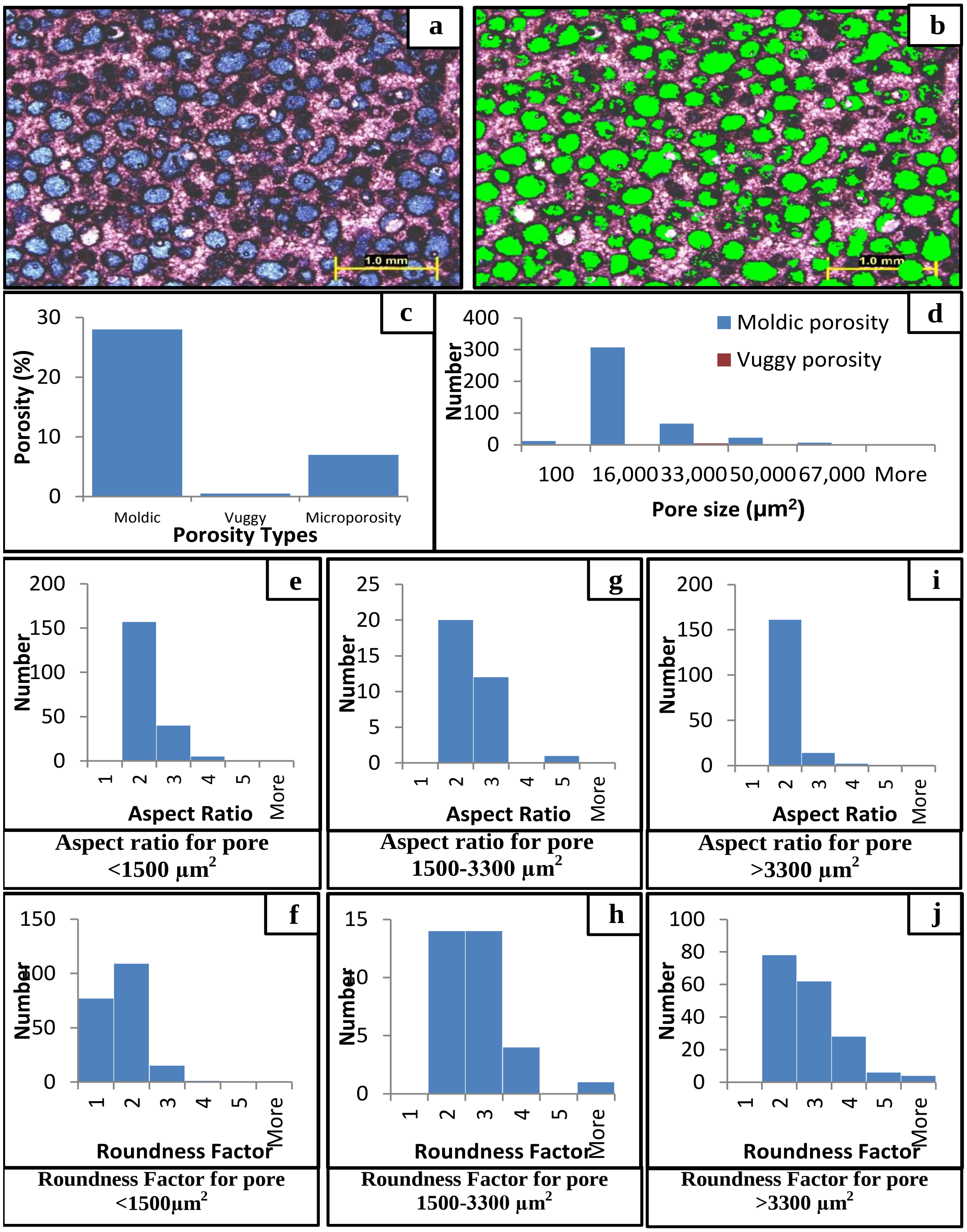

Figure 5.3: (a) representative microphotograph of the second thin section sample of the well-sorted oolitic grainstone facies; (b) picked porosities in green using JMicroVision software; (c) The percentages of visual estimation of different type of porosity and calculated microporosity; (d) The frequency distribution of moldic and vuggy porosity with different pore sizes; (e) & (f) The aspect ratio and roundness factor frequency distribution of pore sizes less than 1500 µm^2 window respectively; (g) & (h) The aspect ratio and roundness factor frequency distribution of pore sizes between 1500-33000 µm^2 window respectively; and (i) & (j) The aspect ratio and roundness factor frequency distribution of pore sizes larger than 33000 µm^2 window respectively.

5.3.1.2. Cross-bedded Oolitic Fossiliferous Grainstone Facies

In this facies, ooids and skeletal grains are mostly dissolved with minor remains of original grains. The facies is characterized by well-rounded oolitic molds and angular bivalve molds. Few samples have intergranular porosity.

Three representative samples belonging to this facies are discussed in the following section. The main porosity types in the samples are moldic with minor amount of intergranular and vuggy porosity types. Most of the molds are partially filled with calcite cement. The total core porosity ranges from 25% to 35% and permeability ranges from 10 to 23 md.

This facies is represented by three different samples to cover the variety ranges of porosity types include: moldic, vuggy, intergranular and intragranular porosities. The first sample is contains moldic and vuggy porosities dominated by moldic porosity (Figure 5.4a). The second sample is also contains moldic and vuggy porosities but instead it dominated by moldic porosity (Figure 5.5a). The third sample is composite of intergranular and intragranular porosities dominated by intergranular pores (Figure 5.6a).

In the first sample, the total measured porosity from core plug was 21%. Visual estimation using the JMicroVision software yielded 14% of moldic porosity and 4% of vuggy porosity suggesting that the microporosity amount to about ~3% of the total porosity (Figure 5.4c). In the second sample, the total porosity measured from core plug was 21%. In thin section, the vuggy porosity contributes by 12% and moldic porosity represents 5%. This suggests that the microporosity is ~4% of the total measured porosity (Figure 5.5c). In the third sample, the total measured porosity from core plug is

21%. In thin section, intergranular porosity contributes about 12%, and intragranular porosity amounts to about 5%. The microporosity calculated from this sample is ~4% (Figure 5.6c). Calcite cement around the grains reduced the connectivity of the intergranular pores.

The dissolution of ooid grains resulted into the formation of the moldic pores. In some of the molds, the pores are subdivided into many small pores separated by calcite cement (Figure 5.4a).

The moldic porosity aspect ratio shows that the pores are elongated without any significant changes as pore size becomes larger (Figures 5.4e, 5.4g, 5.4i, 5.5e, 5.5g and 5.5i). Roundness factor shows rounded shape for the molds smaller than 300 μm^2while those with sizes greater than 300 μm^2 show considerable amount of angularity in the first sample (Figures 5.4f, 5.4h and 5.4j) but in the second sample the angularity appears in sizes larger than 9 mm^2 (Figures 5.5f, 5.5h and 5.5j). The combination of the aspect ratio and roundness factor shows small elongated well rounded elliptical molds. The larger molds are elongated rounded to sub-angular ellipses and sub-rectangular molds.

Vuggy porosity in this facies is not uniform in shape, but overall, the pores are elongated with rounded edges. The average aspect ratio is mainly above 2 indicating elongated shapes. Roundness factor of 2 to 3 indicates rounded shape, and the average sizes of the vugs are 3 mm^2 for small vugs, and 12 mm^2 for large vugs (Figure 5.5d).

Vuggy porosity's aspect ratio shows elongated pores in all size windows (Figures 5.4e, 5.4g, 5.4i, 5.5e, 5.5g and 5.5i). Roundness factor indicates rounded shape in the vugs smaller than 300 μm^2 and those vugs with size greater than 300 μm^2 show some degrees of angularity (Figures 5.4l, 5.4n and 5.4p), but in the second sample the angular pores become significant in sizes larger than 9 mm^2 (Figures 5.5f, 5.5h and 5.5j). The combination of the aspect ratio and roundness factor shows that the small pores are of elongated well rounded elliptical vugs, and large vugs are elongated rounded sub-angular to angular ellipse and sub-rectangular shapes.

Intergranular porosity in this facies shows variable shapes, but mainly elongated with angular edges. The average aspect ratio of the sample which is >1.5 (elongated) and average roundness factor (>3) indicate an angular shape. The average sizes of intergranular pores are 7 mm^2, and 70 mm^2 for the large pores (Figure 5.6d).

The pore shape of intergranular porosity is elongated, rounded to extremely angular. The aspect ratio shows elongated pores for all pore size windows (Figures 5.6e, 5.6g and 5.6i). Roundness factor for smaller pores (less than 4 mm^2) shows rounded to sub-angular shape. On the other pores larger than 4 mm^2 exhibit high degree of angularity (Figures 5.6f, 5.6h and 5.6j). A combination of the aspect ratio and roundness factor indicate that the small pores are small elongated, rounded to elliptical while the large ones are elongated, angular to rectangular.

For the intragranular porosity, the pores appear to be elongated to well-rounded. The aspect ratio shows that the pores are equidimensional but when the pore size exceeds 4 mm^2, the pores become elongated (Figures 5.6k, 5.6m and 5.6o). Roundness factor shows very well-rounded pores (Figures 5.6l, 5.6n and 5.6p) in all sizes. The small intragranular pores are very well-rounded, equidimensional and circular in shape and the large pores are very well-rounded, elongated and elliptical in shape.

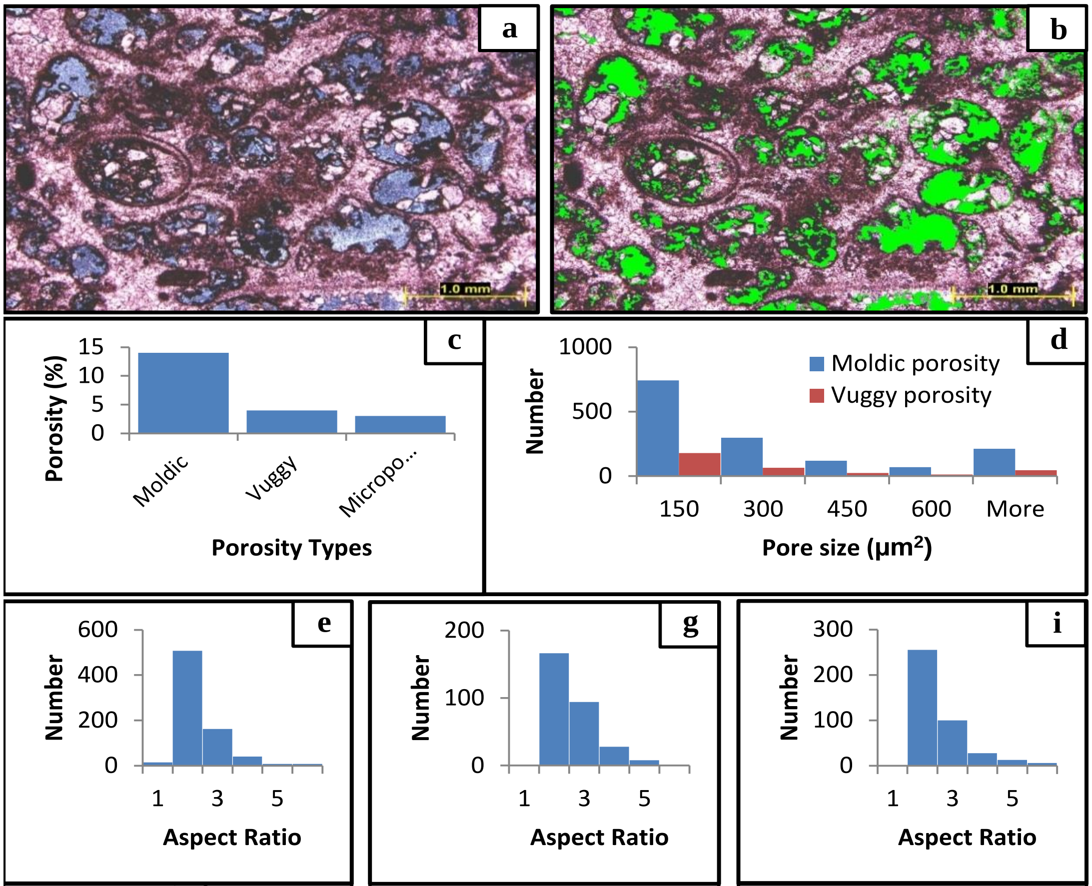

Aspect ratio for pores <150 μm^2

Aspect ratio for pores 150-300 μm^2

Aspect ratio for pores > 300 μm^2

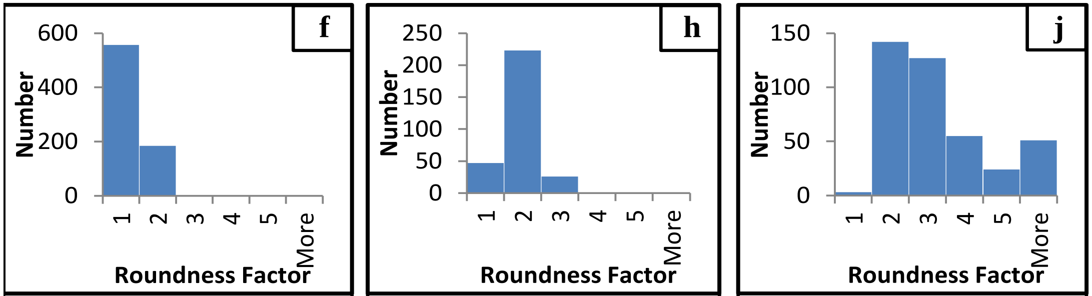

Roundness factor for pores <150 μm^2

Roundness factor for pores 150-300 μm^2

Roundness factor for pores > 300 μm^2

Figure 5.4: (a) representative microphotograph first thin section sample of the cross-bedded oolitic fossiliferous grainstone facies; (b) picked porosities in green using JMicroVision software; (c) The percentages of visually estimated porosity and calculated microporosity; (d) The frequency distribution of moldic and vuggy porosity in different pore sizes; (e) & (f) The aspect ratio and roundness factor frequency distribution of pore sizes less than 150 µm^2 window respectively for moldic porosity, and (k) & (l) for vuggy porosity respectively; (g) & (h) The aspect ratio and roundness factor frequency distribution of pore sizes between 150-300 µm^2 window respectively for moldic porosity, and (m) & (n) for vuggy porosity respectively; and (i) & (j) The aspect ratio and roundness factor frequency distribution of pore sizes larger than 300 µm^2 window respectively for moldic porosity, and (o) & (p) for vuggy porosity, respectively.

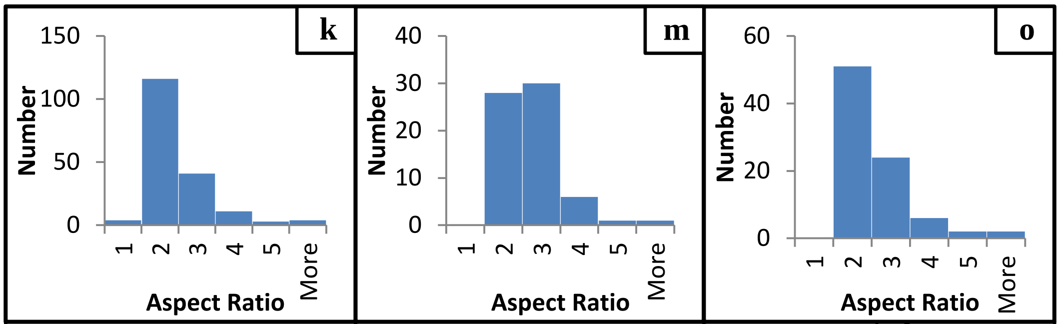

Aspect ratio for pores <150 µm^2

Aspect ratio for pores 150-300 µm^2

Aspect ratio for pores >300 µm^2

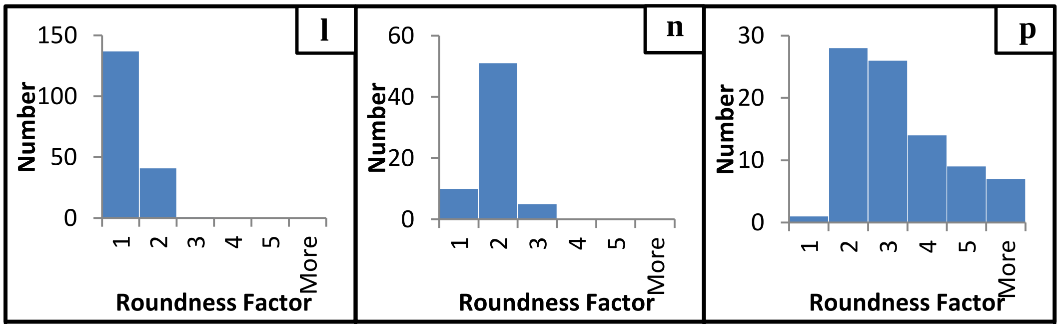

Roundness factor for pores <150 µm^2

Roundness factor for pores 150-300 µm^2

Roundness factor for pores >300 µm^2

Figure 5.4: (Continued).

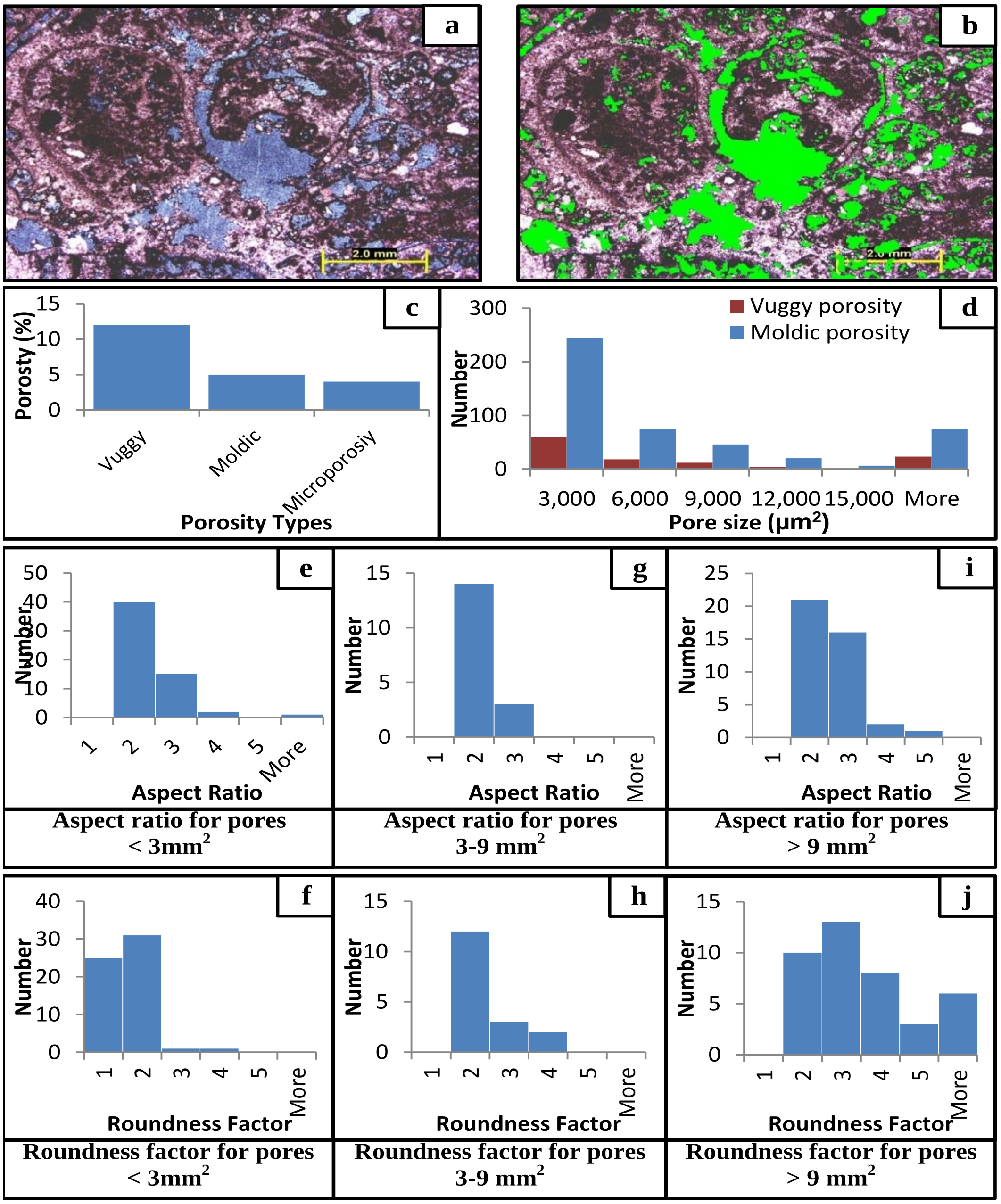

Aspect ratio for pores $< 3mm^2$ | Aspect ratio for pores 3-9 mm^2 | Aspect ratio for pores $> 9\ mm^2$

Roundness factor for pores $< 3mm^2$ | Roundness factor for pores 3-9 mm^2 | Roundness factor for pores $> 9\ mm^2$

Figure 5.5: (a) representative microphotograph of the second thin section sample of the cross-bedded oolitic fossiliferous grainstone facies; (b) picked porosities in green using JMicroVision software; (c) The percentages of visually estimated porosity and calculated microporosity; (d) The frequency distribution of vuggy and moldic porosity in different pore sizes; (e) & (f) The aspect ratio and roundness factor frequency distribution of pore sizes less than 3000 μm^2 window respectively for vuggy porosity, and (k) and (l) are for moldic porosity respectively; (g) & h) The aspect ratio and roundness factor frequency distribution of pore sizes between 3000-9000 μm^2 window respectively for vuggy porosity, and (m) and (n) are for moldic porosity respectively; and(i) & (j) The aspect ratio and roundness factor frequency distribution of pore sizes larger than 9000 μm^2 window respectively for vuggy porosity, and (o) and (p) are for moldic porosity, respectively.

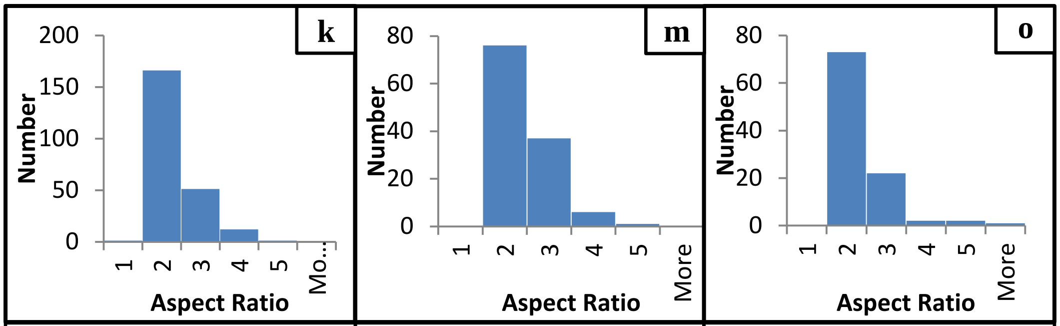

Aspect ratio for pores < 3mm^2

Aspect ratio for pores 3-9 mm^2

Aspect ratio for pores > 9 mm^2

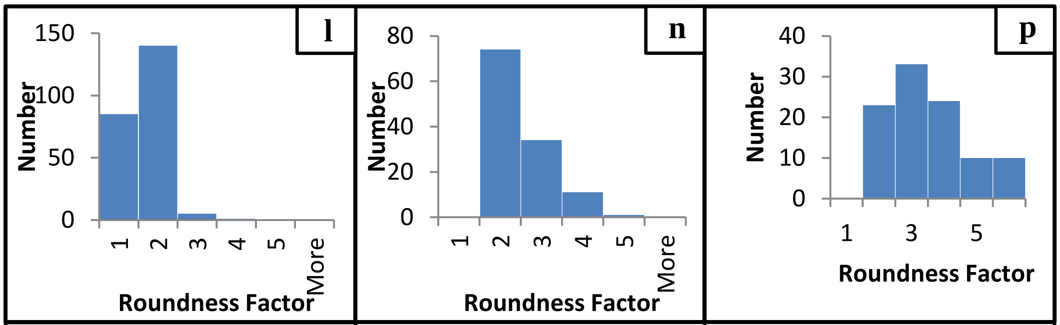

Roundness factor for pores < 3mm^2

Roundness factor for pores 3-9mm^2

Roundness factor for pores > 9mm^2

Figure 5.5: (Continued).

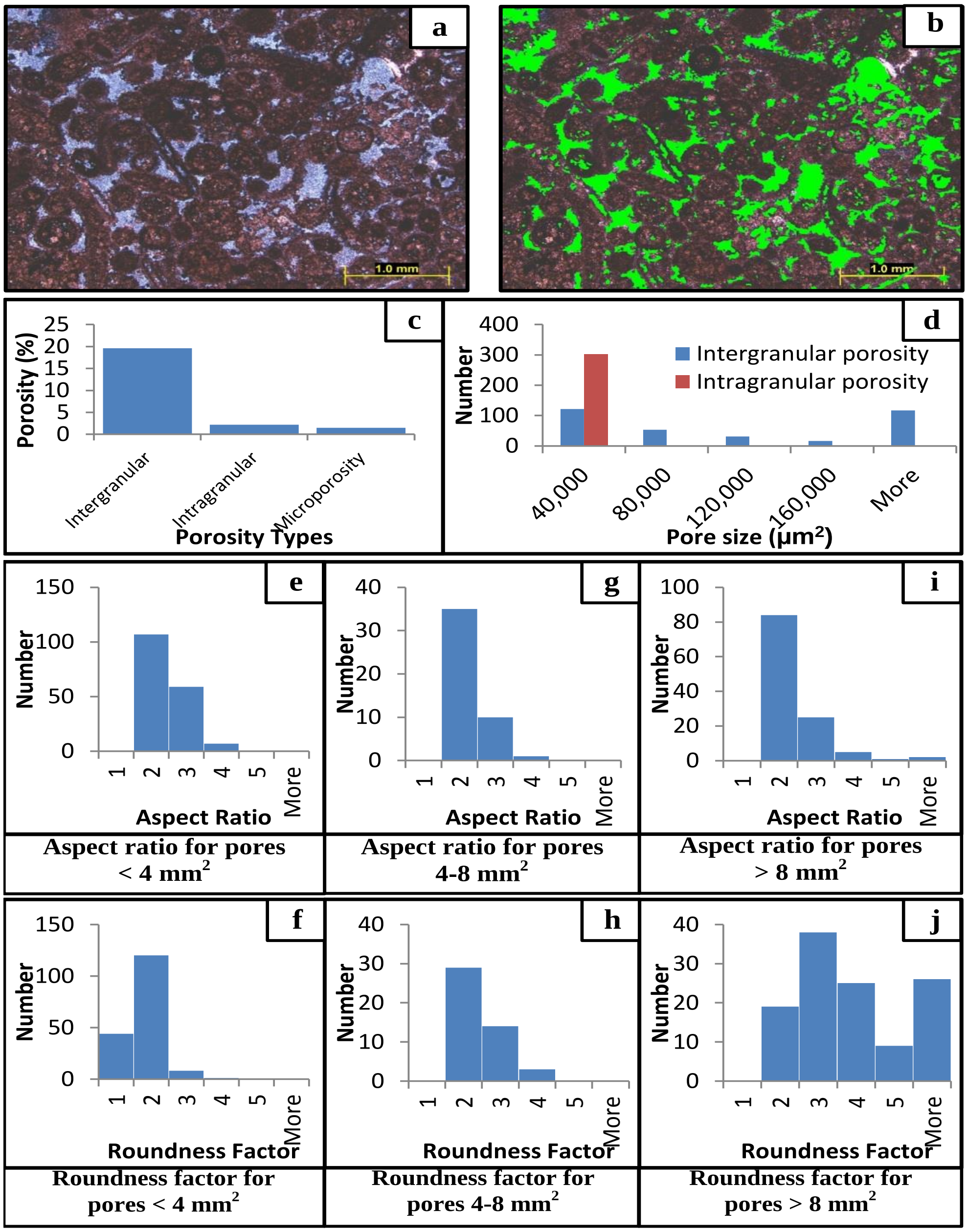

Figure 5.6: (a) representative microphotograph third sample of cross-bedded oolitic fossiliferous grainstone thin section sample; (b) picked porosities in green using JMicroVision software; (c) The percentages of visual estimated of porosity and calculated microporosity; (d) The frequency distribution of intergranular and intragranular porosity in different pore sizes; (e) & (f) The aspect ratio and roundness factor frequency distribution of pore sizes less than 4000 μm^2 window respectively for intergranular porosity, and (k) & (l) are for intragranular porosity respectively; (g) & (h) The aspect ratio and roundness factor frequency distribution of pore sizes between 4000-8000 μm^2 window respectively for intergranular porosity, and (m) & (n) are for intragranular porosity respectively; (i) & (j) The aspect ratio and roundness factor frequency distribution of pore sizes larger than 8000 μm^2 window respectively for intergranular porosity, and (o) & (p) are for intragranular porosity respectively.

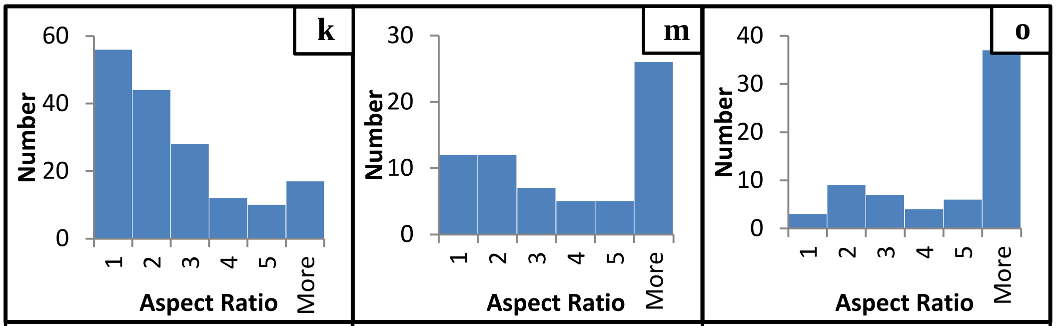

Aspect ratio for pores < 4 mm^2

Aspect ratio for pores 4-8 mm^2

Aspect ratio for pores > 8 mm^2

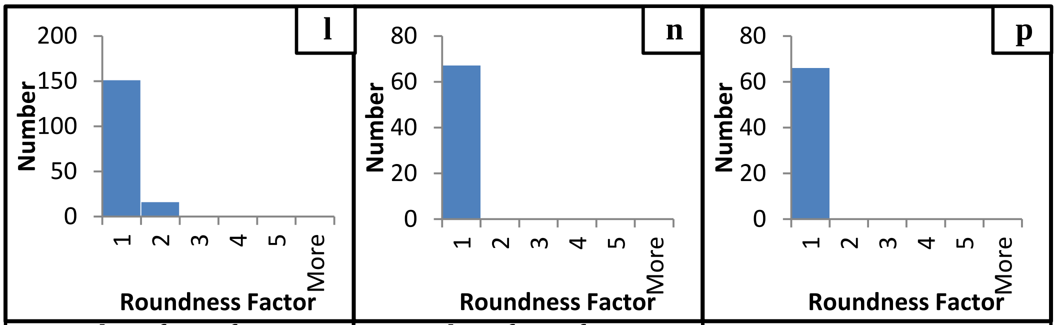

Roundness factor for pores < 4 mm^2

Roundness factor for pores 4-8 mm^2

Roundness factor for pores > 8 mm^2

Figure 5.6: (Continued).

5.3.1.3. Graded Mudstone to Packstone Facies

This facies contains muds with some scattered grains. The samples of this facies are characterized by vuggy porosity. The total core porosity ranges from 5 % to 10% and the permeability ranges from 0.3 to 1 md in two representative samples of this facies. The core plug measured porosity from the first of the two representative samples is about 5.14 %. The visually estimated portion of this total porosity, vuggy (4%) porosity, and calculated microporosity is ~1.14% (Figure 5.7c). The total measured porosity in the second sample is 10.62%. Using JMicroVision software, vuggy porosity in this sample was estimated at 8.2%, and thus suggesting that the remaining ~2.42% represents microporosity (Figure 5.8c). Vuggy porosity in the samples is characterized by small scattered disconnected pores (Figure 5.8a).

In this facies, the vugs are elongated and rounded, with few large square vugs in the second sample (Figure 5.8j). The aspect ratio is about 2 (elongated a little bit). The average roundness factor of 2 indicates rounded shape; and dominant pore size of vugs is 100 μm^2 for the first sample (Figure 5.7d) and 50 μm^2 for the second sample (Figure 5.8d).

The aspect ratio shows that there are not any variation in dimensions in different pore sizes suggesting that the pore size does not affect the pore dimensions (Figures 5.7e, 5.7g, 5.7i, 5.8e, 5.8g and 5.8i). Roundness factor shows rounded shape in all pore sizes in the first sample (Figures 5.7f, 5.7h and 5.7j) with minor degree of angularity present in the pores that larger 200 μm^2 in size in the second sample (Figures 5.8f, 5.8h and 5.8j). Both the aspect ratio and roundness factor confirm that pores are circular to elliptical shapes with minor large square vugs.

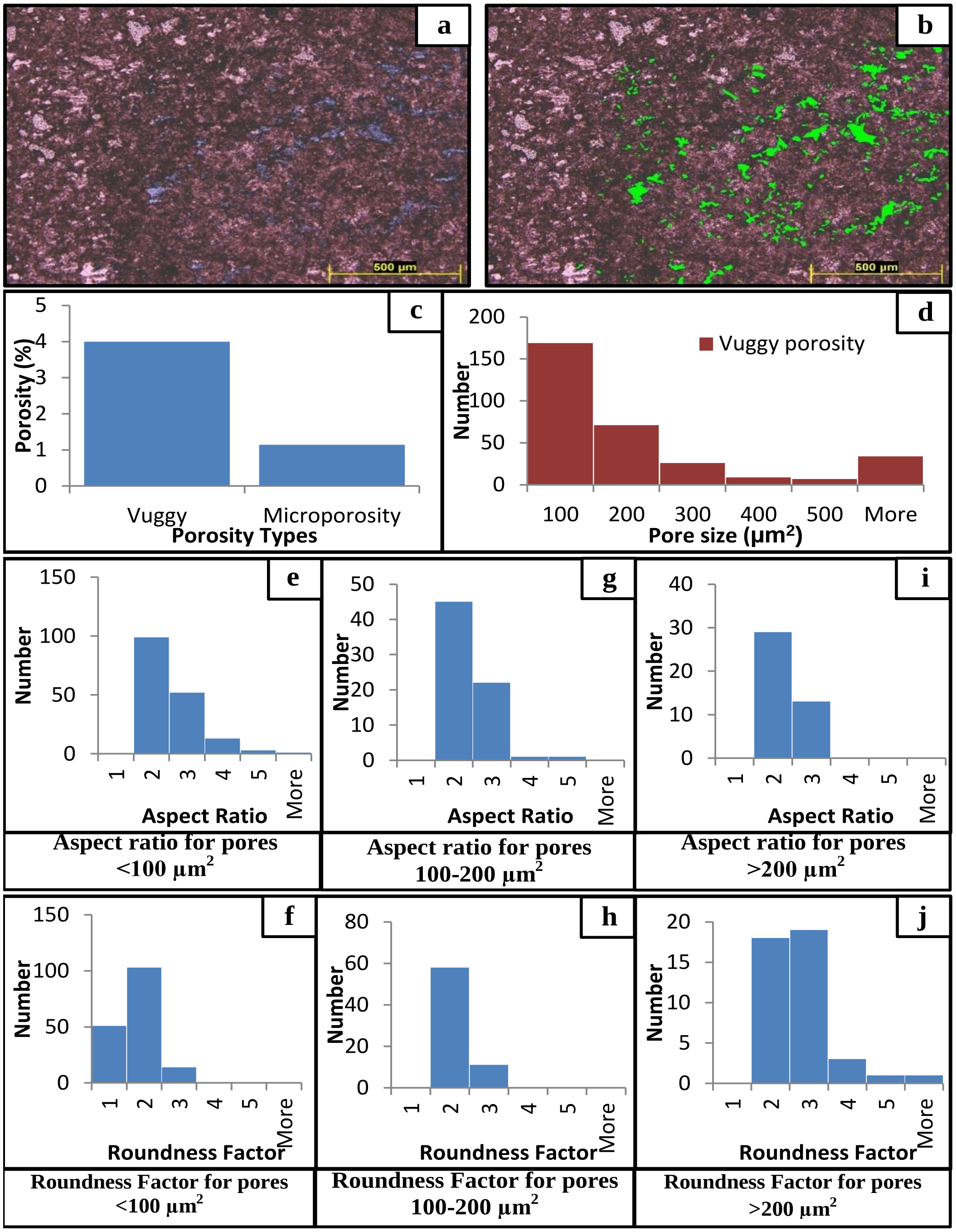

Aspect ratio for pores <100 µm^2

Aspect ratio for pores 100-200 µm^2

Aspect ratio for pores >200 µm^2

Roundness Factor for pores <100 µm^2

Roundness Factor for pores 100-200 µm^2

Roundness Factor for pores >200 µm^2

Figure 5.7: (a) representative microphotograph of the first thin section sample of the graded mudstone to packstone facies; (b) picked porosities in green using JMicroVision software; (c) The percentages of visual estimation of porosity and calculated microporosity; (d) The frequency distribution of vuggy porosity in different pore sizes; (e) & (f) The aspect ratio and roundness factor frequency distribution of pore sizes less than 100 µm^2 window respectively; (g) & (h) The aspect ratio and roundness factor frequency distribution of pore sizes between 100-200 µm^2 window respectively; and (i) & (j) The aspect ratio and roundness factor frequency distribution of pore sizes larger than 200 µm^2 window respectively.

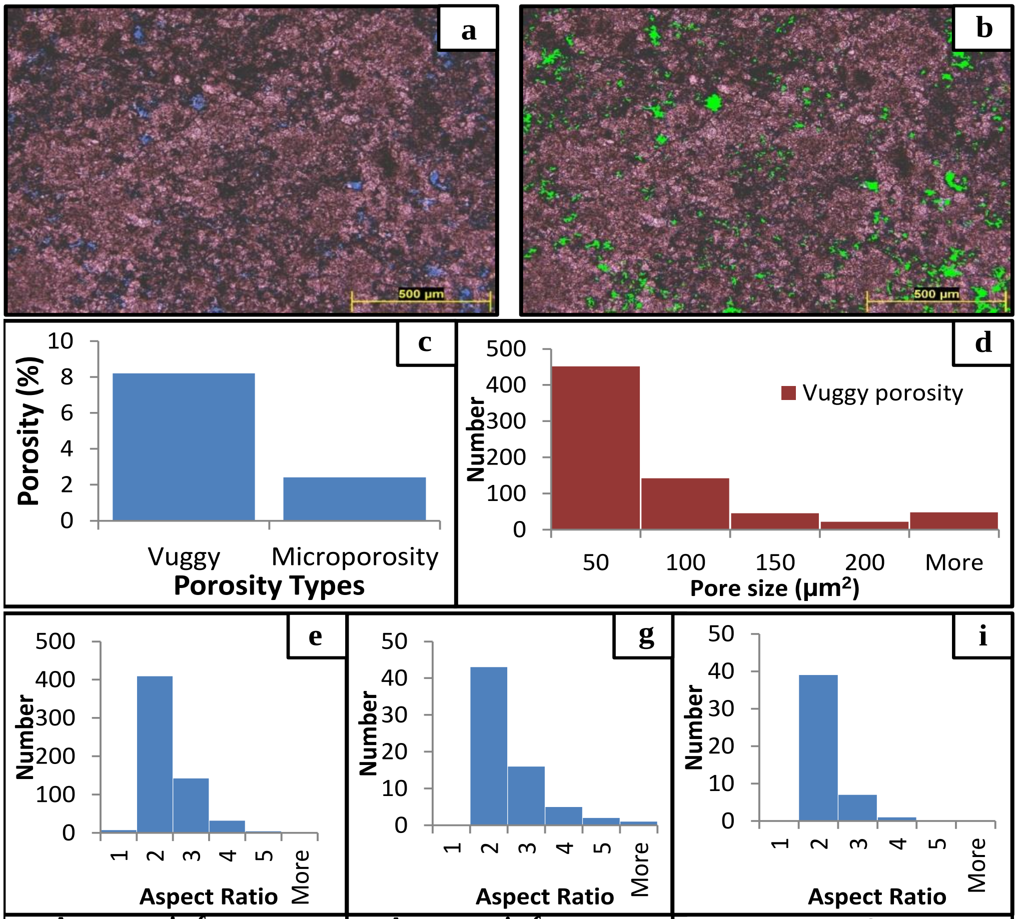

Aspect ratio for pores <100 µm²	Aspect ratio for pores 100-200 µm²	Aspect ratio for pores >200 µm²

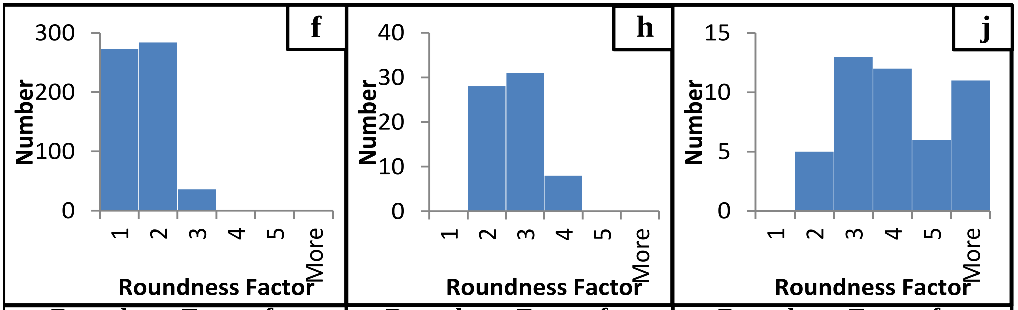

Roundness Factor for pores <100 µm²	Roundness Factor for pores 100-200 µm²	Roundness Factor for pores >200 µm²

Figure 5.8: (a) representative microphotograph of the second thin section of the graded mudstone to packstone facies; (b) picked porosities in green using JMicroVision software; (c) The percentages of visual estimation of porosity and calculated microporosity; (d) The frequency distribution of vuggy porosity in different pore sizes; (e) The aspect ratio and roundness factor frequency distribution of pore sizes less than 100 µm^2 window respectively; (g) & (h) The aspect ratio and roundness factor frequency distribution of pore sizes between 100-200 µm^2 window respectively; and (i) & (j) The aspect ratio and roundness factor frequency distribution of pore sizes larger than 200 µm^2 window respectively.

5.3.1.4. Dolostone

The samples from this facies are completely dolomitized containing both fabric preserved (Figures 5.9a and 5.10a) and non-fabric preserved dolomite (Figure 5.11a). The dolomite occurs as cement and also as dolomitized grains. Dolomitization is the major process responsible for enhancing and reducing the porosity. Intercrystalline and intracrystalline porosities are the common types of porosity in the samples, with some vuggy pores.

In the analyzed samples, the total measured core porosity was around 10% and permeability was about 0.4 md.

This facies which is characterized by intercrystalline, intracrystalline and vuggy porosities is represented by three samples. In the first sample, intercrystalline pores are the dominant pore type mainly associated with dolomite crystals (Figure 5.9a). The total porosity measured from the core plug was 10.1%. This total porosity is shared between intercrystalline porosity (7%) intracrystalline porosity (1%) and microporosity (~2.1%) (Figure 5.9c). The dominant pore type in the second sample is intracrystalline porosity with a minor percentage of intercrystalline porosity (Figure 5.10a). Intracrystalline pores found mainly between the dolomite crystals were produced as a result of partial dissolution of the dolomite crystals. The total porosity measured from core plug was 10%. From visual estimation, the intracrystalline porosity is about 5% while intercrystalline type accounts for 2% of the total porosity. Therefore the microporosity in the sample is ~3% (Figure 5.10c). In the third sample, vuggy porosity is the dominant pore types and it is characterized by a group of small vugs associated with each other. The total porosity measured from core plug was 8.17%. Using JMicroVision software to calculate the visual estimation of porosity, 4.1% was obtained for vuggy porosity. Thus the remaining ~4.07% is considered as microporosity in the sample (Figure 5.11c).

Intercrystalline porosity in this facies appears to be of large size, angular and elongated a little bit closer to square and rectangular shapes. Aspect ratio is between 1 and 2 (equidimensional) and roundness factor 3 in average indicating rounded pores. A few pores show some elongation and angularity in sizes larger than 200 µm^2. Average size of intercrystalline pores is 200 µm^2 in both samples (Figures 5.9d and 5.10d).

Aspect ratio shows no variation with changing pore sizes. A majority of intercrystalline pores are elongated in all pore size windows. Roundness factor shows rounded in small pores sizes, but in those that larger than 200 µm^2 in size are more angular in shape. The combination of aspect ratio and roundness factor confirms small rounded circular pores with large pore exhibiting square to rectangular shapes in both samples.

Intracrystalline porosity is delineated mainly by angular and elongated pores forming shapes closer to a rectangle. The aspect ratio of 3 obtained in second samples, suggests elongated pore (Figures 5.9e, 5.9g, 5.9i, 5.10e, 5.10g and 5.10i). An average roundness factor of 4 indicates angular shape in the first sample, but the roundness factor in the second sample is less than 3 in general indicating rounded pores. In pore sizes larger than 200 µm^2, a minor fraction of angular pores are developed (Figures 5.9f, 5.9h and 5.9j). The average size of the intracrystalline pores is 50 µm^2 for the first sample (Figure 5.9d) and 100 µm^2 for the second sample (Figure 5.10d). Aspect ratio and roundness factor show small elongated rounded elliptical pores, and a few large size pores with angular, elongated or rectangular shapes.

Vuggy porosity in this facies mainly shows elliptical with some rectangular vugs. An average aspect ratio of 2 is also interpreted as elongated pores. An average roundness factor of 2 in indicates rounded shape. The average size of vuggy pores in the sample is 150 μm^2 (Figure 5.11d).

Aspect ratio shows that the pores are elongated as the pore size increases (Figures 5.11e, 5.11g and 5.11i). Roundness factor shows the smaller pores are rounded and that pores larger than 200 μm^2 in size are angular in shape (Figures 5.11f, 5.11h and 5.11j). A combination of aspect ratio and roundness factor shows that the small pores are elongated, rounded and elliptical in shape, and the shape of the large pores are elongated rounded partly angular to sub-angular elliptical in shape.

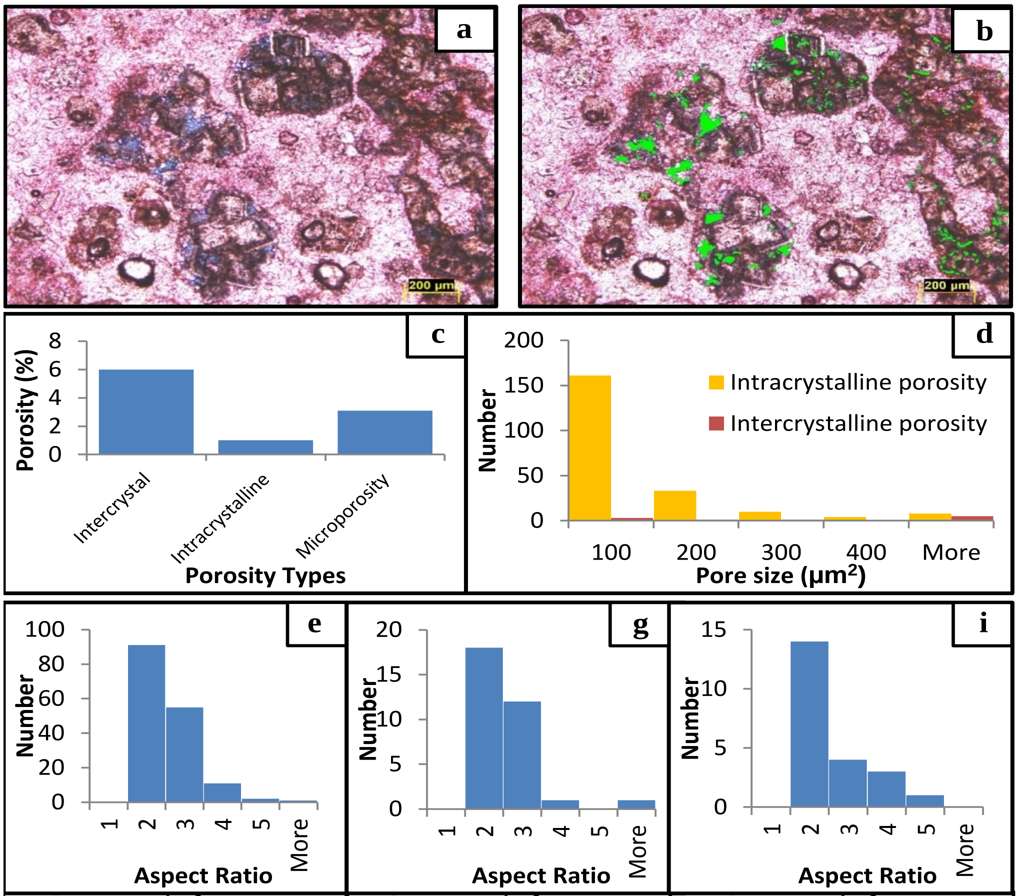

Aspect ratio for pores <100 µm^2

Aspect ratio for pores 100-200 µm^2

Aspect ratio for pores >200 µm^2

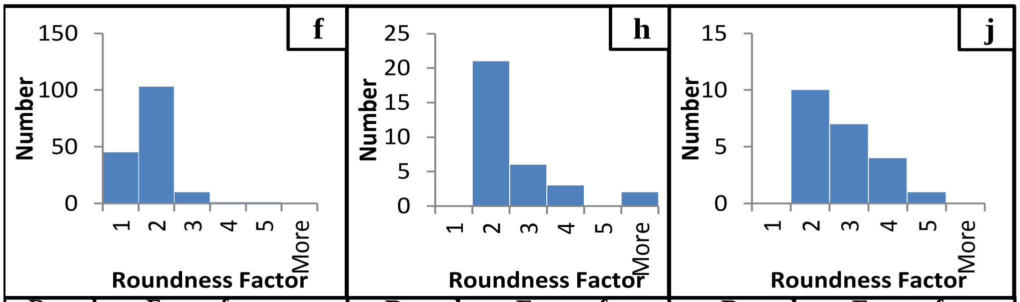

Roundness Factor for pores <100 µm^2

Roundness Factor for pores 100-200 µm^2

Roundness Factor for pores >200 µm^2

Figure 5.9: (a) representative microphotograph of the first thin section sample of the dolostone; (b) picked porosities in green using JMicroVision software; (c) The percentages of visually estimated porosity and calculated microporosity; (d) The frequency distribution of intracrystalline and intercrystalline porosity in different pore sizes; (e) & (f) The aspect ratio and roundness factor frequency distribution of pore sizes less than 100 µm^2 window respectively for intracrystalline porosity, and (k) & (l) for intercrystalline porosity; (g) & (h) The aspect ratio and roundness factor frequency distribution of pore sizes between 100-200 µm^2 window respectively for intracrystalline porosity; and (i) & (j) The aspect ratio and roundness factor frequency distribution of pore sizes larger than 200 µm^2 window respectively for intracrystalline porosity, and (m) (n) for intercrystalline porosity.

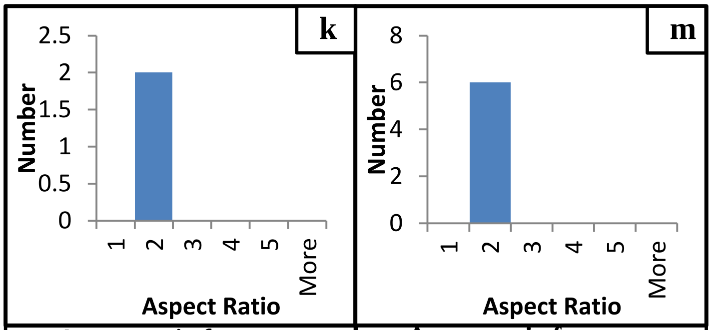

Aspect ratio for pores <100 µm²

Aspect ratio for pores >200 µm²

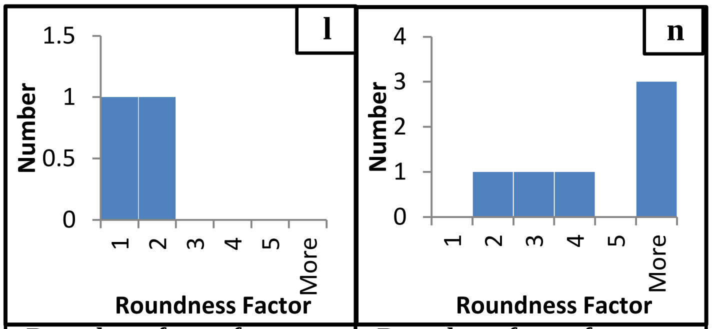

Roundness factor for pores <100 µm²

Roundness factor for pores >200 µm²

Figure 5.9: (Continued).

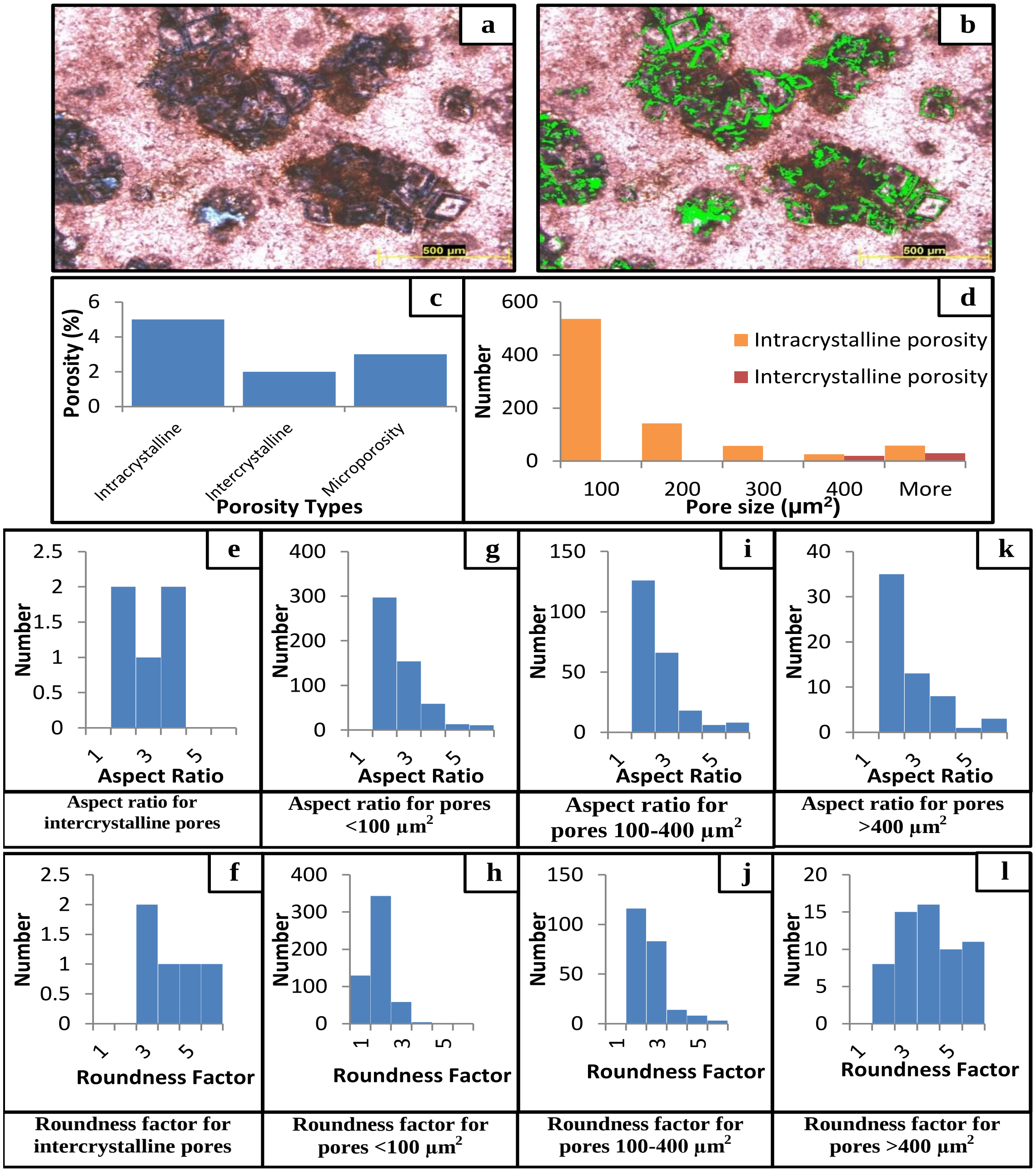

Aspect ratio for intercrystalline pores

Aspect ratio for pores <100 µm²

Aspect ratio for pores 100-400 µm²

Aspect ratio for pores >400 µm²

Roundness factor for intercrystalline pores

Roundness factor for pores <100 µm²

Roundness factor for pores 100-400 µm²

Roundness factor for pores >400 µm²

Figure 5.10: (a) representative microphotograph of the second thin section sample of the dolostone; (b) picked porosities in green using JMicroVision software; (c) The percentages of visual estimation of porosity and calculated microporosity; (d) The frequency distribution of intracrystalline and intercrystalline porosity in different pore sizes; (e) & (f) The aspect ratio and roundness factor frequency distribution of intercrystalline porosity; (g) & (h) The aspect ratio and rounded factor frequency distribution of pore sizes less than 100 µm^2 window respectively for intracrystalline porosity; (i) & (j) The aspect ratio and rounded factor frequency distribution of pore sizes between 100-400 µm^2 window respectively for intracrystalline porosity; and (k) & (l) The aspect ratio and rounded factor frequency distribution of pore sizes larger than 400 µm^2 window respectively for intracrystalline porosity.

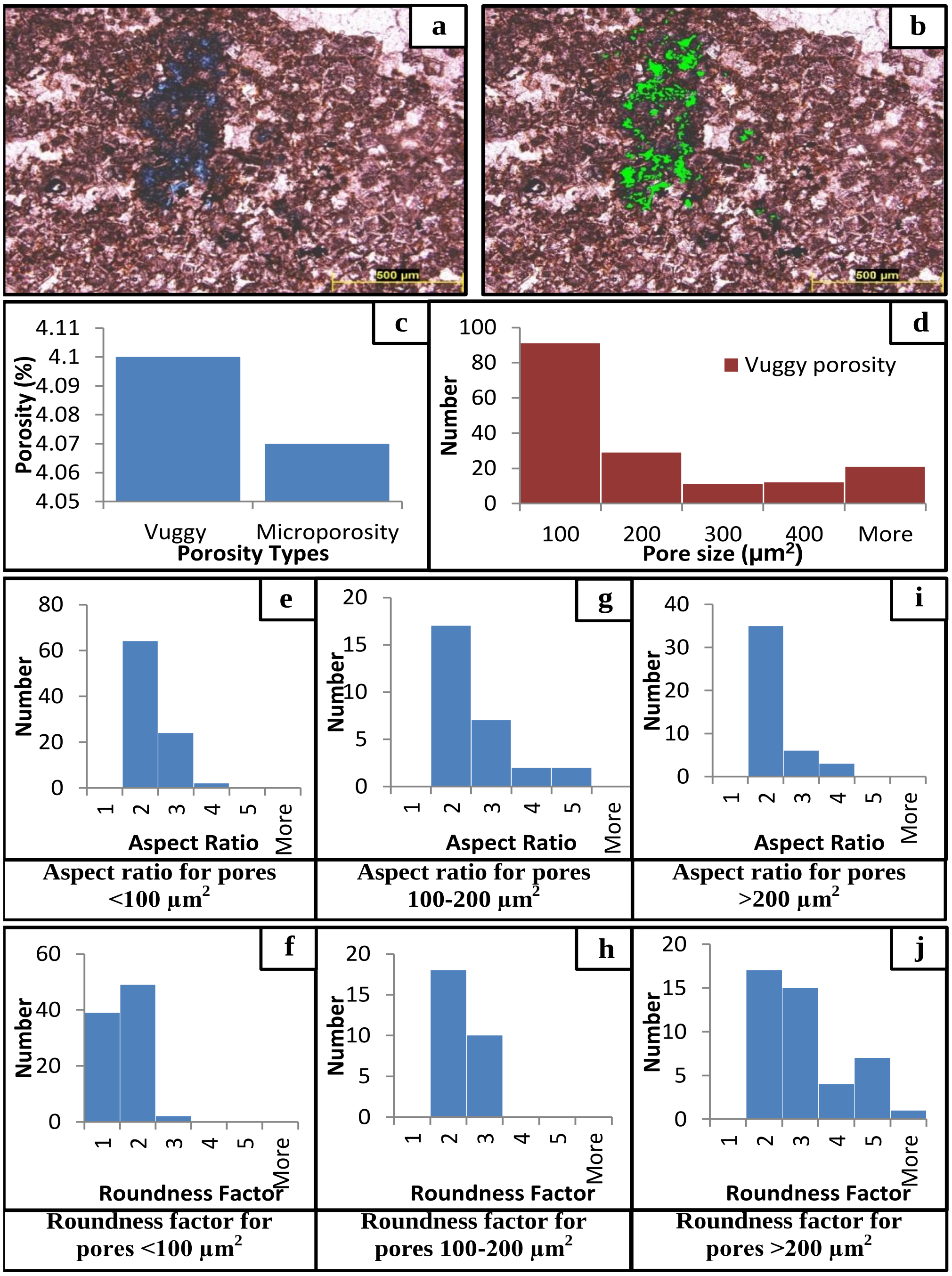

Aspect ratio for pores <100 µm^2

Aspect ratio for pores 100-200 µm^2

Aspect ratio for pores >200 µm^2

Roundness factor for pores <100 µm^2

Roundness factor for pores 100-200 µm^2

Roundness factor for pores >200 µm^2

Figure 5.11: (a) representative microphotograph of the third thin section sample of the dolostone; (b) picked porosities in green using JMicroVision software; (c) The percentages of visually estimated porosity and calculated microporosity; (d) The frequency distribution of vuggy porosity in different pore sizes; (e) & (f) The aspect ratio and roundness factor frequency distribution of pore sizes less than 100 µm^2 window respectively; (g) & (h) The aspect ratio and roundness factor frequency distribution of pore sizes between 100-200 µm^2 window respectively; and (i) & (j) The aspect ratio and roundness factor frequency distribution of pore sizes larger than 200 µm^2 window respectively.

5.4. XRD Mineral Identification

The XRD analysis for the three lithofacies reveals calcite minerals in well-sorted oolitic grainstone, graded mudstone to packstone facies (Figure 5.12). Calcite along with some traces of dolomite minerals was identified in the cross-bedded oolitic fossiliferous grainstone facies (Figure 5.12). Mixtures of dolomite and calcite minerals are present in the dolostone facies (Figure 5.12). Pure calcite mineral was identified in the graded mudstone to packstone facies (Figure 5.12).

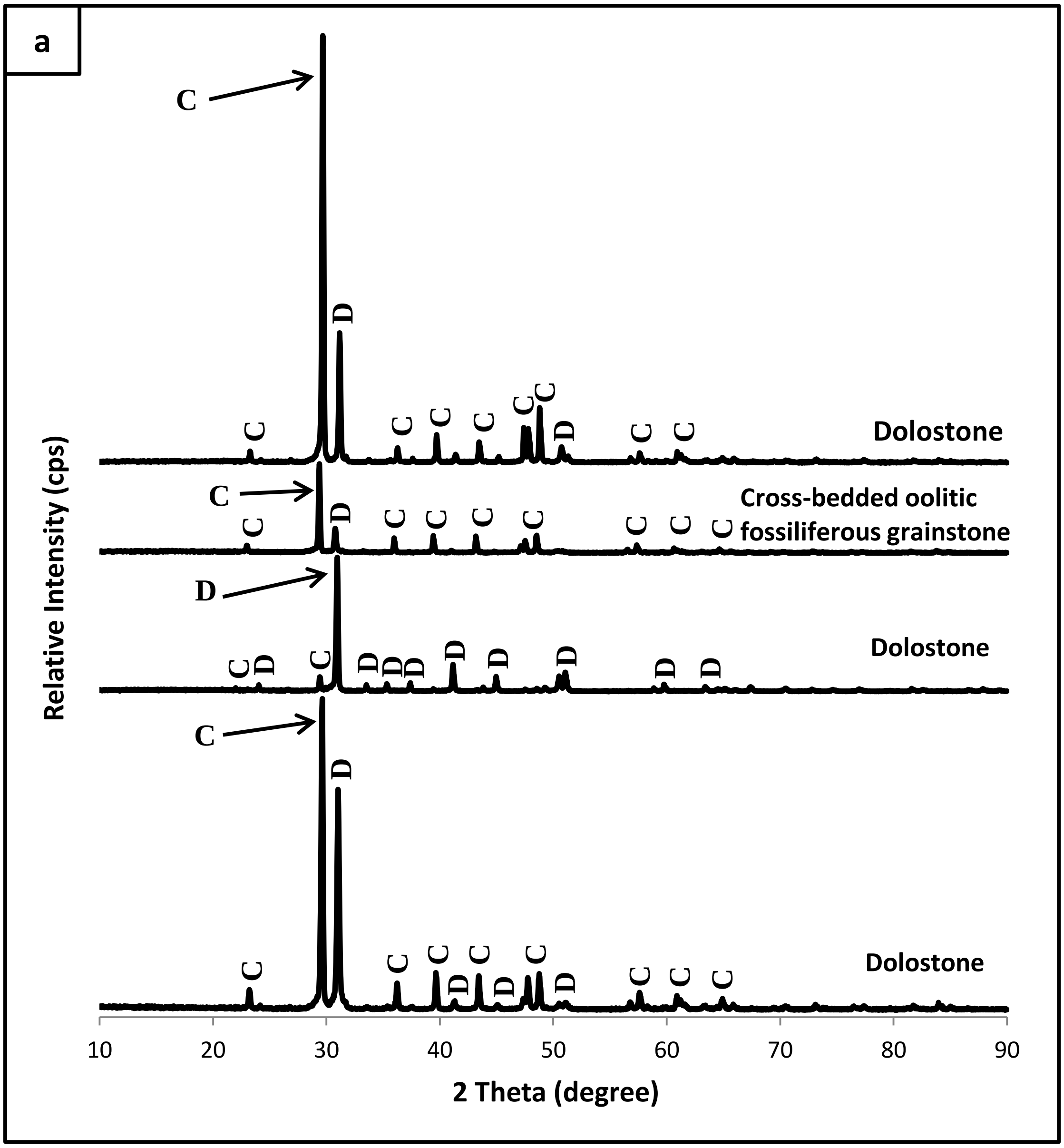

Mineral abbreviation	Phase Name	Formula	Space Group
C	Calcite	Ca CO_3	167 : R-3c,hexagonal
D	Dolomite	Ca Mg $(CO_3)_2$	148 : R-3,hexagonal

Figure 5.12: The XRD signatures for each lithofacies with identified peaks (abbreviated minerals). The minerals abbreviations, phase name, formula and space group are illustrated in the table.

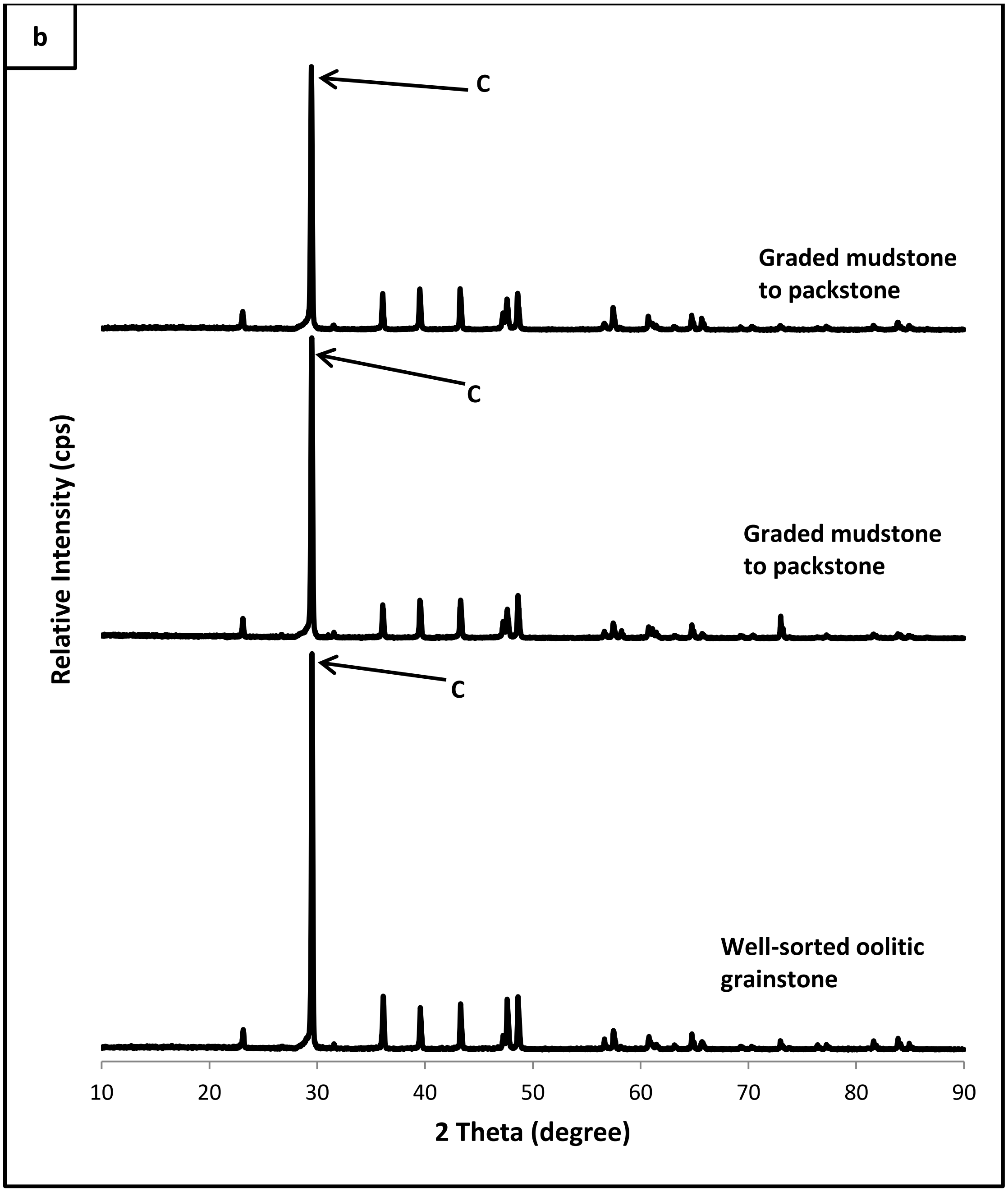

Mineral abbreviation	Phase Name	Formula	Space Group
C	Calcite	Ca (CO_3)	167 : R-3c,hexagonal

Figure 5.12: (Continued).

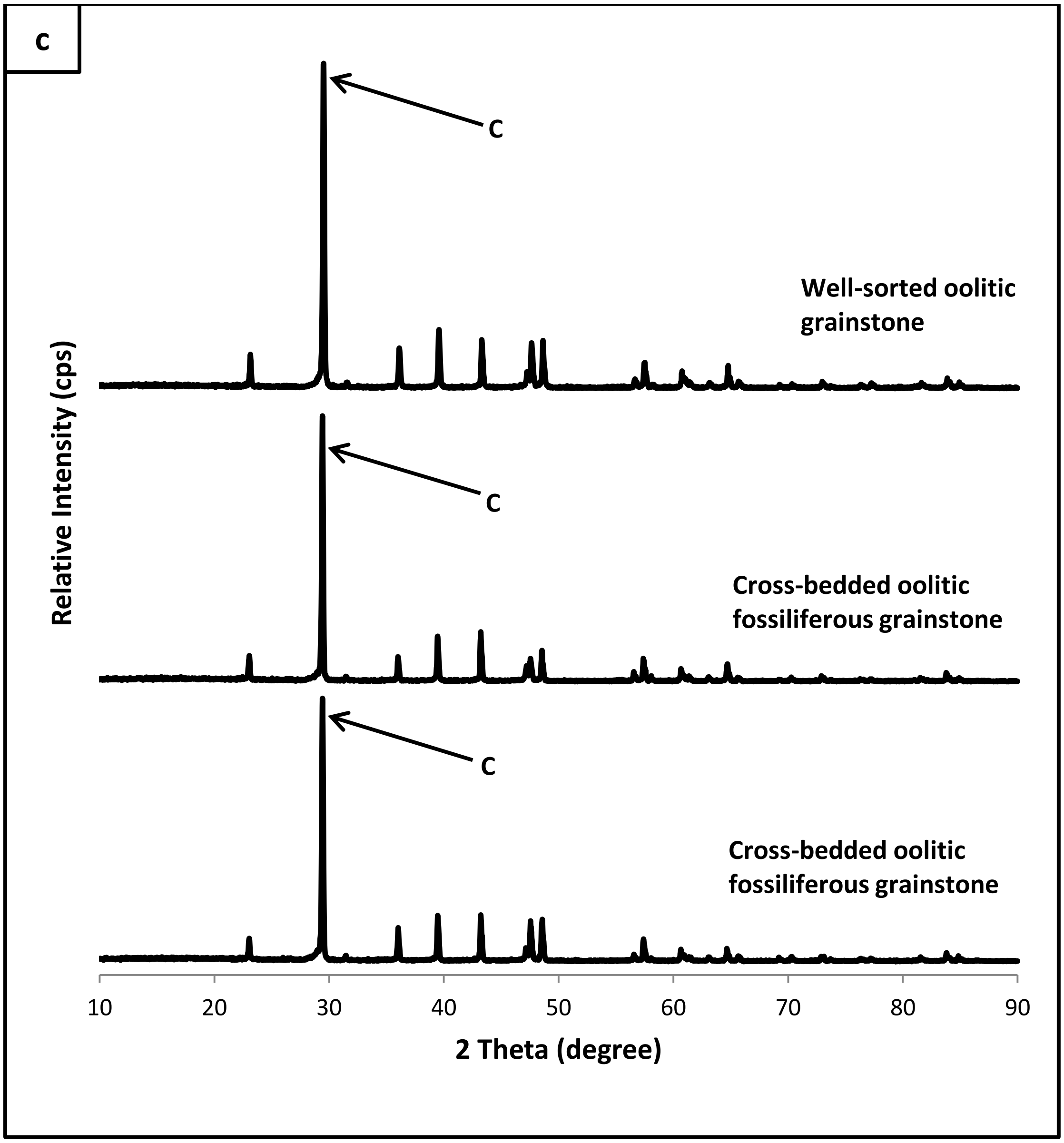

Mineral abbreviation	Phase Name	Formula	Space Group
C	Calcite	Ca (CO_3)	167 : R-3c,hexagonal

Figure 5.12: (Continued).

5.5. Linking Porosity Types with Their Geometrical Shapes and Lithology

The relationships between porosity types and facies were established based on the studied thin sections (Figure 5.13). The porosity types in selected samples were plotted against their geometries (Figure 5.14).

From the studied thin sections, the relationships between abundant pore types within certain lithology were identified. The moldic porosity is restricted to the grainstone facies. It was formed from the molds of ooids and skeletal (mainly bivalve) grains. The vuggy porosity varies in shapes and sizes depending on the facies. The large size vugs are mainly associated with grainstone as a result of poor micrite envelopes of ooids and skeletal grains (Figure 5.13). In the muddy and dolomitic facies, vuggy porosity shows small sizes with scattered or sometimes concentrated in certain areas. Intergranular and intragranular porosities mainly occur in the grainstone facies. Intercrystalline and intracrystalline porosity are associated with the dolostone facies (Figure 5.14).

Moldic porosity has variety of pore sizes that are mainly controlled either by the original grains size (ooids or skeletal) or by diagenesis. Cementation is the main diagenetic control of the pore size. Some molds are filled partially or completely by calcite cement, which produce small pores without connection in 2D thin section view. Most of the molds that are produced from ooids are characterized by equidimensional well-rounded circles. Bivalve molds show elongated angular rectangle pores, but sometimes inside molds cementation may change that a little bit.

Vuggy porosity has different sizes depending on the original facies (small in mudstone/wackestone and large in grainstone) (Figure 5.14). Also poor micrite envelopes of the original grains may have converted the moldic porosity to vuggy porosity. In addition, two different porosity types might have also stacked together to form complex shape of vugs. Vuggy porosity can be angular or rounded equidimensional or elongated in shapes (Figure 5.14).

Intercrystalline porosity usually has very small size, equidimensional and sometimes elongated and angular in most cases. The common most geometry is the square shape (Figure 5.14). Intracrystalline porosity is the smallest porosity type. It is angular and elongated because it usually takes the shape of the dolomite crystals. The common geometry is rectangular shape (Figure 5.14).

Intergranular porosity has variable sizes depending on compaction, cementation, and sorting. In general the pore type is characterized by elongated and angular shape geometries. The elongation describes the pore connectivity, and the angularity appears when the grains start touching each other to close the pore throat. Cementation may change the pore shape, and may divide the large pore into smaller pores.

Fracture porosity provides extremely good connectivity. It looks like a rectangle because it is elongated and angular. Cementation acts as seal that reduces fracture elongation. Most of the fractures in the thin section are filled with calcite cement.

5.5.1. Porosity Types Ranking

In this study, a strong relationship between facies and pore type has been noticed (Figure 5.13). Following this relationship, vuggy porosity was divided into two different pores (vuggy-1 and vuggy-2) due to the differences in the facies and the differences in the pore geometry. Vuggy-1 is the vuggy porosity that occupies grainstone facies, and vuggy-2 is the pores formed in the wackestone/mudstone facies. Vuggy-1 is characterized by very large pores with complex geometry (Figure 5.14). Vuggy-2 is characterized by small rounded pores (Figure 5.14).

Moldic porosity was also divided into two types depending on the type of mold whether this molds a result of ooids or skeletal grains dissolution (mostly bivalve). Oomoldic is the moldic porosity that is produced as a result of oolitic grains dissolution. Skelmoldic is the moldic porosity that developed in place of dissolved skeletal grains. Oomoldic is characterized by well-rounded molds (circle) (Figure 5.14), and skelmoldic is distinguished by the elongated angular shape (rectangular) (Figure 5.14) because most of the molds are originally dissolved bivalves.

The porosity types were ranked into eight classes depending on the mean pore size. The classes range from 1 to 8 in sequential order. One represents the worst pore type and eight is the best (Figure 5.14). Also by calculating the percent of each pore type to represent the contribution of each pore type in the total porosity that may add more reliable quality ranking for each pore type as shown in Figure 5.14).

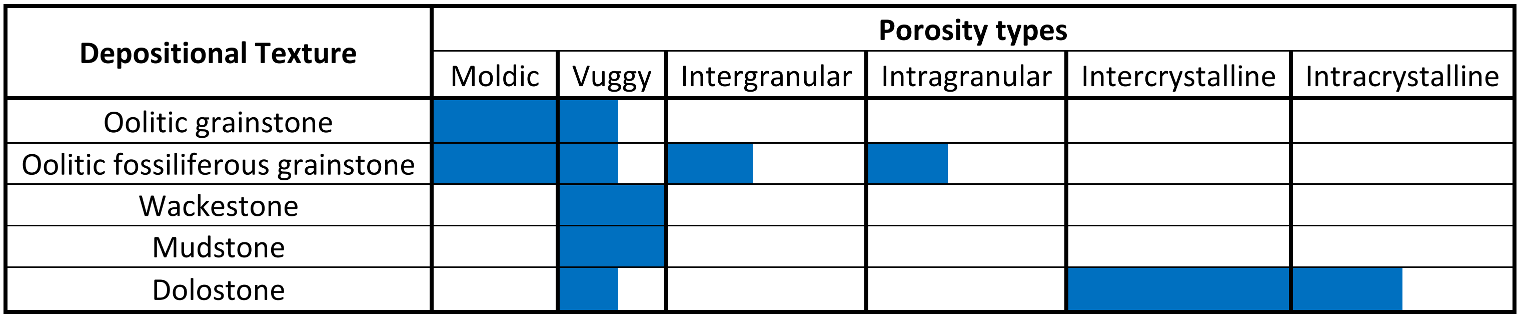

Depositional Texture	Porosity types					
	Moldic	Vuggy	Intergranular	Intragranular	Intercrystalline	Intracrystalline
Oolitic grainstone	■	▌				
Oolitic fossiliferous grainstone	■	▌	▌	▌		
Wackestone		■				
Mudstone		■				
Dolostone		▌			■	▌

Figure 5.13: the relationship between the lithology (depositional texture) and abundant pore types.

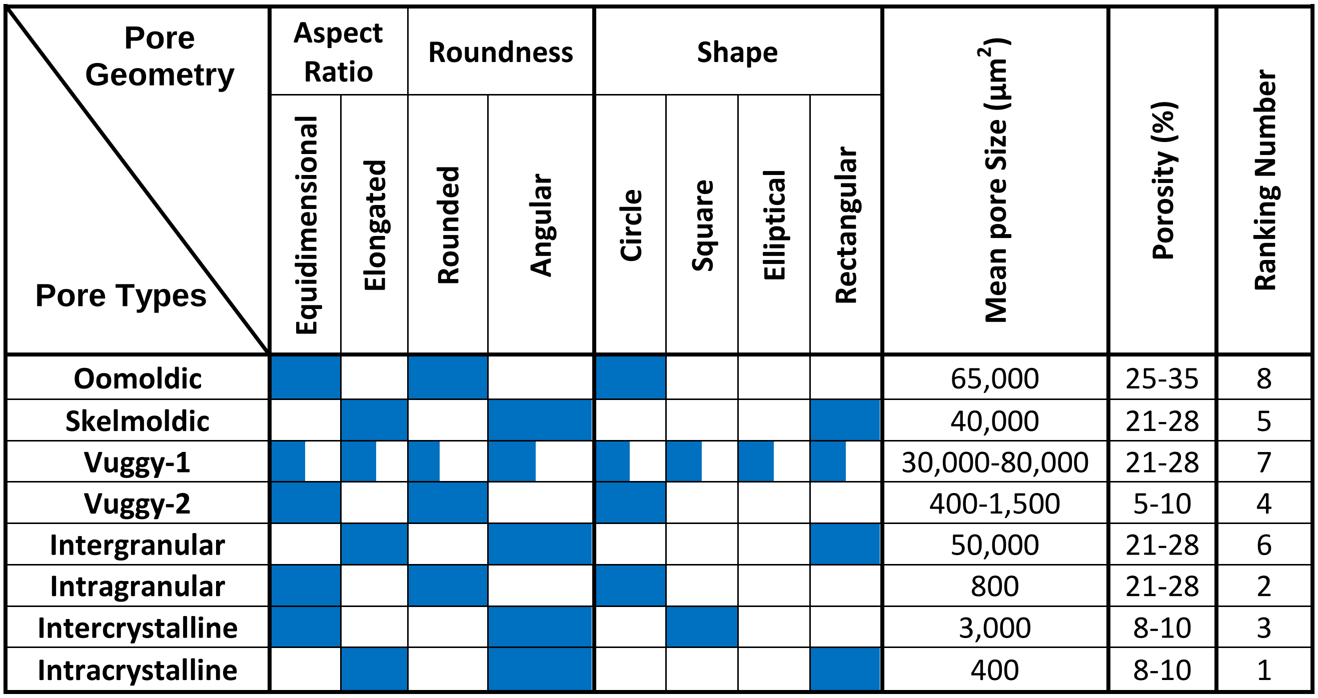

Pore Geometry / Pore Types	Aspect Ratio		Roundness		Shape				Mean pore Size (μm^2)	Porosity (%)	Ranking Number
	Equidimensional	Elongated	Rounded	Angular	Circle	Square	Elliptical	Rectangular			
Oomoldic	■		■		■				65,000	25-35	8
Skelmoldic		■		■				■	40,000	21-28	5
Vuggy-1	▌	▌	▌	▌	▌	▌	▌	▌	30,000-80,000	21-28	7
Vuggy-2	■		■		■				400-1,500	5-10	4
Intergranular		■		■				■	50,000	21-28	6
Intragranular	■		■		■				800	21-28	2
Intercrystalline	■			■		■			3,000	8-10	3
Intracrystalline		■		■				■	400	8-10	1

Figure 5.14: The relationship between different pore types and their geometrical shapes.

5.6. Discussion

The study confirmed that each pore type has its own distinguish geometry and size (Figure 5.13). In general there are not any major changes in the pore geometry with increasing or decreasing pore size for the same pore type.

Dolomitization in the Upper Khartam Member enhances the porosity when it invades the mudstone/wackestone facies. But in the dolomitized layers the meteoric cementation closed the effective porosity. However, dolomitization destroys both porosity and permeability when it grows as cement inside the moldic and vuggy porosity (Figure 5.1d). In the subsurface Khuff equivalent in Pars gas filed in Iran, Tavakoli et al. (2011) mentioned that, dolomitization enhances the porosity and permeability. However, in certain zones anhydrite cements plugged these pores.

The best quality pores are the vuggy-1 and oomoldic porosities. However, the outcrop study in the same locality by Janson et al. (2014) indicated that oomoldic porosity has high porosity but less permeability. Similar to the present study, they ranked oomoldic as the worst in terms of permeability and the best in term of porosity. Also Layman II (2002) ranked the moldic porosity as good to intermediate quality while the vuggy porosity has the worst quality mainly due to insufficient diagenetic dissolution in the studied reservoir.

The quality of the vuggy porosity in the studied samples is mainly facies controlled. The mudstone/wackestone facies have the lowest quality of the vuggy porosity (small pore sizes). On the other hand, the grainstone facies has the highest quality of the vuggy porosity (large pore size). The possible reasons for having large sizes of vugs in the grainstone facies are that:

1- The initial permeability was high thus allowing more of dissolving solutions to able to penetrate this grainy facies to create large pores (vugs).

2- Some of the oolitic grains have weak micrite envelopes such that at the stage of ooids dissolution they are able to form vugs instead of forming molds.

3- In some cases, the association of oolitic grains is preserved by one micrite envelopes, and then the large vugs are later created during dissolution event.

These reasons also increase the reservoir quality, because they are responsible for creation of vuggy and moldic porosities which they have the highest ranking number 7 and 8.

CHAPTER SIX

PETROPHYSICAL CHARACTERISTICS

6.1. Introduction

Porosity and permeability are the fundamental parameters that determine reservoir quality. In order to evaluate a reservoir quality, it is essential to accurately predict the porosity and permeability distribution patterns. Porosity can be determined easily from wire line logs in the subsurface, but permeability cannot be determined directly from logs. Therefore, porosity-permeability relationship is needed to determine the permeability in a given porosity. Linking the porosity-permeability relationship with their depositional texture is extremely important in the prediction of porosity and permeability in the proximal and distal sites.

Samples were collected from nine vertical sections from the Upper Khartam Member at the outcrop (Figure 6.1), in order to obtain a statistically significant number of samples to perform porosity-permeability cross plots and to determine the heterogeneity in the porosity and permeability.

In this part, the cross plots between porosity and permeability for each depositional texture which can be used to make better prediction of the porosity and permeability with reference to the facies. In addition, statistical parameters were used to reveal the heterogeneity of both the porosity and permeability.

6.2. Porosity-Permeability Relationships

Upper Khartam Member of the Khuff Formation consists of mainly mudstone, wackestone, packstone and grainstone. The cross plot of porosity and permeability data derived from all the lithofacies combined, shows poor correlation (R^2 = 0.23) (Figure 6.2). However, the correlation improved significantly when porosity and permeability values for each depositional rock texture (fabric) were cross plotted separately (Figure 6.4).

The statistical parameters for whole porosity population for all the lithofacies combined are shown in Table 6.1. The histograms of the porosity shows unimodal distribution with positive skewness (left skewed). The porosity has one mode positioned at 5% (Figure 6.3a). Permeability also shows bimodal distribution with positive skewness (left skewed). The permeability has two modes positioned at 5 md and 30 md (Figure 6.3b).

After considering the depositional textures, the porosity-permeability cross plot improved significantly from R^2 = 0.23 for whole population to R^2 = 0.62, 0.81, 0.46, and 0.45 for mudstone, wackestone, packstone, and grainstone, respectively (Figures 6.4a, 6.4b, 6.4c and 6.4d).

These samples contain outliers that represent real data. The outliers are belonging to grainstone texture with high permeability due to dominance of intergranular porosity that shows good connectivity (Figures 6.7c and 6.7f). Unlike other grainstone texture that have vuggy and moldic porosity with no visible connection in the 2D thin section view (Figures 6.7a and 6.7d).

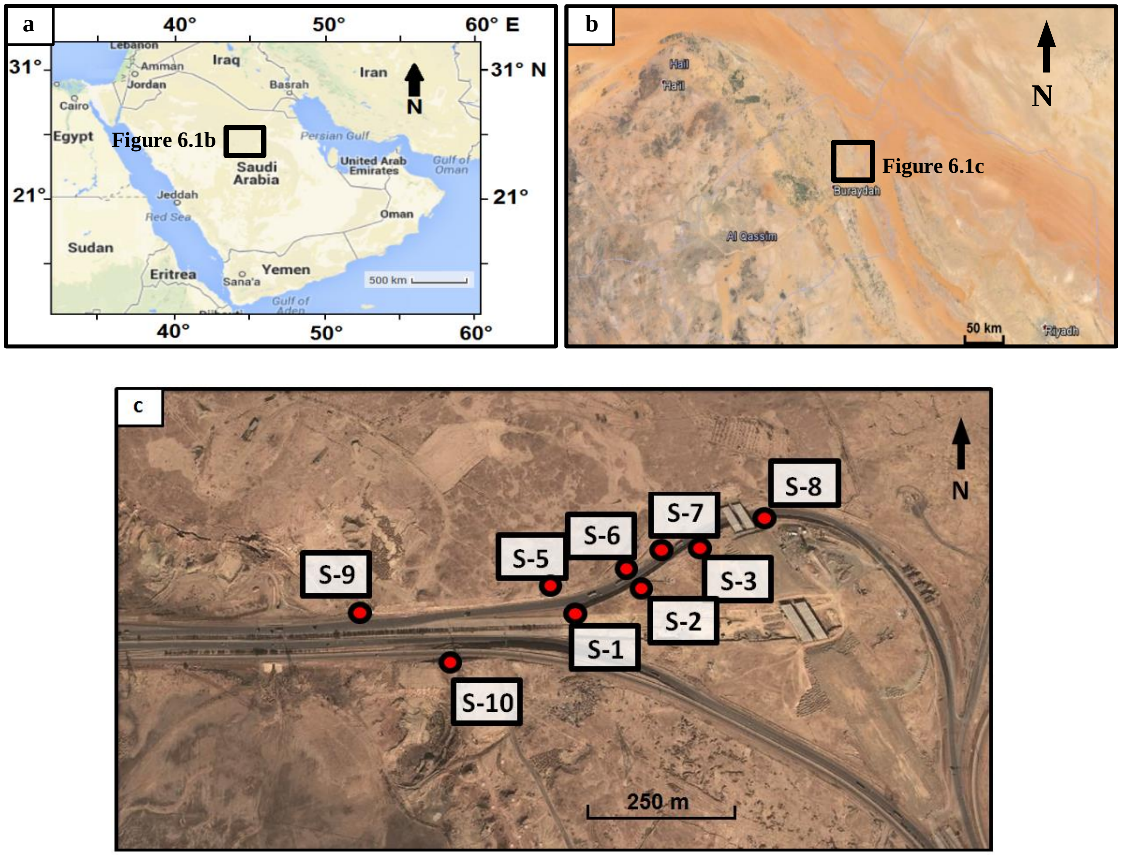

Figure 6.1: (a) Map showing the location of the study area highlighted with black box in the central Saudi Arabia; (b) close look of the region of the study area; and (c) map showing the location of the nine vertical sections of the studied outcrop (Google Maps, 2013).

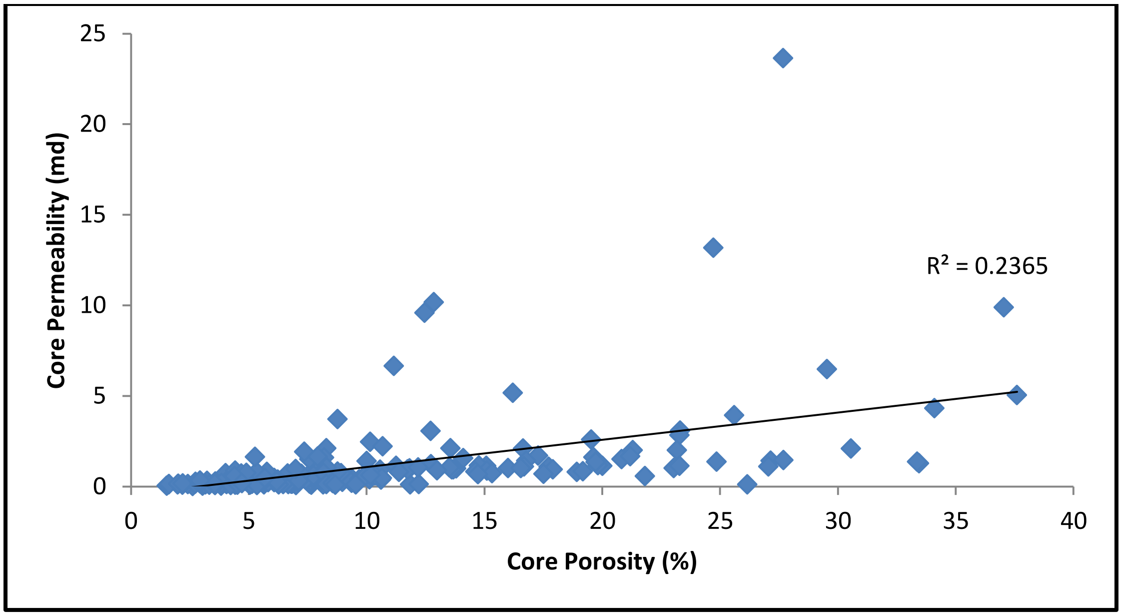

Figure 6.2: Whole core porosity vs. permeability cross plot for all samples of the Upper Khartam Member.

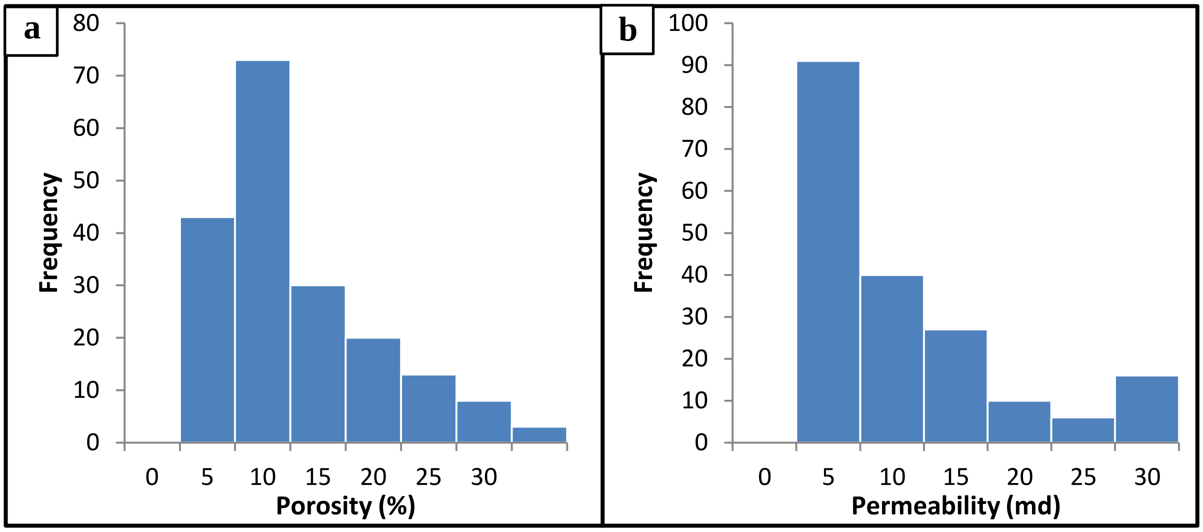

Figure 6.3: (a) & (b) showing the frequency distributions of porosity and permeability respectively.

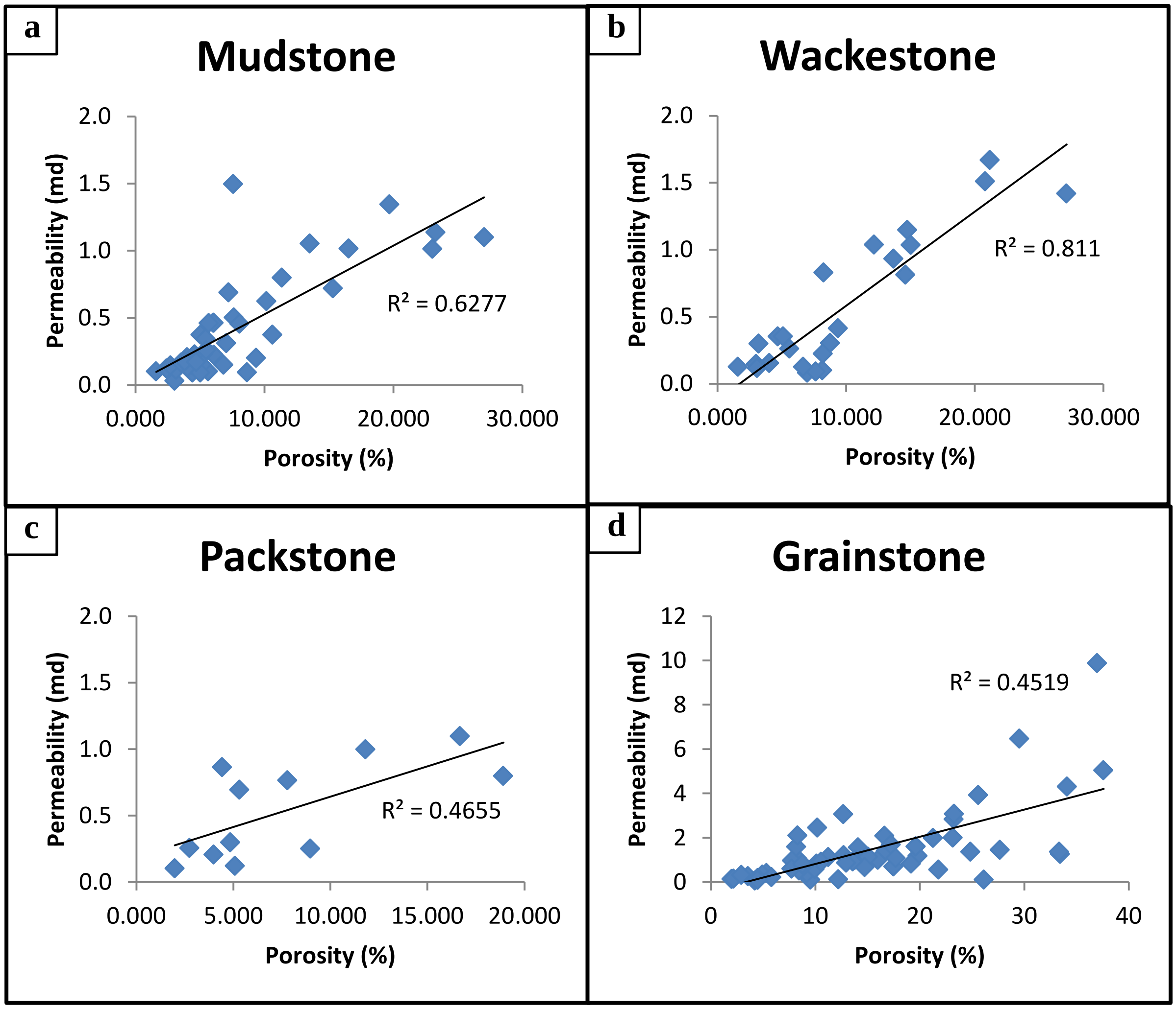

Figure 6.4: (a); (b); (c); and (d) are porosity-permeability relationships based on the lithofacies (mudstone, wackestone, packstone, and grainstone respectively).

6.3. Statistical Parameters of Porosity

The porosity values in the 138 samples analyzed range from 1.5 to 37.5%. Statistical parameters were determined for the whole population of porosity derived from all the lithofacies combined (Table 6.1).

The porosity values in the 60 grainstone samples analyzed range from 2.0 % to 37.6%. The statistical parameters for this rock fabric are presented in Table 6.2. Packstone represented by 12 samples, are characterized by porosity values ranging from 2.0 % to 18.9%. Similarly, the porosity values in the 24 wackestone samples studied, fall between 2.0 % and 21.1%. The 24 mudstone samples that were analyzed are characterized by values that range from 1.6 % to 19.7% (Table 6.2). Box plot of the porosity values shows the important statistical parameters for each depositional rock texture (Figure 6.5). The box plot reveals that the grainstone fabric is dominated by the highest porosity samples with minor highly and that of all the lithofacies, the mudstone fabric has the lowest porosity values. Few samples from this rock type have fracture porosity.

Table 6.1: Statistical parameters of porosity for all samples.

Median	8.56
Skewness	1.19
Kurtosis	0.86
Mode	19.63
Average (mean)	11.39
Variance (S^2)	68.12
Standard Deviation (S)	8.25
Coefficient of Variance (CV)	0.72

Table 6.2: Statistical parameters of porosity for each depositional texture.

	Mudstone	**Wackestone**	**Packstone**	**Grainstone**
Minimum	1.516	1.615	1.984	2.005
25th Percentile	4.463	5.017	4.316	8.307
Median	5.859	8.191	5.203	13.291
75th Percentile	9.190	13.919	9.685	20.181
Maximum	27.046	27.140	18.920	37.602
Skewness	1.754	1.129	1.171	0.731
Kurtosis	2.547	0.892	0.350	-0.167
Average (mean)	8.110	9.751	7.716	15.163
Variance (S^2)	36.027	42.537	29.759	84.515
Standard Deviation (S)	6.002	6.522	5.455	9.193
Coefficient of Variance (CV)	0.740	0.669	0.707	0.606

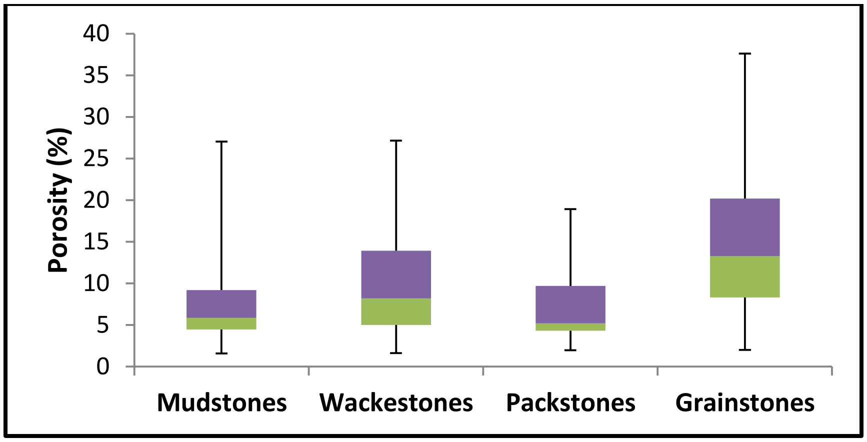

Figure 6.5: Box plot of porosity showing the minimum, first quartile, median, third quartile, and maximum porosity values for each depositional texture.

6.4. Statistical Parameters of Permeability

The permeability values in the 138 samples examined, range from 0.03 to 9.88 md. Statistical parameters for permeability derived from for all the rock fabrics combined were obtained (Table 6.3).

The permeability values for the grainstone fabric range from 0.07 to 9.88 md while those of the packstone range between 0.24 and 1.10 md. The values for the wackestone texture range from 0.08 to 1.66 md and the mudstone fabric is characterized by values ranging from 0.03 to 1.48 md (Table 6.4). The statistical parameters for each texture are also shown in Table 6.4. The box plot (Figure 6.6) shows that the grainstone is dominated by the highest permeability values. Only few samples from this rock type are characterized by low values. The mudstone rock type is characterized by the lowest permeability. Some of the samples from this rock type having fracture permeability (Figure 6.6).

Table 6.3: Statistical parameters for the whole permeability population.

Median	0.57
Skewness	4.11
Kurtosis	23.18
Mode	1.42
Average (mean)	0.90
Variance (S^2)	1.53
Standard Deviation (S)	1.24
Coefficient of Variance (CV)	1.37

Table 6.4: Statistical parameters of permeability for each depositional texture.

	Mudstone	**Wackestone**	**Packstone**	**Grainstone**
Minimum	0.030	0.080	0.103	0.070
25th Percentile	0.150	0.140	0.241	0.490
Median	0.246	0.327	0.497	1.002
75th Percentile	0.593	0.958	0.815	1.612
Maximum	1.479	1.668	1.098	9.880
Skewness	1.254	0.887	0.201	2.974
Kurtosis	0.583	-0.556	-1.759	11. 374
Average (mean)	0.430	0.563	0.538	1.447
Variance (S^2)	0.149	0.259	0.133	2.745
Standard Deviation (S)	0.386	0.509	0.365	1.657
Coefficient of Variance (CV)	0.898	0.904	0.679	1.145

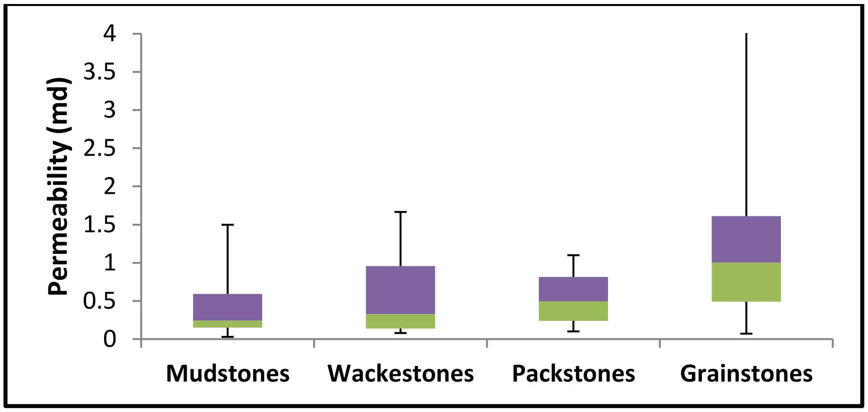

Figure 6.6: Box plot of permeability showing the minimum, first quartile, median, third quartile, and maximum porosity values for each depositional texture.

6.5. Porosity-Permeability Heterogeneities

The coefficient of variance (CV) can be used as a heterogeneity indicator. Homogenous population has CV less than 0.5, CV between 0.5-1.0 indicates heterogeneous population, and CV values above 1.0 indicate greater heterogeneity (Corbet and Jensen, 1992).

The porosity in both the whole data population and within the individual textural group is heterogeneous (Tables 6.1, and 6.2). The permeability shows greater heterogeneity in the whole data set, but within the individual textural group, it becomes heterogeneous. The degree of heterogeneity is higher in grainstone than in any of the other lithofacies (Tables 6.3, and 6.4).

Petrographic studies revealed heterogeneity in the porosity and microporosity, in terms of shape, size and connectivity. In other words, the degrees of leaching/cementation are variable within the individual depositional texture that defines the shape, size and connectivity of the pores (Figures 6.7 and 6.8).

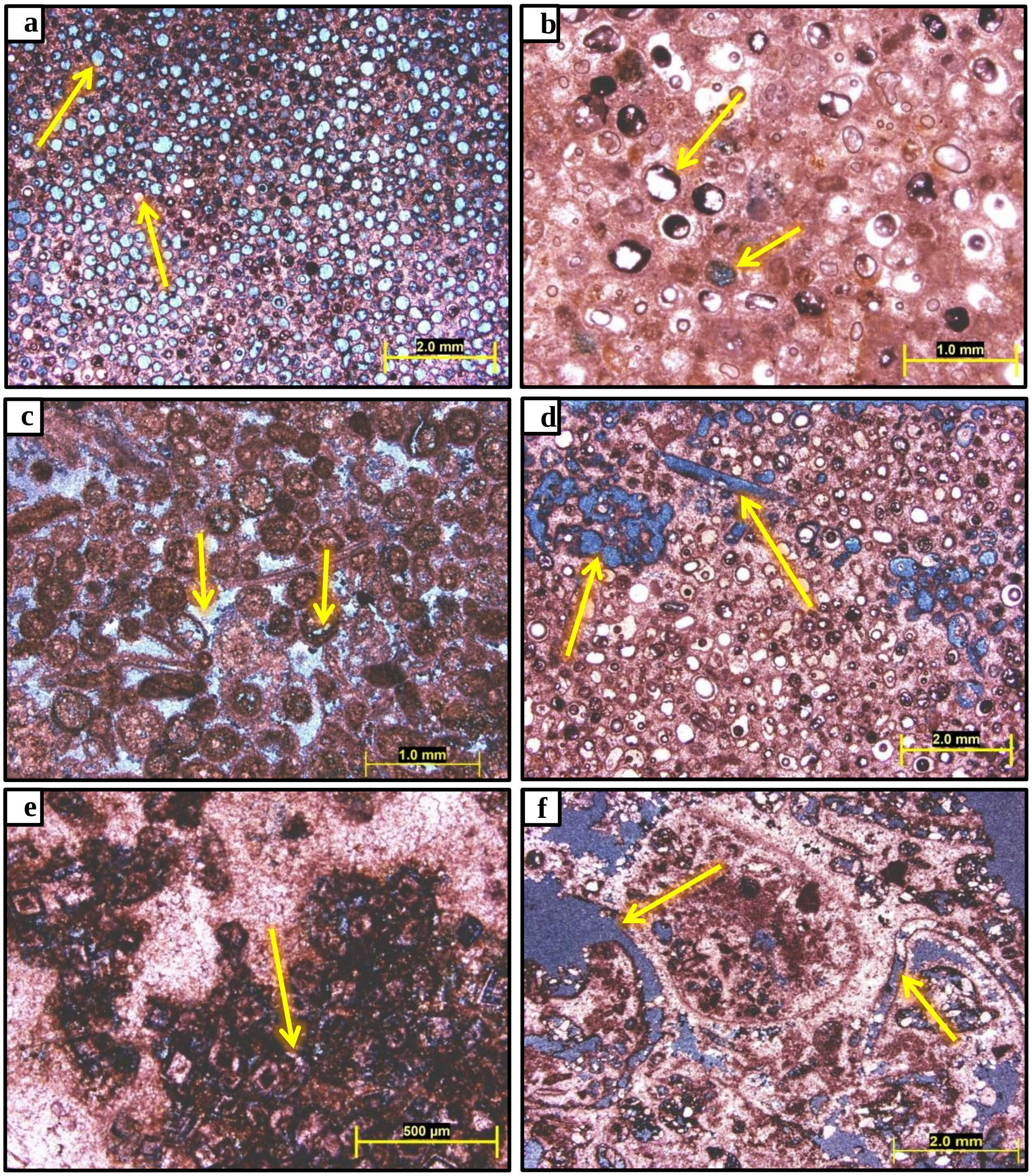

Figure 6.7: The heterogeneity of the pore system in the studied samples (arrows are pointing to the pores that are different in size and geometry).

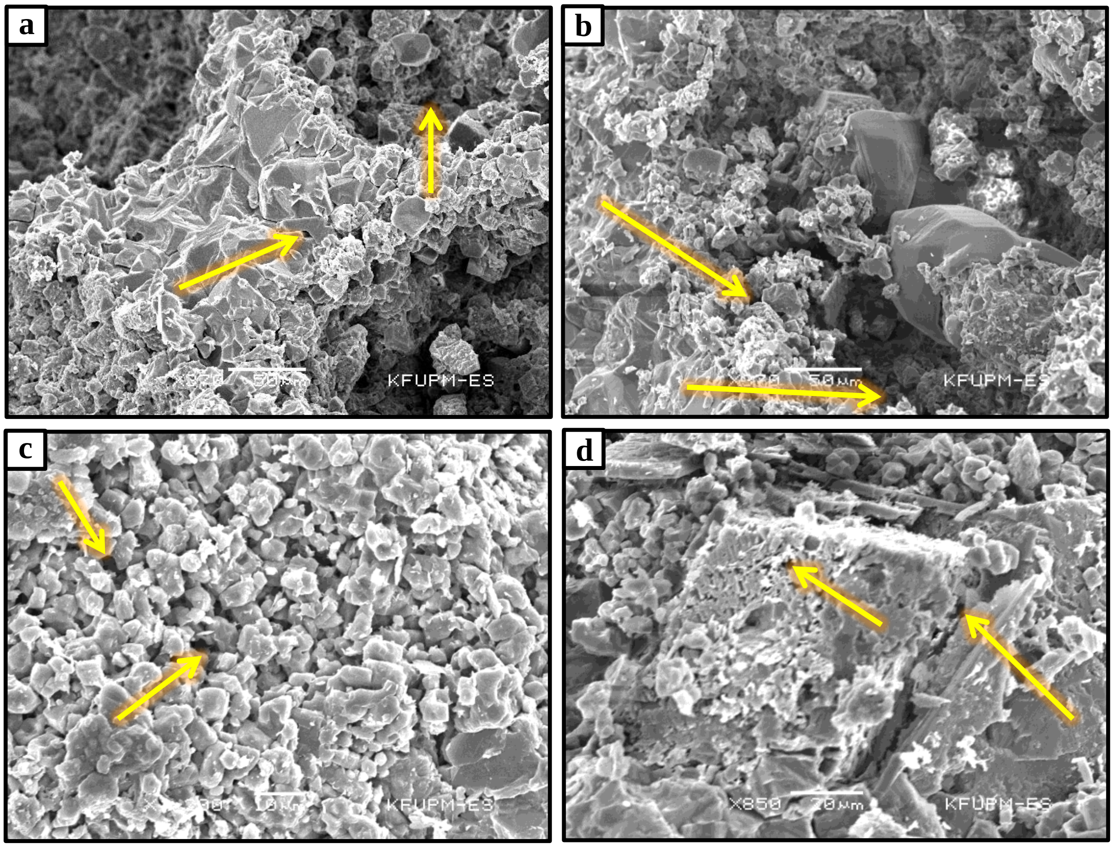

Figure 6.8: SEM images show the variation in presence of microporosity in the studied samples (arrows are pointing to the micropores).

6.6. Discussion

The porosity-permeability cross plot shows poor correlation (R^2 = 0.23) although. The correlations improved significantly when textural groups were considered separately. These correlations indicate:

1- The coefficient of variance (CV) results, which show heterogeneous porosity and very heterogeneous permeability. Thus suggesting indicates that there are a lot of variations in the reservoir quality of the Khartam Member's lithofacies.

2- The porosity-permeability relationships are facies controlled, due to the significant enhancement in the correlation coefficients when the relationships plotted based on the facies group.

The possible factors that produced the heterogeneity in the porosity and permeability are:

1- The variation in the pore sizes (Figure 6.7).

2- The differences in the amount of microporosity within the individual facies (Figures 6.8a, 6.8b. 6.8c and 7.8d).

3- The variation in the degrees of cementation (Figures 6.7b and 6.71d).

Similar study was conducted on Khuff-time equivalent subsurface reservoirs in the Persian Gulf (e.g. Asadi-Eskandar et al., 2013). The porosity-permeability relationship in the study yielded good correlations (R^2 = 0. 66, 0.64, 0.72 and 0.64).

The similarity and the differences between this present study and that of Asadi-Eskandar's et al. (2013) study are:

1- The porosity-permeability relationship in this study was done based on the depositional texture. Whereas, Asadi-Eskandar et al. (2013) performed the porosity-permeability relationship based on the system tracts (HST, LST and TST) for the identified reservoir zones. Therefore, this study is considered to be of higher resolution than the study of Asadi-Eskandar et al. (2013) because this study was done in the scale of bed (depositional texture) within one system tract (HST).

2- This study and Asadi-Eskandar et al. (2013) showed good correlation coefficients. However, the sample number was too large in the study of Asadi-Eskandar et al. (2013) as compare with this study. Large sample number gives statistically good correlation but the amount of risk in permeability prediction from porosity become high.

The box plots for both porosity and permeability (Figures 6.5 and 6.6) did not show any significant separation in the porosity and permeability among the depositional textures indicating the role of diagenesis on the distribution of the reservoir and non-reservoir intervals. This result is consistent with the result of Tavakoli et al. (2011) study on Khuff time equivalent reservoirs in the South Pars gas field, Iran. They plotted the reservoir quality index (RQI) against each depositional texture, and they concluded the porosity and permeability distribution was controlled by diagenesis.

CHAPTER SEVEN

FLOW UNITS RANKING

7.1. Introduction

The information needed for reservoir evaluation exists in different scales of observation, starting from field scale (containing one or more reservoirs), to reservoir scale (one depositional/diagenetic facies or more), to flow unit scale (using porosity and permeability ranges to identify the reservoir intervals), to pore scale (relating the petrophysical characteristics to the pore types/facies associations) (Ahr, 2008). In order to obtain high resolution integration of the outcrop scale, information from outcrop sections, core plugs and thin section scales are essential to evaluate and rank the flow units. Ahr (2008) defined the flow units as rock units within the reservoir scale that allow movement of fluids through effective porosity. Flow units identification, ranking and mapping require good understanding of porosity in three dimension plus connectivity as the fourth dimension (Ahr, 2008).

The main focus in this chapter was to identify and rank the flow units in the Upper Khartam Member outcropping north of Buraydah town, central Saudi Arabia. Integration of field studies, porosity-permeability of the core plugs, and constructing the porosity evolution model was attempted in order to achieve the best ranking of the flow units in the investigated sequence. The flow units ranking depends on the porosity-permeability ranges that are present in porosity-permeability bracket (Figure 7.2). According to this bracket the flow units were divided to nine classes, ranging from one (poor quality) to nine (excellent quality) (layman, 2002 and Poole, 2006).

Porosity evolution model was constructed to show the impact of diagenetic processes in enhancing or reducing the pore quality. Through the porosity evolution model, we can easily estimate the porosity percentages in each stage of diagenesis. This model might also enhance the prediction of the equivalent reservoir rocks that might have been affected by the same diagenetic processes.

7.2. Outcrop Description

The outcrop consists of interbedded beds of grainstone and mudstone facies. Well-sorted oolitic grainstone and cross-bedded skeletal grainstone facies have the highest potentials for being reservoir intervals in the Upper Khartam Member at the outcrop. These flow units are separated from each other by mudstone and wackestone facies which prevent vertical movement of fluids (Figure 7.3). Porosity and permeability data obtained from each bed in three different stratigraphic sections (Figure 7.1) were used to rank each bed in these vertical sections (Figure 7.3) according to the porosity-permeability bracket (Figure 7.2).

7.3. Flow Units Ranking

In order to rank the flow units, a range of porosity and permeability values was related to design porosity-permeability brackets (Figure 7.2). The flow units were ranked into nine classes. In sequential order, they range from a unit showing very poor quality to those characterized by extremely high flow quality. In Figure 7.2, these classes are indicated by violet and blue colors to represent poor quality, and red-orange for excellent reservoir quality units. Porosity was divided into ranges less than 13%, 13.1-25.0 md and greater than 25.1%. Permeability was also divided into less than 1.0 md, 1.1-4.0, and greater than 4.1 md. The subdivisions of porosity and permeability into ranges reflected the observed diversity among the data. A cut-off criterion was chosen to designate flow units 1 to 2 as poor reservoirs and flow units 5 to 9 as good reservoirs. However, none of the units belongs to the flow units 3, 4, and 6 classes.

The ranking of the flow units for vertical stratigraphic sections 1, 2 and 3 that were previously described in chapter four is shown in Figure 7.3. The best quality facies in term of porosity and permeability is the cross-bedded oolitic skeletal grainstones followed by well-sorted oolitic grainstones facies.

The Reservoir Quality Index (RQI) was determined based on the following equation according (Amaefule et al., 1993):

$$RQI = 0.314\sqrt{\frac{k}{\Phi}}$$

Where: RQI: Reservoir quality index, µm; k: Permeability, md; Φ: Porosity, volume fraction.

There is a close relationship between the flow units classes that were delineated based on the porosity-permeability bracket (in Figure 7.2) and the RQI. The units that fall within the poor quality classes (1-4) have RQI value more than 0.09 µm. Whereas the high quality classes (5-9) are characterized by RQI values that are less than 0.08 µm (Figure 7.3).

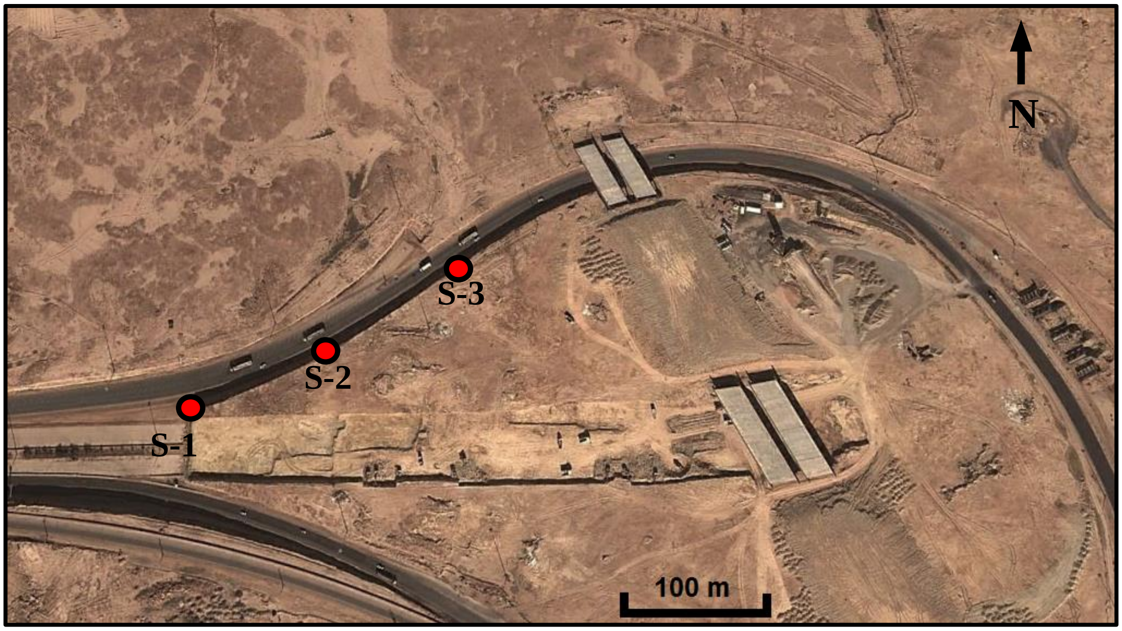

Figure 7.1: Satellite image showing the study area with stratigraphic sections locations, been used to identify and rank the flow units (Google earth, 2013).

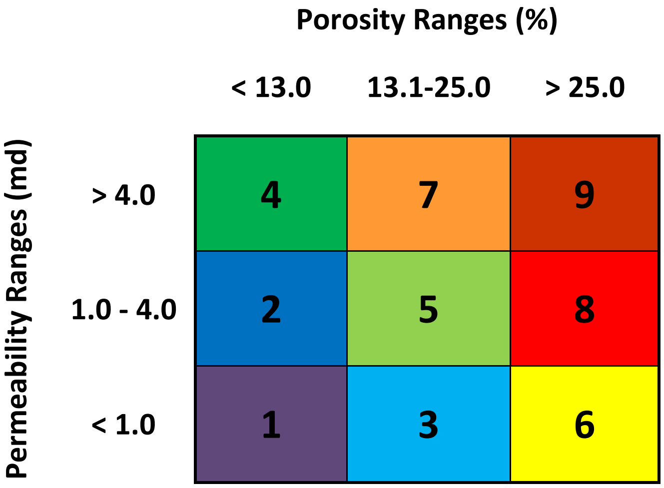

Porosity Ranges (%)

Permeability Ranges (md)	< 13.0	13.1-25.0	> 25.0
> 4.0	4	7	9
1.0 - 4.0	2	5	8
< 1.0	1	3	6

Figure 7.2: Definition of flow units (porosity-permeability brackets).

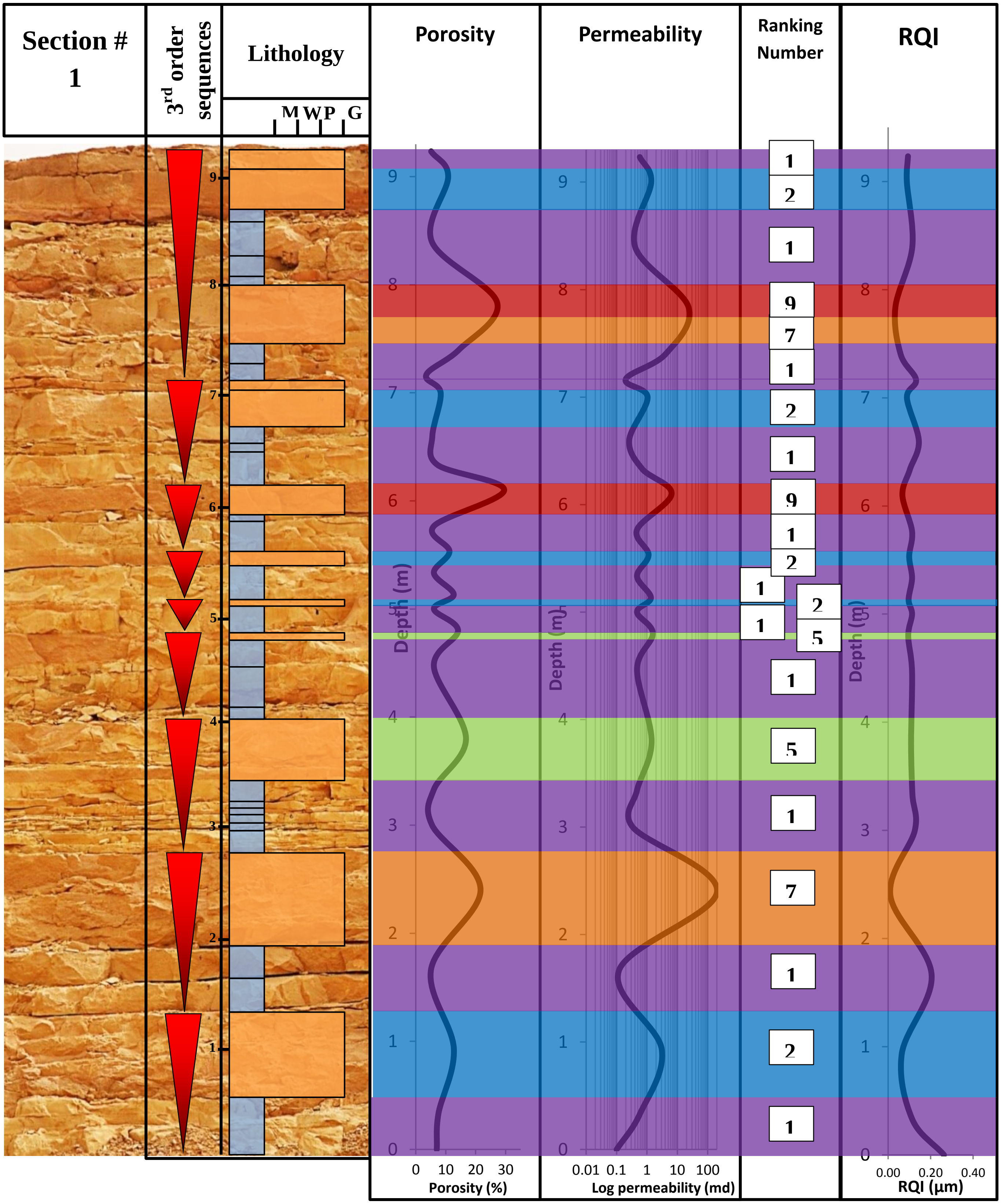

Figure 7.3: vertical outcrop sections 1, 2 and 3 with their outcrop photo, porosity, permeability, flow units ranking numbers, RQI and color code.

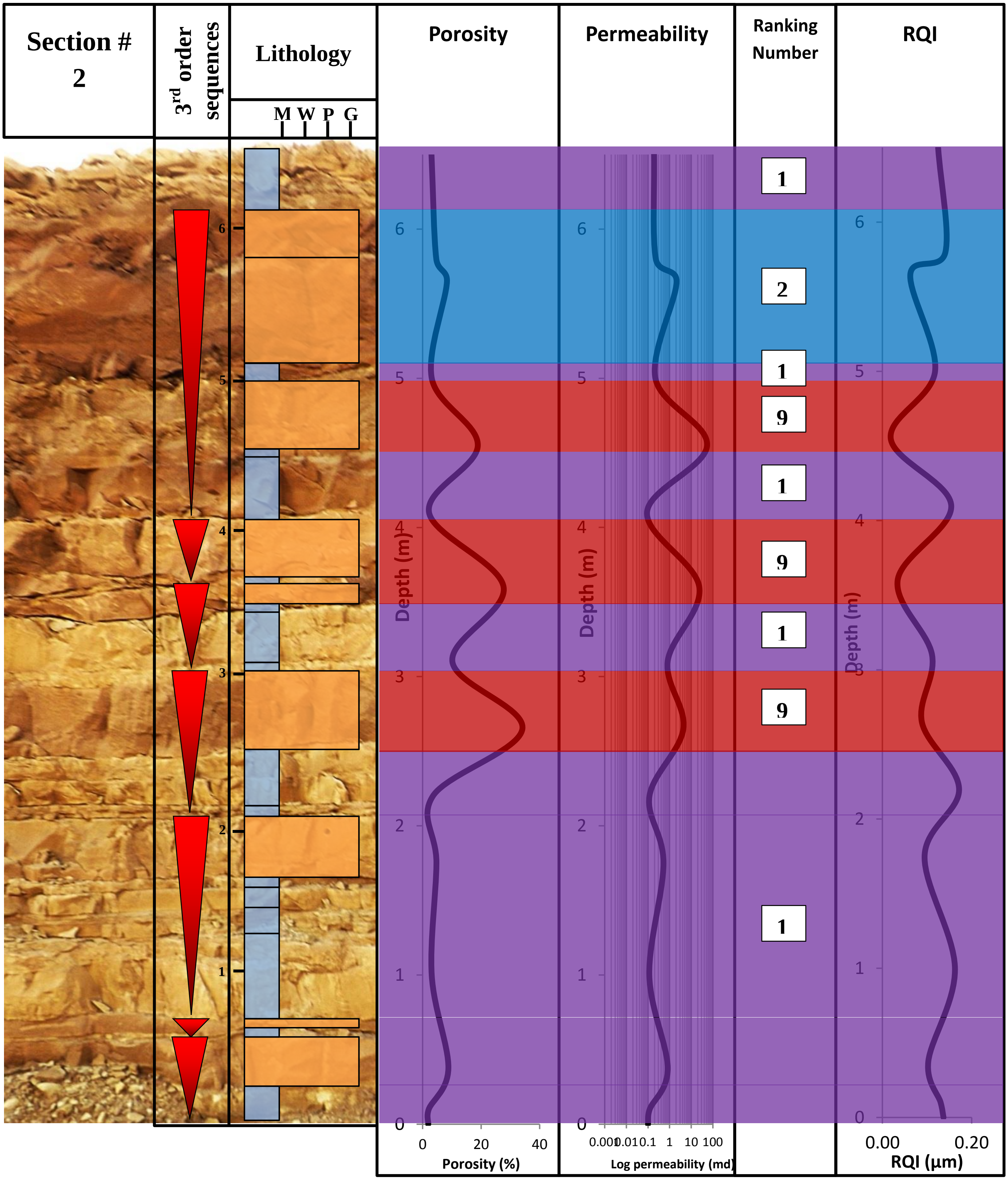

Figure 7.3: (Continued).

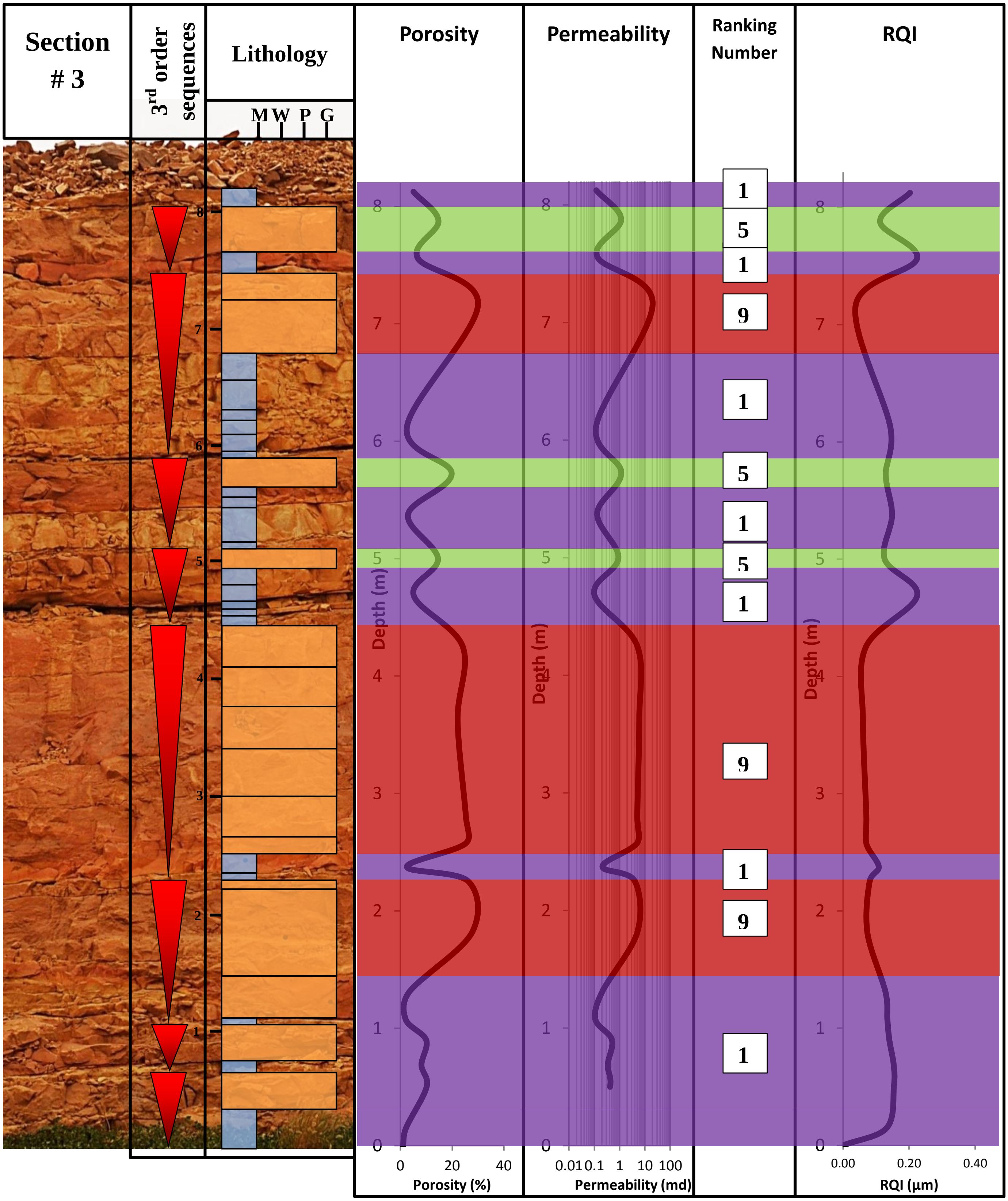

Figure 7.3: (Continued).

7.4. Porosity Evolution under Diagenetic Framework

The observations from thin sections reveal that the Upper Khartam Member in the outcrop has gone through multistage diagenetic alterations. Eodiagenesis (early), mesodiagenesis (middle) and telogenesis (late) have all affected the exposed strata of the investigated Upper Khartam Member.

Understanding the evolution of porosity is important especially when studying the equivalent subsurface strata. In addition, some strata are located in the shadow of the diagenetic solutions or for some reasons the diagenetic solutions could not penetrate them, and accordingly these beds remain in earlier stage of diagenesis unlike other beds. Thus, these phenomena have to be addressed.

Six stages of diagenesis were identified from the thin section studies. The first diagenetic stage was the direct precipitation of the oolitic grains without any significant compaction. This was followed by precipitation of micrite envelopes, partial dissolution, marine cementation, partial/total dissolution of oolitic grains in association with partial/total cementation in the intergranular space, and finally partial/total cementation of the moldic porosity (Figure 7.5). The well sorted oolitic grainstone facies was chosen to illustrate the paragenesis of diagenetic processes on the investigated Upper Khartam Member. These diagenetic events are briefly discussed as follows.

1- Precipitation of the oolitic grains

In the well-sorted oolitic grainstones facies, the ooids are the main and only grain component. Ooids develop in shallow marine (less than 10 m), warm, and wave agitated water. The marine waves keep the ooids moving which enable accretion to occur on all sides. Ooids are well rounded spherical grains with nuclei in their centers surrounded by tiny concentric layers made of calcium carbonate. Oolitic grains are less than 2 mm in diameter. If their grains size exceeds 2 mm they are called pisoids.

In Figure 7.5a, the ooids are shown to have been precipitated without any significant compaction in the shallow warm water. This type is considered the depositional form of oolitic grainstone without any diagenetic alteration. The porosity at this stage is very high.

2- The micrite envelopes

Micrite envelopes are tiny cements that develop around the oolitic/skeletal grains within the shallow marine environment (early burial alteration). These envelopes play a main role in preserving the original fabric that might be lost during later diagenesis. In this phase, micrite envelopes are the only trace of the original sedimentary texture as shown in stage (7), Figure 7.5g (calcite in white color) and Figure 7.5h (calcite stained red) (Scholle and Ulmer-Scholle, 2003). In the examined samples, micrite envelopes have no significant effect on the porosity. However, they have positive effect in preserving the original texture framework and preventing moldic porosity from collapsing during meteoric diagenesis (grain dissolution).

Micrite envelopes are originally composed of high-Mg calcite. In most cases, micrite envelopes have thin cover or layers of phreatic calcite cement in their interior and exterior surfaces (intergranular and intragranular pores) (Scholle and Ulmer-Scholle, 2003).

3- Partial dissolution

The oolitic grains usually contain tiny layers or the nuclei of high Mg calcite that can be easily dissolved to form intragranular porosity. In this stage, the dissolved layers are a result of early diagenesis (Eodiagenesis). However, some materials which can withstand this stage are easily dissolved during the mesodiagenesis as stages 5, 6 and 7. At this stage, the porosity is enhanced by additional intragranular porosity (Figure 7.5c).

4- Marine cementation

Marine cementation is composed of high-Mg calcite which is developed in warm, shallow, slightly hypersaline waters in tropical shelf, lagoonal or coastal areas. Marine cementation is characterized by the high ratio of the length and width (longer and thinner) as compared with the crystals that are found in typical high-Mg calcite cements.

Marine cementation in this case grows around the grains in the intergranular porosity and within the grains in the intragranular porosity (Figure 7.5d). This cementation is not resistant to meteoric diagenesis and is usually gets dolomitized or completely dissolved. In this phase, there is no any trace of the marine cementation. At this stage, the porosity leading significantly reduction in permeability and closure of the pore throat that lies between intergranular pores.

Usually marine cementation contains micro-dolomite inclusions or high concentrations of Mg to prove an original high-Mg calcite composition. In order to detect these inclusions Scanning Electron Microscopy (SEM) or microprobe analysis is required to be carried out.

5 & 6- Partial dissolution of ooids and partial cementation in the intergranular space

There are called stages of meteoric diagenesis (mesodiagenesis). In the meteoric diagenesis, dissolution of the unstable grains and precipitation of the meteoric cement in the primary intergranular space are both simultaneously active. The dissolved materials become the supplying materials for the cementation process. This stage is considered as an intermediate stage of grain destruction in which numerous large and small intragranular pores are initiated. Figure 7.4 shows the three different stages of selective leaching of oolitic thin layers and cementation of the intergranular space (e.g., Scholle and Ulmer-Scholle, 2003). Oolitic thin layers (coating materials) contain different materials to allow differential leaching of the layers.

In case of well-sorted oolitic grainstone facies, the oolitic grains are dissolved to form intragranular or moldic porosity at the same time of the precipitation of the blocky calcite cement (meteoric cement). Blocky calcite cement is characterized by coarsely-crystalline and equant crystals (similar length and width). The stage of dissolution and cementation are divided into two stages (stages 5 & 6) to show both the partial dissolution/cementation and semi to full dissolution/cementation stages. In these stages (5 & 6), porosity enhancement and reduction took place at the same time. The cement (marked by white color in Figures 7.5e and 7.5f) reduced the intergranular pores, while dissolution of oolitic grains enhances the intragranular/moldic porosity (porosity marked by blue color epoxy in Figures 7.5e and 7.5f).

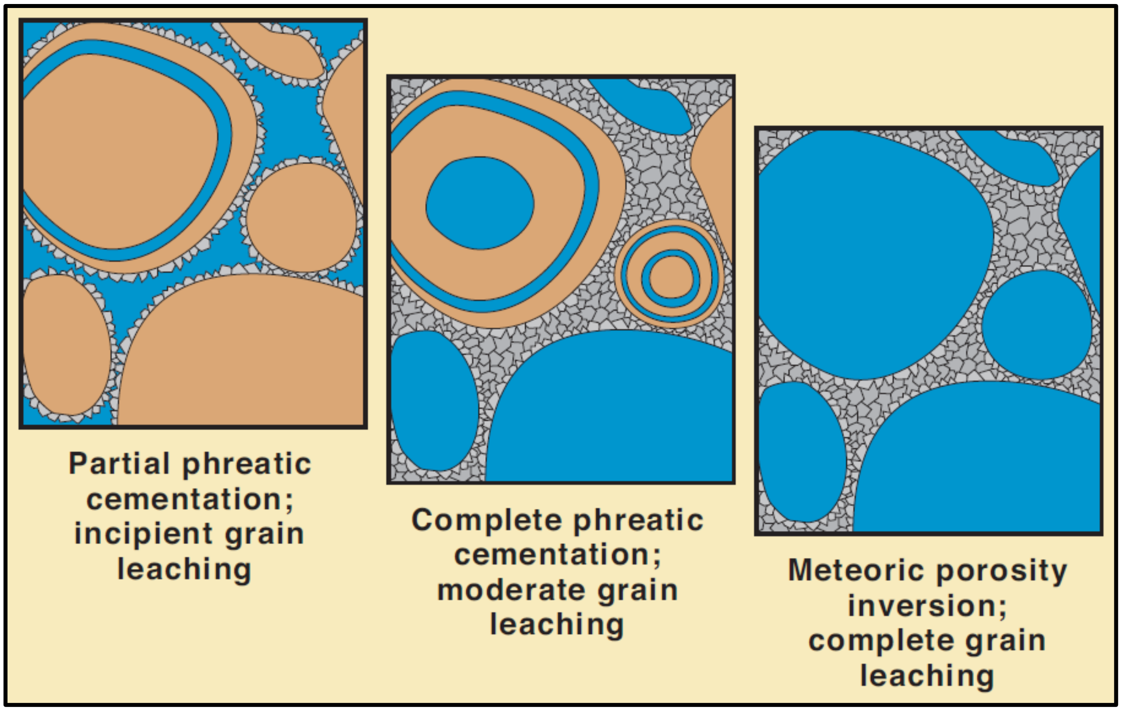

Figure 7.4: Stages of the meteoric diagenesis (Scholle and Ulmer-Scholle, 2003).

7- Complete molds

This stage shows complete development of moldic porosity (secondary porosity) through dissolution of oolitic grains. Primary intergranular porosity is completely filled by blocky calcite cement (meteoric cementation) as a result of vadose (telogenesis). Although visual porosity (moldic pores) in this stage is still high, the permeability was mainly reduced due to the poor connection of the moldic pores (the connection is mainly through intercrystalline micropores or at the molds' point contacts) (e.g., Scholle and Ulmer-Scholle, 2003).

This stage represents a complete inversion of the original fabric and the pore system; the grains become pores and the intergranular space filled with calcite cements (calcite indicated by white color in Figure 7.5g, and calcite stained red in Figure 7.5h). If this process continues with further supply of calcite rich solutions from external supply, the moldic and vuggy porosities will be filled with calcite cement (see stage 8 & 9).

8- Partial cementation within the oolitic molds

After total inversion of the porosity system from primary to secondary porosity, a further cementation process might proceed due to continuous influx of the solutions that can enhance the cementation process within the pore space (moldic porosity in this case).

In the well-sorted oolitic grainstone facies, moldic porosity was reduced by further calcite cementation (calcite indicated by white color in Figure 7.5i, and calcite stained red in Figure 7.5j). Continuous supply of the calcite-rich solution from external supplier leads to partial cementation of the pores and then totally if the supply of the cementing material continues. This stage causes a major reduction of the total porosity as the process of cementation proceeds.

9- Complete cementation of the inter & intragranular porosity

This stage was reached when the calcite-saturated solutions continue to flow into the formation to precipitate the calcite cement within the moldic porosity (calcite indicated by white color and stained red in Figures 7.5k and 7.5l, respectively). In the well-sorted oolitic grainstone facies, some of the pores are completely filled with calcite cement, however, most of the molds are partially cemented. The porosity at this stage has been reduced to the minimum and microporosity (>10 microns in diameter (Cantrell and Hagerty, 1999) becomes the dominant pore type.

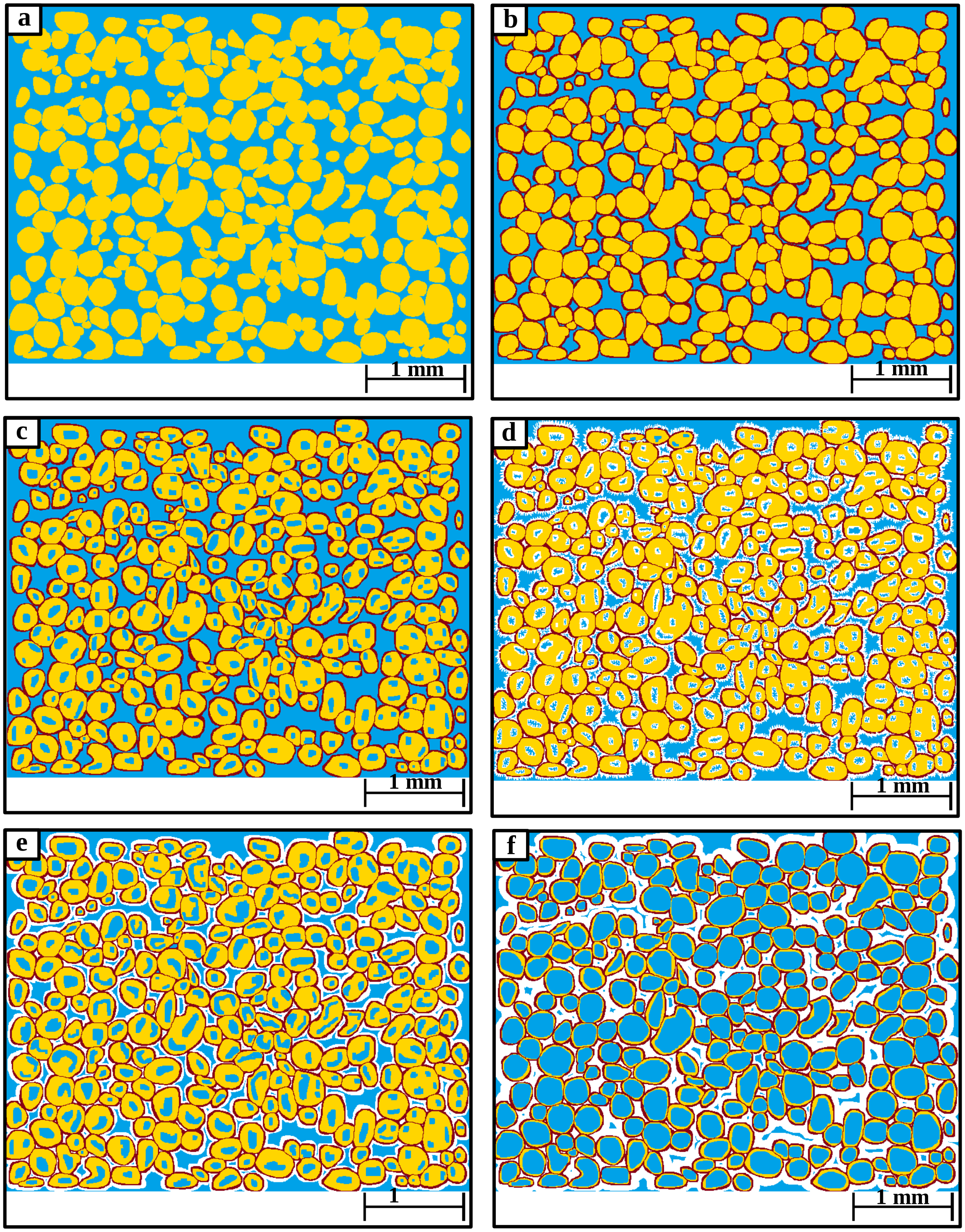

Figure 7.5: porosity evolution models of the Upper Khartam Member. Porosity is shown in blue, calcite in white and red in stained samples, and ooids in yellow.

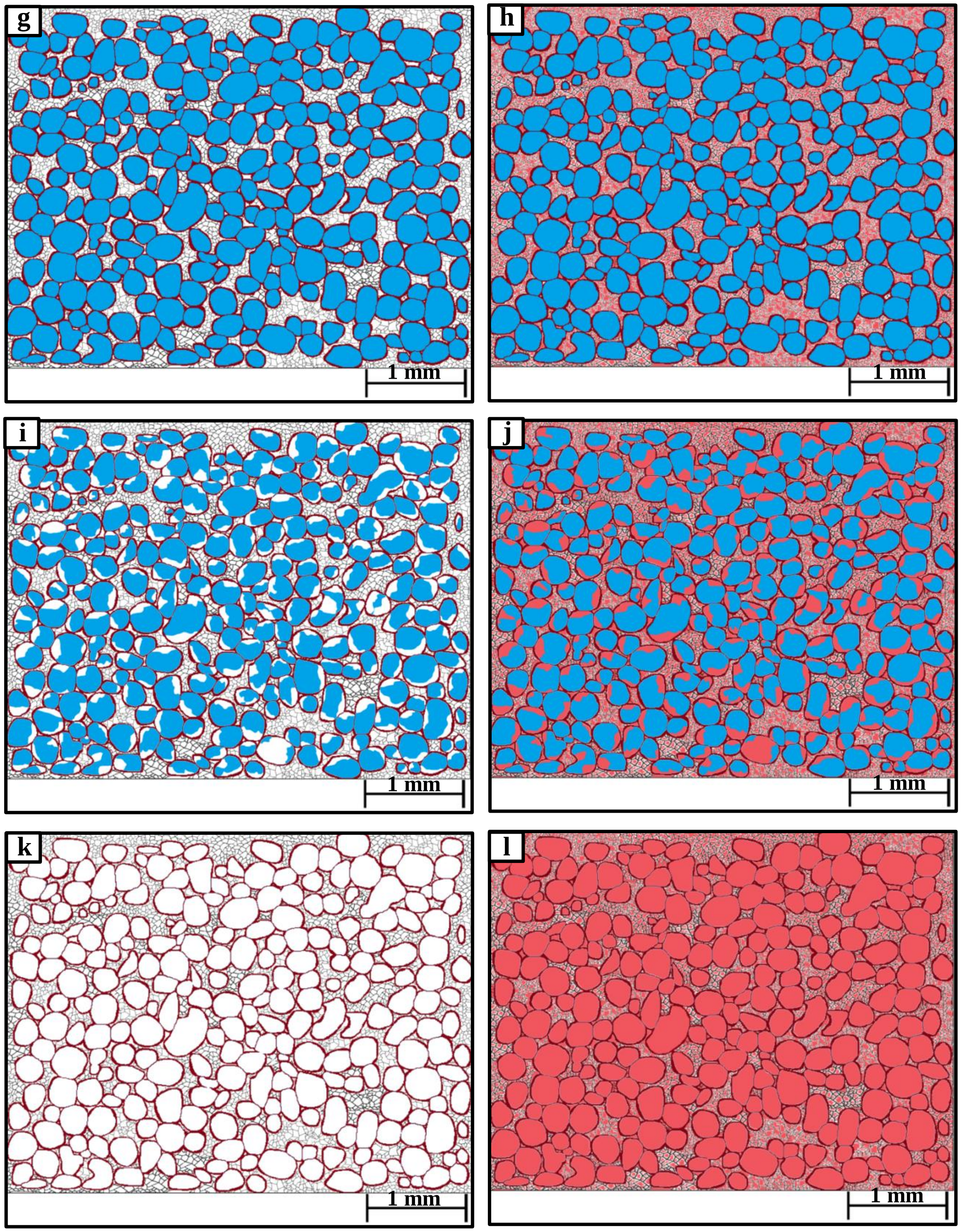

Figure 7.5: (Continued).

7.5. Discussion

The mudstone/wackestone facies have no sufficient porosity and permeability to be considered as a flow unit, and instead it serves as porosity and permeability barriers, which fall into the 1 and 2 ranking classes. Some of the packstone/grainstone beds are also considered permeability barriers due to calcite cementation. From this study the main factors that control the intra reservoir barriers (IRBs) are the depositional texture and the diagenetic cementation. Similar finding was documented by Rahimpour-Bonab et al. (2014) in the Khuff equivalent successions in the subsurface, Central Persian Gulf, Iran. With the lithology and the calcite cementation, Rahimpour-Bonab et al. (2014) including anhydrite cementation, micrite recrystallization and stylolitization as factors that control the distribution of the intra reservoir barriers (IRBs).

Both the well-sorted oolitic grainstone and cross-bedded oolitic skeletal grainstone facies have the highest ranking numbers ranged from 5 to 9. However, a few intervals belonging to these facies fall in the lowest quality ranking classes (1-2). This means that the majority of the flow units in the Upper Khartam Member are facies controlled. However, most of these facies have been diagenetically altered. This idea is supported by high variation in the porosity and permeability within the dominant facies. Intervals with the lowest quality ranking (1 and 2) in the grainstone facies correspond to the intervals that are strongly affected by extensive cementation and pores filling. Whereas, the highest quality ranking intervals (5-9) correspond to the intervals in which cementation is followed by extensive leaching.

Poole (2007) found similar flow units ranking in the Grayson field, in Columbia County. In her study, she classify the flow units based on the following permeability ranges 10-

210, 210-410 and < 410 md. In the present study, permeability ranges are >1, 1-4, <4 md to rank the flow units. Low permeability is accepted in the Khuff gas reservoir, while the oil reservoir required high permeability such as the Smackover reservoir (Poole, 2007).

The ranking of the flow units was made in three vertical sections. The vertical sections 1, 2 and 3 respectively, represent the bottom, middle and top of the composite section of the studied part of the Upper Khartam Member.

The flow units appear as small isolated intervals in section #1, at the bottom of the composite section, present a highly cemented grainstone. Section #3 shows thick stacked flow units, which are located at the top of the composite section. These units represent less cemented-highly leached grainstone. Therefore, the studied intervals of the Upper Khartam Member show good quality reservoir in the upper part of the composite section, while the lower part is considered as possessing the least reservoir quality (Figure 8.2).

In most cases, the flow units follow the lithological boundaries in the vertical sections, indicating that the distribution of flow units is mainly controlled facies distribution pattern (depositional). However, some grainy beds which are highly cemented are characterized as poor flow units‟ classes suggesting that diagenetic cementation also played a second role in the distribution of the flow units.

CHAPTER NINE

CONCLUSION

The main findings of this research are summarized as follows:

Porosity (vuggy and moldic porosity types) development in the Upper Khartam outcrop samples was mainly due to diagenetic alteration of the depositional textures.

The eight distinctive pore types identified in this study were linked with their geometrical shapes. These porosity types were in turn, integrated with the facies to predict rock and petrophysical properties.

The correlation coefficients of the porosity and permeability improved significantly when the data was plotted based on the different depositional textures. Among the four textural groups, mudstone and wackestone facies show the highest correlation coefficient (0.6 and 0.8 respectively), while packstone and grainstone show the lowest (0.4 for both).

The coefficient of variance of the data sets revealed heterogeneous nature of the porosity in the all lithofacies combined data populations and in the each of the individual facies. The coefficient of variance of the permeability data indicated very heterogeneous permeability for the combined lithofacies data population and for the grainstone facies. The coefficient of variance show heterogeneous permeability in the mudstone, wackestone and packstone facies. The possible reasons for both reduction of the correlation coefficient and the variety degrees of heterogeneity of the porosity and permeability populations are:

1- The mixture of different types/sizes of porosity especially the secondary porosity (moldic and vuggy porosities).
2- The variability in sizes and shapes of the microporosity.

The cross-bedded oolitic skeletal grainstones facies and well-sorted oolitic grainstone facies are ranked the highest flow units in the Khartam Member. Furthermore, the presence of moldic pores (oomoldic or skelmoldic) larger than 40,000 μm^2 combined with large vuggy porosity provide for optimum porosity and permeability.

The Upper Khartam Member mostly consists of poor flow unit intervals at the basla section and excellently ranked intervals in the upper portion of the studied outcrop. The flow units' distribution pattern follows the lithological boundaries in most cases, suggesting that flow units development and distribution in the investigated outcrop are principally controlled by depositional facies. The grainstone intervals form excellent flow units while the muddy lithofacies are classified as poor flow units. The identification of poor flow unit in a few grainstone intervals is interpreted as an indication that in addition to facies type, diagenesis (e.g., cementation) also controlled flow unit distribution in the studied outcrop.

Close relationship was determined between the flow units classes based on the porosity-permeability bracket and the RQI. The units that fall in poor quality classes (1-4) have RQI value more than 0.09 µm. Whereas, less than 0.08 µm are distinguished for the high quality classes (5-9).

References

Aigner, T. and Pöppelreiter, M. (2012). The Khuff outcrop project in the Oman Mountains: Framework and research approach. In The Permo–Triassic Sequence of the Arabian Plate, Abstracts of the EAGE's Third Arabian Plate Geology Workshop, Kuwait. Abstract, *GeoArabia*, *17*(1), 185-189.

Ahr, W. M. (2008). *Geology of Carbonate Reservoirs: The Identification, Description and Characterization of Hydrocarbon Reservoirs in Carbonate Rocks*. Wiley-Interscience.

Ahr, W. M., Allen, D., Boyd, A., Bachman, H. N., Smithson, T., Clerke, E. A., ... & Ramamoorthy, R. (2005). Confronting the carbonate conundrum. *Oilfield Review*, *17*(1), 18-29.

Al-Aswad, A. A. (1997). Stratigraphy, Sedimentary Environment and Depositional Evolution of the Khuff Formation in South-Central Saudi Arabia. *Journal of Petroleum Geology*, *20*(3), 307-326.

Al-Belushi, J.D., Glennie, K.W., & Williams, B.P.J. (1996). Permo-Carboniferous glaciogenic Al Khlata Formation, Oman: A new hypothesis for origin of its glaciation. *GeoArabia*, *1*(3), 389-404.

Al-Husseini, M.I. (2004). Pre-Unayzah unconformity, Saudi Arabia. In, M.I. Al-Husseini (Ed.), Carboniferous, Permian and Early Triassic Arabian Stratigraphy. *GeoArabia Special Publication* 3, 15-59.

Al-Husseini, M.I. (2006). Permian Arabian tectono-stratigraphy chart. *GeoArabia*, *11*(4), 95- 102.

Al-Jallal. I. A. (1989). *Depositional environments, diagenesis and reservoir characteristics of the late Permian Khuff Formation in eastern Saudi Arabia*: Ph. D. Thesis, University of London, (unpublished).

Al-Jallal, I. A. (1995). The Khuff Formation: its regional reservoir potential in Saudi Arabia and other Gulf countries; depositional and stratigraphic approach. In *Middle East Petroleum Geosciences Conference, GEO* (Vol. 94, pp. 103-119).

Al-Sharhan, A. S., and Narin, A. E. M. (2003). Sedimentary Basins and Petroleum Geology of the Middle East: *Elsevier Pub*., Chap. 5-6, pp. 141-178.

Alsharhan, A.S. (2006). Sedimentological character and hydrocarbon parameters of the middle Permian to Early Triassic Khuff Formation, United Arab Emirates. *GeoArabia 11*, 121–158.

Amaefule, J. O., Altunbay, M., Tiab, D., Kersey, D. G., & Keelan, D. K. (1993, January). Enhanced reservoir description: using core and log data to identify hydraulic (flow) units and predict permeability in uncored intervals/wells. In *SPE Annual Technical Conference and Exhibition*. Society of Petroleum Engineers.

Anselmetti, F. S., Luthi, S., and Eberli, G. P. (1998). Quantitative characterization of carbonate pore systems by digital image analysis. *AAPG bulletin*, *82*, 1815-1836.

Archie, G. E. (1952). Classification of carbonate reservoir rocks and petrophysical considerations. *AAPG Bulletin*, *36*(2), 278-298.

Asadi-Eskandar, A., Rahimpour-Bonab, H., Hejri, S., Afsari, K., & Mardani, A. (2013). Consistent geological-simulation modeling in carbonate reservoirs, a case study from the Khuff Formation, Persian Gulf. *Journal of Petroleum Science and Engineering*, *109*, 260-279.

Baud, A., Richoz S., & Pruss S. (2007). The Lower Triassic anachronistic carbonate facies in space and time. *Global and Planetary Change*, *55*(1-3), 81-89.

Baud, A., and Richoz, S. (2013). Permian–Triassic Transition and the Saiq/Mahil Boundary in the Oman Mountains: Proposed correction for lithostratigraphic nomenclature. *GeoArabia*, *18*(3), 87-98.

Béchennec, F., Le Métour, J., Rabu, D., Bourdillon-de-Grissac, C., De Wever, P., Beurrier, M. T., & Villey, M. (1990). The Hawasina Nappes: stratigraphy, palaeogeography and structural evolution of a fragment of the south-Tethyan passive continental margin. *Geological Society, London, Special Publications*, *49*(1), 213-223.

Béchennec, F., Roger, J., Le Métour, J., & Wyns, R. (1992). Explanatory notes to the Geological map of Seeb. Sheet NF40-03. *Muscat, Oman Ministry of Petroleum and Minerals*, 104.

Beydoun, Z. R. (1993). Evolution of the northeastern Arabian plate margin and shelf: hydrocarbon habitat and conceptual future potential. *Oil & Gas Science and Technology*, *48*(4), 311-345.

Cantrell, D. L., & Hagerty, R. M. (1999). Microporosity in Arab Formation carbonates, Saudi Arabia. *GeoArabia*, *4*(2), 129-154.

Choquette, P. W., & Pray, L. C. (1970). Geologic nomenclature and classification of porosity in sedimentary carbonates. *AAPG bulletin*, *54*(2), 207-250.

Cogné, J.P. (2003). PaleoMac: A MacintoshTM application for treating paleomagnetic data and making plate reconstructions. *Geochemistry, Geophysics, and Geosystems*, *4* (1), 1007.

Corbet, P., and Jensen, J. L. (1992). Estimating the mean permeability: how many measurements do you need?. *First Break*, *10*(3), 89–94.

Coy, G.A. (1997). *Dolomitisation of the Akhdar Group: The Arabian Platform of Oman*: Ph. D. Thesis, University of Cambridge, 164, (Unpublished).

Dasgupta, S. N., Hong, M. R., & Al-Jallal, I. A. (2002). Accurate reservoir characterization to reduce drilling risk in Khuff-C carbonate, Ghawar field, Saudi Arabia. *GEOARABIA*, *7*, 81-100.

Delfour, J., R. Dhellemmes, P., Elsass, D., Vaslet, J.-M., Brosse, Y.-M., Le Nindre and Dottin O. (1982). Explanatory notes to the geologic map of the Ad Dawadimi Quadrangle, Kingdom of Saudi Arabia. *Geoscience Map GM-60C*, scale 1:250,000, sheet 24G. *Deputy Ministry for Mineral Resources, Ministry of Petroleum and Mineral Resources, Kingdom of Saudi Arabia*. 36 p.

Dunham, R.J. (1962). Classification of carbonate rocks according to depositional texture. *Memoir 1 of American Association of Petroleum Geologists*, 108-121.

Ehrlich, R., Kennedy, S. K., Crabtree, S. J., and Cannon R. L. (1984). Petrographic image analysis; I, Analysis of reservoir pore complexes. *Journal of Sedimentary Petrology*, *54*(4), 1365-1378.

Ehrlich, R., Crabtree, S.J., Horkowitz, K.O., and Horkowitz J.P. (1991a). Petrography and reservoir petrophysics I: Objective classification of reservoir porosity. *AAPG Bulletin*, *75*(10), 1547-1562.

Ehrlich, R., Etris, E.L., Brumfield, D., Yuan, L.P., and Crabtree S.J. (1991b). Petrography and reservoir petrophysics III: Physical models for permeability and formation factor. *AAPG Bulletin*, *75*, 1579-1592.

Eltom, H., Abdullatif, O.M., Babalola, O.L., Bashari, M A., Yassin, M., and Osman M.S. (*2014*). Characterization of the Late Permian Early Triassic Upper Khuff Formation: Outcrop Study-Implications for Hydrocarbon Reservoirs. *GeoArabia*.(In Press)

Garzanti, E., & Sciunnach, D. (1997). Early Carboniferous onset of Gondwanian glaciation and Neo-Tethyan rifting in South Tibet. *Earth and Planetary Science Letters*, *148*(1), 359-365.

Glennie, K.W., Boeuf, M.G.A., Hughes-Clarke, M.W., Moody-Stuart, M., Pilaar, W.F.H. & Reinhardt, B.M. (1973). Late Cretaceous nappes in Oman Mountains and their geological evolution. *AAPG Bulletin*, *57*, 5-27.

Glennie, K.W., Boeuf, M.G., Hughes-Clarke, M.H.W., Moody-Stuart, M., Pilaar, W.F., & Reinhardt, B.M. (1974). Geology of the Oman Mountains. *Verhandelingen van het Koninklijke Nederlands Geologisch Mijnbouwkundig Genootschap*, (31), 423.

Glennie, K.W. (2000). Cretaceous tectonic evolution of Arabia‟s Eastern Plate margine: A tale of two oceans. *SEPM Spec. Publ.* 69, 9-20.

Goldstein, J., & Yakowitz, H. (1975). *Practical scanning electron microscopy*: New York, Plenum Press, 582p.

Google Earth 7.1. 2013. *Altarafiya, north Buraydah town, central Saudi Arabia 26°25'37.26"N, 44° 0'19.20"E.* 45° Imagery. <http://www.google.com/earth/index.html> [Viewed 1 December 2013].

Humbolt, A. (2008). *Genetic Pore Typing as a Means of Characterizing Reservoir Flow Units: San Andres, Sunflower Field, Terry Country, Texas*: *M.S. Thesis, Texas A&M University, College Station, Texas*, 187 p.

Koehrer, B., Aigner, T., Forke, H., & Pöppelreiter, M. (2012). Middle to Upper Khuff (Sequences KS1 to KS4) outcrop-equivalents in the Oman Mountains: Grainstone architecture on a subregional scale. *GeoArabia*, *17*(4), 59-104.

Kershaw, S., Li, Y., Crasquin-Soleau, S., Feng, Q., Mou, X., Collin, P-Y., Reynolds, A., & Guo, L. (2007). Earliest Triassic microbialites in the South China block and other areas: controls on their growth and distribution. *Facies*, 53, 409-425.

Konert, G., Afifi, A.M., Al-Hajri, S.A., de Groot, K., Al Naim, A.A., and Droste, H.J. (2001). Paleozoic stratigraphy and hydrocarbon habitat of the Arabian Plate. *AAPG Memoir*, 74(Chapter 24), 483-515.

Layman, M. J., and Ahr, W. M. (2004). Porosity characterization utilizing petrographic image analysis: implications for rapid identification and ranking of reservoir flow units, Happy Spraberry Field, Garza County, Texas, extended abstract, *AAPG*, *88*(13) (supplement)

Layman, J. M., and Ahr, W. M. (2002). Porosity characterization utilizing petrographic image analysis: Implications for rapid identification and ranking of reservoir flow units, Happy Spraberry Field, Garza County, Texas. *Publications-West Texas Geological Society*, 107-114.

Layman, J. M. (2002). *Porosity characterization utilizing petrographic image analysis: Implications for identifying and ranking reservoir flow units, Happy Spraberry field, Garza County, Texas: M.S. thesis, Texas A&M University, College Station, Texas*, 114 p.

Le Métour, J. (1987). *Géologie de l'autochtone des Montagnes d'Oman: La fenêtre du Saih Hatat*: Ph. D. Thesis, University Pierre and Marie Curie, Paris VI, France, 425 p. (Document Bureau de Recherches Géologiques et Minières no. 129, Orléans, France, 1988, 430.

Le Nindre Y.-M., Vaslet, D., Le Métour, J., Bertrand, J., and Halawani M. (2002). Quantitative subsidence analysis of the Arabian Platform from Permian to Paleogene outcrops. *Sedimentary Geology*, 156(1), 263-285.

Le Nindre, Y.-M., Manivit, J., and Vaslet, D. (1990a). Histoire géologique de la bordure occidentale de la plate-forme Arabe, v. 3: Le Permo-Trias d‟Arabie centrale. *Bureau de Recherches Géologiques et Minières*, *3*(193), 262.

Le Nindre, Y.-M., Manivit J., and Vaslet, D. (1990b). Histoire géologique de la bordure occidentale de la plate-forme Arabe, v. 2: Géodynamique et paléogéographie de la plate-forme Arabe du Permien au Jurassique. *Bureau de Recherches Géologiques et Minières*, 2(192), 278.

Luo, P., and Machel, H. G. (1995). Pore size and pore throat types in a heterogeneous dolostone reservoir, Devonian Grosmont Formation, Western Canada sedimentary basin. *AAPG bulletin*, *79*(11), 1698-1719.

Maurer, F., Martini, R., Rettori, R., Hillgärtner, H., & Cirilli, S. (2009). The geology of Khuff outcrop analogues in the Musandam Peninsula, United Arab Emirates and Oman. *GeoArabia*, *14*(3), 125-158.

Poole, K. R. (2006). *Construction of a diagenetic history and identification with quality ranking of reservoir flow units: Grayson field, Columbia County, Arkansas: M.S. thesis, Texas A&M University, College Station, Texas*.

Powers, R.W. (1968). International stratigraphic lexicon; volume 3, Asia, part 10 b 1, Saudi Arabia Lexique stratigraphique international; volume III, Asie, fascicule 10 b 1, Arabie Saoudite. 177.

Powers, R. W., Ramirez, L. F., Redmond, C. D., and Elberg, E. L. (1966). Geology of the Arabian Gulf, sedimentary geology of Saudi Arabia: U.S.G.S. Prof. Paper 560 D, U.S. Govt. Printing Office, Washington D.C., USA, 147 p.

Powers, R. W. (1962). Arabian Upper Jurassic carbonate reservoir rocks. *Classification of carbonate rocks: AAPG Memoir*, *1*, 122-192.

Ppelreiter, M. (2014). *Permo-triassic sequence of the Arabian Plate*. Houten, The Netherlands: EAGE Publications.

Rabu, D., Béchennec, F., Beurrier, M., & Hutin, G. (1986). Explanatory notes to the geological map of the Nakhl Quadrangle, Sultanate of Oman. Geoscience map, scale 1:100,000, sheet NF 40-3E. *Ministry of Petroleum and Minerals, Directorate General of Minerals, Sultanate of Oman*. 42.

Rahimpour-Bonab, H., Enayati-Bidgoli, A. H., Navidtalab, A., & Mehrabi, H. (2014). Appraisal of intra-reservoir barriers in the Permo-Triassic successions of the Central Persian Gulf, Offshore Iran. *Geologica acta: an international earth science journal*, *12*(1), 87-107.

Scholle, P. A., & Ulmer-Scholle, D. S. (2003). *A Color Guide to the Petrography of Carbonate Rocks: Grains, Textures, Porosity, Diagenesis, AAPG Memoir 77* (Vol. 77). AAPG.

Senalp, M. and Al-Duaiji, A. (1995). Stratigraphy and Sedimentation of the Unayzah Reservoir, central Saudi Arabia. In, M. A. Al-Husseini (Ed.), *Middle East Petroleum Geosciences Conference, Geo'94, Gulf PetroLink, Bahrain*, *2*, 837- 847.

Sharief, F. A. (1983). Permian and Triassic geological history and tectonics of the Middle East. *Journal of Petroleum Geology*, *6*(1), 95.

Stampfli, G., Marcoux, J., & Baud, A. (1991). Tethyan margins in space and time. *Palaeogeography, Palaeoclimatology, Palaeoecology*, *87*(1), 373-409.

Steineke, M., Bramkamp, R.A., and Sander, N.J. (1958). Stratigraphic relations of Arabian Jurassic Oil, habitat of oil. *AAPG Bulletin*, 1294-1329.

Steineke, M., & Bramkamp, R. A. (1952, January). Mesozoic Rocks of Eastern Saudi-Arabia. In *AAPG Bulletin-American Association of Petroleum Geologists* , Vol. 36, No. 5, pp. 909-909.

Tavakoli, V., Rahimpour-Bonab, H., & Esrafili-Dizaji, B. (2011). Diagenetic controlled reservoir quality of South Pars gas field, an integrated approach. *Comptes Rendus Geoscience*, *343*(1), 55-71.

Vaslet, D., Le Nindre, Y., Vachard, D., Broutin, J., Crasquin-Soleau, S., Berthelin, M., & Al-Husseini, M. (2005). The Permian-Triassic Khuff Formation of central Saudi Arabia. *GeoArabia*, *10*(4), 77.

Weidlich, O. and Bernecker, M. (2010). The Permian-Triassic transition at Wadi Aday, Saih Hatat, Capital area. In A. Baud and M. Bernecker (Eds.), IGCP 572 Field Guide Book: The Permian-Triassic transition in the Oman Mountains. GUtech, Muscat, 17-33.

Weidlich, O. and Bernecker, M. (2011). Biotic carbonate precipitation inhibited during the Early Triassic at the rim of the Arabian Platform (Oman). *Palaeogeography, Palaeoclimatology, Palaeoecology*, (308), 129-150.

Wender, L. E., Bryant, J. W., Dickens, M. F., Neville, A. S., and Al-Moqbel, A. M. (1998). Paleozoic (Pre-Khuff) hydrocarbon geology of the Ghawar area, eastern Saudi Arabia. *GeoArabia*, *3*(2), 273-302.

Wignall, P.B., and Twitchett, R.J. (1999). Unusual intraclastic limestones in Lower Triassic carbonates and their bearing on the aftermath of the end-Permian mass extinction. *Sedimentology*, (46), 303-316.

Ziegler, M. A. (2001). Late Permian to Holocene paleofacies evolution of the Arabian Plate and its hydrocarbon occurrences. *GeoArabia,* 6, 445-504.

Ziegler, M. A., Hulver, M. L., and Rowley, D. B. (1997). Permian world topography and climate. In: I.P. Martini (ed.), *Late Glacial and Postglacial Environment Changes-Quaternary, Carboniferous-Permian, and Proterozoic*, Oxford University Press, Oxford 111-146.

APPINDIX

Sample Name	Porosity (Fraction)	Permeability (md)	RQI (µm)
KS1- 1V	0.01	7.57	0.864
KS1- 2V	0.03	12.71	0.669
KS1- 3V	0.05	5.09	0.317
KS1- 4V	0.07	21.63	0.544
KS1- 5	0.09	5.44	0.244
KS1- 6V	0.10	6.08	0.245
KS1-7	0.11	16.77	0.381
KS1-8V	0.13	6.03	0.211
KS1-9	0.14	14.11	0.311
KS1-10AV	0.15	6.03	0.199
KS1- 10BV	0.15	12.68	0.285
KS1- 10CV	0.16	6.03	0.193
KS1- 11	0.17	11.25	0.258
KS1- 12AV	0.17	6.03	0.185
KS1- 13V	0.18	29.54	0.399
KS1- 14V	0.19	7.23	0.194
KS1- 15V	0.20	5.51	0.166
KS1- 16V	0.21	8.31	0.198
KS1- 17V	0.22	3.5	0.127
KS1- 18V	0.22	14.48	0.254
KS1- 19V	0.24	27.2	0.338
KS1- 20V	0.25	5.33	0.144
KS1- 21V	0.27	10.81	0.199
KS1- 22V	0.28	5.12	0.135

Figure A.1: Porosity, permeability and calculated reservoir quality index (RQI) data for section #1. See Figure 6.1c for the location map.

Sample Name	Porosity (Fraction)	Permeability (md)	RQI (µm)
KS2 - 1H	0.02	0.12	0.076
KS2 - 2V	0.09	0.82	0.096
KS2 - 3V	0.03	0.115	0.061
KS2 - 4V	0.05	0.52	0.104
KS2 - 5V	0.04	0.117	0.057
KS2 - 6V	0.34	4.31	0.112
KS2 - 7	0.10	0.81	0.089
KS2 - 8V	0.28	23.64	0.290
KS2 - 9V	0.02	0.09	0.064
KS2 - 10V	0.19	54.23	0.533
KS2 - 11V	0.03	0.22	0.084
KS2 - 12V	0.08	2.1	0.158
KS2 - 14V	0.05	0.23	0.070
KS2 - 15V	0.03	0.19	0.079

Figure A.2: Porosity, permeability and calculated reservoir quality index (RQI) data for section #2. See Figure 6.1c for the location map.

Sample Name	**Porosity (Fraction)**	**Permeability (md)**	**RQI (µm)**
KS3 - 1V	0.01	2.14	0.419
KS3 - 2A V	0.04	10.1	0.499
KS3 - 2BV	0.06	8.12	0.382
KS3 - 3V	0.07	9.95	0.369
SK3 - 4V	0.09	2.01	0.152
SK3 - 5V	0.11	3.5	0.181
KS3 - 6V	0.15	27.6	0.433
KS3 - 7V	0.18	26.3	0.380
SK3 - 8V	0.19	2.5	0.114
KS3 - 9V	0.21	25.26	0.348
KS3 - 10 V	0.23	25.26	0.333
KS3 - 11V	0.29	22.1	0.274
KS3 - 11 H	0.34	24.1	0.264
KS3 - 12 V	0.38	5.1	0.116
KS3 - 13V	0.40	14.5	0.189
KS3 - 14 V	0.43	2.9	0.082
KS3 - 15V	0.46	19.8	0.206
KS3 - 16 V	0.49	2.5	0.071
KS3 - 17V	0.57	30	0.227
KS3 - 18 V	0.61	6.6	0.104
KS3 - 19V	0.63	14.7	0.152
KS3 - 20V	0.65	5.01	0.087

Figure A.3: Porosity, permeability and calculated reservoir quality index (RQI) data for section #3. See Figure 6.1c for the location map.

Sample Name	Porosity (Fraction)	Permeability (md)	RQI (µm)
KS4 - 1	0.15	1.04	0.082
KS4 - 2	0.06	0.26	0.068
KS4 - 3	0.04	0.21	0.071
KS4 - 4	0.07	0.36	0.069
KS4 - 5	0.15	1.14	0.086
KS4 - 6	0.08	0.52	0.078
KS4 - 7	0.02	0.10	0.079
KS4 - 8	0.17	2.09	0.111
KS4 - 9	0.03	0.11	0.060
KS4 - 10	0.09	0.41	0.066
KS4 - 11	0.04	0.72	0.133
KS4 - 12	0.03	0.14	0.069
KS4 - 13	0.07	0.31	0.066
KS4 - 14	0.09	0.41	0.066
KS4 - 15	0.06	0.23	0.062
KS4 - 16	0.04	0.21	0.071
KS4 - 17	0.14	0.93	0.082

Figure A.4: Porosity, permeability and calculated reservoir quality index (RQI) data for section #4. See Figure 6.1c for the location map.

Sample Name	Porosity (Fraction)	Permeability (md)	RQI (µm)
KS5 - 1	0.07	0.15	0.047
KS5 - 2	0.06	0.10	0.042
KS5 - 3	0.09	0.25	0.053
KS5 - 4	0.08	0.15	0.044
KS5 - 5	0.33	1.27	0.061
KS5 - 6	0.12	1.00	0.091
KS5 - 7	0.08	0.30	0.062
KS5 - 8	0.10	0.40	0.062
KS5 - 9	0.07	0.15	0.047
KS5 - 10	0.08	0.30	0.061
KS5 - 11	0.06	0.55	0.096
KS5 - 12	0.08	0.30	0.061
KS5 - 13	0.11	0.38	0.059
KS5 - 14	0.14	1.00	0.085
KS5 - 15A	0.05	0.30	0.078
KS5 - 15B	0.08	0.50	0.080
KS5 - 16	0.38	5.04	0.115
KS5 - 17	0.05	0.22	0.063
KS5 - 18 A	0.03	0.30	0.095
KS5 - 18B	0.08	0.22	0.052
KS5 - 19	0.05	0.15	0.054
KS5 - 20	0.04	0.15	0.058
KS5 - 21	0.06	0.23	0.061
KS5 - 22	0.05	0.37	0.085389

Figure A.5: Porosity, permeability and calculated reservoir quality index (RQI) data for section #5. See Figure 6.1c for the location map.

Sample Name	**Porosity (Fraction)**	**Permeability (md)**	**RQI (µm)**
KS6 - 1	0.08	0.10	0.035
KS6 - 2	0.07	0.08	0.034
KS6 - 3	0.05	0.35	0.086
KS6 - 4	0.09	0.20	0.046
KS6 - 5	0.09	0.30	0.058
KS6 - 6	0.05	0.35	0.082
KS6 - 7	0.05	0.40	0.086
KS6 - 8	0.12	0.12	0.031
KS6 - 9	0.04	0.04	0.032
KS6 - 10	0.04	0.15	0.061
KS6 - 11	0.08	0.09	0.034
KS6 - 12	0.04	0.09	0.045
KS6 - 13	0.26	0.10	0.020
KS6 - 14	0.03	0.02	0.027
KS6 - 15	0.23	3.08	0.114
KS6 - 16	0.31	2.08	0.082
KS6 - 17	0.17	1.69	0.098
KS6 - 18	0.21	2.00	0.096
KS6 - 19	0.02	0.03	0.045
KS6 - 20	0.20	1.13	0.075
KS6 - 21	0.21	1.51	0.085
KS6 - 22	0.12	0.12	0.031
KS6 - 23	0.03	0.03	0.031

Figure A.6: Porosity, permeability and calculated reservoir quality index (RQI) data for section #6. See Figure 6.1c for the location map.

Sample Name	Porosity (Fraction)	Permeability (md)	RQI (μm)
KS7- 1V	0.05	0.33	0.081
KS7- 2V	0.08	0.83	0.099
KS7- 3V	0.08	0.77	0.098
KS7- 4V	0.05	0.70	0.114
KS7- 5V	0.25	1.36	0.074
KS7- 6V	0.27	1.42	0.072
KS7- 7V	0.28	1.45	0.072
KS7- 8V	0.08	0.98	0.111
KS7- 9V	0.18	1.09	0.078
KS7- 10V	0.16	1.00	0.079
KS7- 11AV	0.08	0.46	0.075
KS7- 11 BV	0.04	0.26	0.085
KS7- 12V	0.13	1.21	0.097
KS7- 13H	0.05	0.23	0.066
KS7- 14V	0.08	0.88	0.104
KS7- 15V	0.20	1.61	0.090
KS7- 16V	0.11	0.92	0.093
KS7- 17V	0.02	0.10	0.072
KS7- 18V	0.10	0.83	0.090
KS7- 19V	0.03	0.26	0.096
KS7- 20V	0.23	1.01	0.066

Figure A.7: Porosity, permeability and calculated reservoir quality index (RQI) data for section #7. See Figure 6.1c for the location map.

Sample Name	Porosity (Fraction)	Permeability (md)	RQI (µm)
KS8 - 1	0.02	0.13	0.087
KS8 - 2	0.03	0.15	0.073
KS8 - 3	0.04	0.17	0.068
KS8 - 4	0.20	2.59	0.114
KS8 - 5	0.07	0.30	0.064
KS8 - 6	0.04	0.86	0.139
KS8 - 7	0.02	0.14	0.084
KS8 - 8	0.04	0.18	0.067
KS8 - 9	0.14	1.05	0.088
KS8 - 10	0.12	0.93	0.088
KS8 - 11	0.12	1.04	0.092
KS8 - 12	0.02	0.15	0.083
KS8 - 13	0.20	1.34	0.082
KS8 - 14	0.10	0.62	0.078
KS8 - 15	0.23	2.84	0.110

Figure A.8: Porosity, permeability and calculated reservoir quality index (RQI) data for section #8. See Figure 6.1c for the location map.

Sample Name	Porosity (Fraction)	Permeability (md)	RQI (µm)
KS9 - 1	0.23	1.14	0.069
KS9 - 2	0.27	1.10	0.063
KS9 - 3	0.14	2.11	0.124
KS9 - 4	0.05	0.09	0.045
KS9 - 7 A	0.06	0.12	0.043
KS9 - 7 B	0.06	0.11	0.042
KS9 - 7 C	0.03	0.09	0.051
KS9 - 7 D	0.05	0.08	0.038
KS9 - 8	0.15	0.68	0.068
KS9 - 9	0.18	0.70	0.063
KS9 - 10	0.06	0.80	0.117
KS9 - 12	0.19	0.80	0.065
KS9- 13	0.04	0.07	0.040
KS9 - 14	0.05	0.70	0.122
KS9- 15	0.05	0.80	0.121
KS9 - 16	0.04	0.08	0.046
KS9- 18	0.08	0.13	0.039
KS9 - 19	0.09	0.18	0.045
KS9 - 20	0.05	0.74	0.122

Figure A.9: Porosity, permeability and calculated reservoir quality index (RQI) data for section #9. See Figure 6.1c for the location map.

Sample Name	**Porosity (Fraction)**	**Permeability (md)**	**RQI (µm)**
KS10 - 1	0.22	0.56	0.050
KS10 - 2	0.33	1.37	0.064
KS10 - 3	0.13	0.88	0.082
KS11 - 4	0.26	3.93	0.123
KS11 - 5	0.19	0.83	0.065
KS10 - 6	0.04	0.17	0.062
KS10 - 7 A	0.11	2.21	0.143
KS10 - 7 B	0.04	0.58	0.114
KS10 - 7 C	0.04	0.14	0.062
KS10 - 7 D	0.06	0.37	0.077
KS10 - 8	0.06	0.27	0.066
KS10 - 9	0.03	0.16	0.074
KS10 - 10	0.05	0.17	0.060
KS11 - 11	0.10	1.39	0.117
KS10 - 12	0.03	0.32	0.104
KS10- 13	0.05	1.63	0.175
KS10 - 14	0.09	3.72	0.204
KS10- 15	0.25	13.17	0.229
KS10 - 16	0.12	9.58	0.275
KS11 - 17	0.13	10.17	0.279
KS10- 18	0.11	6.65	0.242
KS10 - 19	0.07	1.90	0.160
KS10 - 20	0.08	1.65	0.143
KS11 - 21	0.07	0.96	0.116
KS11 - 22	0.06	0.46	0.089

Figure A.10: Porosity, permeability and calculated reservoir quality index (RQI) data for section #10. See Figure 6.1c for the location map.

Vitae

Name : Asaad Mohammed Mohammed Ahmed Abdulraziq

Nationality : Sudanese

Date of Birth : 8/30/1988

Email : asaadmoha01@hotmail.com

Address : KFUPM, Dhahran, Saudi Arabia

Academic Background: B.Sc. (Honor) in Geology from University of Khartoum (Sudan).

Journal Papers:

Eltom, H., Abdullatif, O., Makkawi, M., & **Abdulraziq, A.** (2013). Microporosity in the upper jurassic arab-d carbonate reservoir, central saudi arabia: An outcrop analogue study. *Journal of Petroleum Geology*, *36*(3), 281-297.

Eltom, H., Abdullatif, O., Makkawi, M., & **Abdulraziq, A.** (2014). Characterizing and modeling the Upper Jurassic Arab-D reservoir using outcrop data from Central Saudi Arabia. *GeoArabia*, *19*(2), 53-84.

Eltom, H., Abdullatif, O., Makkawi, M., Al- Ramadan, K., & **Abdulraziq, A.** (2014). Porosity Evolution within High Resolution sequence stratigraphy and Diagenesis Framework: Outcrop Analog of the Upper Jurassic Arab-D Reservoir, Central Saudi Arabia. *Arabian Journal of Geosciences*.

Conference Papers:

Abdulraziq, A., Abdullatif, O., & Eltom, H. (2013, April). In W. Abdulghani and A. Bakhiet (Chair). *Porosity-permeability distributions in the Khartam Member of the permo-triassic Khuff Formation: Outcrop approach, central saudi arabia*. 10th saudi society for geosciences conference, KFUPM, Dhahran, Saudi Arabia.

Osman, M., Bashir, M., Eltom, H., **Abdulraziq, A.**, Aqil, M., & Abdullatif, O. (2013, April). In M. Al-Dabbagh and K. Al-Ramadan (Chair). *Sedimentology and Stratigraphy of the Late Triassic Minjur and Early Jurassic Marrat Formations: Implication to Sequence Development and Reservoir Architecture, Central Saudi Arabia.* 10th saudi society for geosciences conference, KFUPM, Dhahran, Saudi Arabia.

Abdullatif, O., Yassin, M., Al-Mubarak, A., & **Abdulraziq, A.** (2013, April). In E. Setoyama & M. Benaafi (Chair). *Geological Model of Dam and Hofuf Formations (Miocene-Pliocene): An integrated Approach Utilizing Sequential and Chemostratigraphy, Lidar and Gamma Ray, Eastern Saudi Arabia.* 10th saudi society for geosciences conference, KFUPM, Dhahran, Saudi Arabia.